Chapter 3
Multifunctional Properties of Bulk Nanostructured Metallic Materials

This chapter focuses on multifunctional properties of bulk nanostructured metallic materials and structure–properties relationship therein. The most important structural factors affecting mechanical, physical, and chemical properties of the nanomaterials are discussed, and the strategies to their further improvement are outlined. Special attention is paid to nanostructural design for simultaneous improvement of mutually exclusive properties.

3.1 Superstrength and Enhanced Mechanical Properties

Although the mechanical and functional properties of all polycrystalline metallic materials are determined by several factors, the grain size of the material generally plays the most significant and often a dominant role. Thus, the strength of different polycrystalline materials is related to the grain size, d, through the Hall–Petch equation which states that the yield stress, σ_y, is given by

$$\sigma_y = \sigma_o + k_y d^{-1/2}, \tag{3.1}$$

where σ_o is termed the friction stress and k_y the Hall–Petch constant [1, 2]. It follows from Eq. 3.1 that the strength increases with a reduction in the grain size and this has led to an ever-increasing interest in fabricating materials with extremely small grain sizes.

The fabrication of bulk samples and billets using equal channel angular pressing (ECAP), high pressure torsion (HPT), and other severe plastic deformation (SPD) techniques was a crucial first step in initiating investigations into the properties of bulk nanomaterials because the use of SPD processing permitted, and subsequently fully supported, a series of systematic studies using various nanostructured metallic materials including commercial alloys [3–8]. The research

© I. Sabirov, N.A. Enikeev, M.Yu. Murashkin, and R.Z. Valiev 2015

I. Sabirov et al., *Bulk Nanostructured Materials with Multifunctional Properties*, SpringerBriefs in Materials, DOI 10.1007/978-3-319-19599-5_3

works include strength and strengthening mechanisms, ductility, and ways to its enhancement, fatigue, and wear resistance. The main achievements of these studies are discussed in the section below.

3.1.1 Superstrength and Ductility

During the last two decades, the influence of grain size reduction to nanometer range on the materials strength has been explored in multiple works (see, e.g., [5, 9–11]. The enhancement of strength with grain size reduction in compliance with Eq. 3.1 was observed in many studies (Fig. 3.1), but for nanosized grains (20–50 nm), this relations reported to be typically violated so that the Hall–Petch plot deviates from linear dependence at lower stress values and its slope k_y often becomes negative (the curve 1 in Fig. 3.1). In recent years, this problem has been widely analyzed in both experimental and theoretical studies [5, 10]. At the same time, Hall–Petch relationship breakdown is not observed in ultrafine-grained materials with a mean grain size of 100–1000 nm produced by SPD processing. Moreover, recently it was shown that UFG alloys can exhibit a considerably higher strength than the Hall–Petch relationship predicts for the range of ultrafine grains [12–15]. The nature of such superstrength may be associated with another nanostructural features (dislocation substructures, nanophase particles and segregations, nanotwins, etc.) which could be observed in the SPD-processed metals and alloys (see Chap. 2).

For example, this was shown in studies of the mechanical behavior of Ni subjected to ECAP and subsequent rolling [16]. Figure 3.2 shows the difference in strength between the states of Ni where the grains contain dislocation substructures within the grains and where the grains contain no substructure [17–19]. An attempt was made to describe quantitatively the deviation from the Hall–Petch rule by taking into account the influence of two types of boundaries, high-angle boundaries between grains and low-angle cell boundaries, on the yield stress of the material. Following an earlier analysis [20], it was assumed that each of these types of

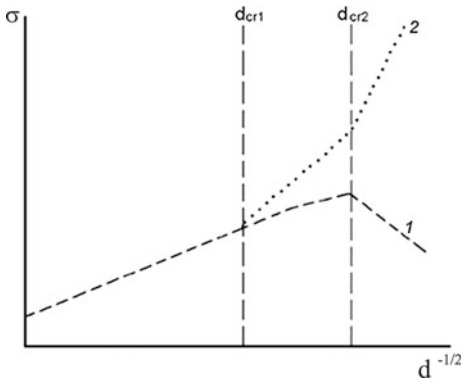

Fig. 3.1 The two types of the Hall–Petch slopes within different characteristic length scales

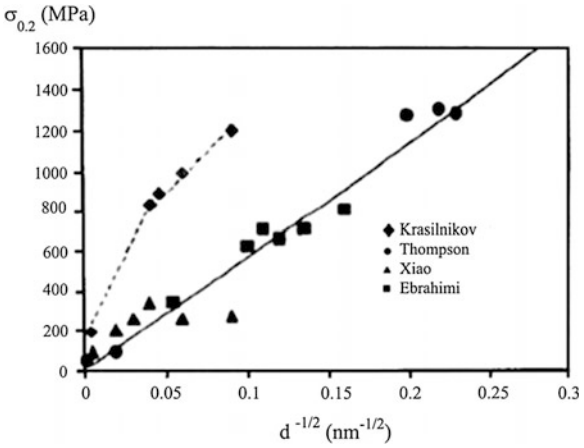

Fig. 3.2 Yield stress as a function of $d^{-1/2}$ for Ni: the continuous line is for material states with grains without substructure, and the dashed line is for nanostructured Ni containing a dislocation substructure [16–19]

boundaries, and also the non-equilibrium state of grain boundaries, contributes in an independent way to the yield stress:

$$\sigma_y = \sigma_o + \sigma_{LAB} + \sigma_{HAB} + \sigma_{NGBs} \tag{3.2}$$

and

$$\sigma_y = \sigma_o + M\alpha Gb\left((1.5S_v\theta/b)_{LAB}\right) + k_y d^{-1/2} + M\alpha Gb(\rho_{GBDs})^{1/2} \tag{3.3}$$

where σ_o is the threshold stress, M the Taylor factor, α a constant ($\alpha = 0.24$), G the shear modulus, b the Burgers vector, θ the misorientation angle of the low-angle grain boundaries, d the average grain size, ρ_{GBDs} the density of extrinsic grain boundary dislocations, k_y the Hall–Petch constant and the term S_v associated with the cell size. The numerical values for the constants were taken from the earlier report [20].

The contributions of these different components for SPD-processed Ni correspond well to the experimentally obtained data as shown in Table 3.1. After HPT, a homogeneous UFG structure was formed with mainly high-angle misorientations. Therefore, for the HPT sample, it is reasonable to neglect the contribution of low-angle grain boundaries. The analysis of mechanical test data shows that the presence of substructure and the non-equilibrium state of grain boundaries contributes more strongly to the yield stress of SPD-processed Ni than the strength calculated according to the Hall–Petch rule for a material with the given grain size.

In addition to the dislocation substructure and non-equilibrium grain boundaries, other nanostructured elements formed in the UFG materials processed by SPD may contribute to the change of yield stress and flow stress. This issue was recently studied in detail for the case of superstrong UFG Al alloys, namely AA1570 and AA7475 [12, 13].

Table 3.1 Contribution to flow stress for SPD-processed pure Ni

Processing of Ni	YS_{exp} (MPa)	YS_{calc} (MPa)	σ_{LAB} (MPa)	σ_{HAB} (MPa)	σ_{GBDs} (MPa)
ECAP + rolling	990	980	510	280	170
HPT	1200	1190	–	460	710

YS_{exp}—experimental data, YS_{calc}—calculated by means of Eq. 3.3

The transmission electron microscopy (TEM) analysis demonstrated that HPT leads to a complete transformation of the initial coarse-grained structure of the alloys into the UFG structure. In the alloys 1570 and 7475, homogeneous UFG structures with a grain size of about 100 nm were formed after HPT as shown in Fig. 3.3. It was also determined that HPT processing has a visible effect on the value of the crystal lattice parameter α of Al alloys. For example, in the AA1570, its value after straining was reduced considerably in comparison with the initial state, from 4.0765 ± 0.0001 Å to 4.0692 ± 0.0003 Å, which results from the formation of Mg segregations at grain boundaries [12, 13].

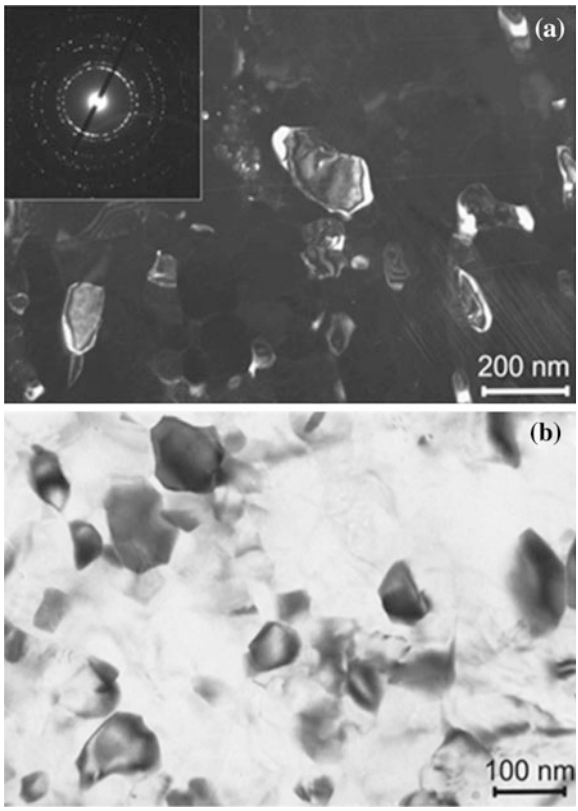

Fig. 3.3 A typical TEM dark-field image of the UFG 1570 alloy with a corresponding SAED (**a**), a bright-field image (**b**). The images are reproduced from [12] with the permission from the publisher

Figure 3.4 shows the results of mechanical testing of the 1570 and 7475 alloys. It can be seen that the UFG alloys processed by HPT at room temperature demonstrate record strength that more than twice exceeds the level of strength of the material subjected to standard hardening.

Figure 3.5 illustrates the data for a number of Al alloys presented in the form of the Hall–Petch relation in which the yield stress ($\sigma_{0.2}$) is plotted against the inverse square root of the grain size ($d^{-1/2}$) for a UFG AA1100 produced by accumulative roll bonding (ARB)-rolling and consequent heat treatment [21] as well as for an ECAP-processed Al–3 % Mg alloy [22]. For the Hall–Petch relation in the AA1100 [21], the following parameters were set: σ_o = 6.0 MPa and k_y = 105 (for the grain sizes in μm); for the ECAP-processed Al–3 % Mg alloy [22], σ_o = 62 MPa and k_y = 149. Figure 3.5 also shows the data obtained for the coarse-grained and UFG AA1570 and AA7475.

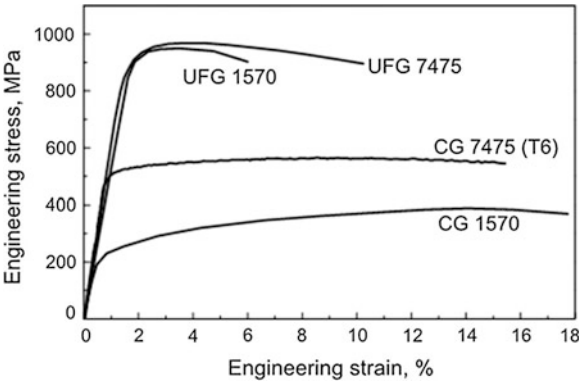

Fig. 3.4 Engineering stress–strain curves for AA1570 and AA7475 in UFG and coarse-grained states. The curves are reproduced from [12] with the permission from the publisher

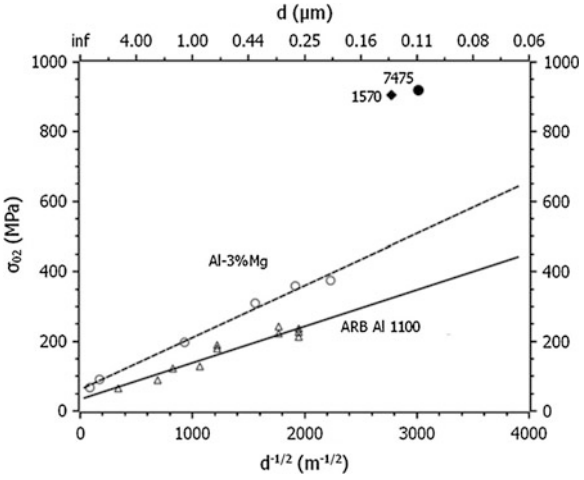

Fig. 3.5 The Hall–Petch relation for the Al alloys 1100 [21] and Al–3 % Mg [22] and data on the yield stresses of the UFG alloys 1570 and 7475

From the available data, it is seen that the σ_y values for the coarse-grained solution-treated alloys are close to the results for the Al–3 % Mg alloy. However, for the UFG states in the 1570 and 7475 alloys with a grain size of 100–130 nm, the value σ_y is considerably higher than that calculated from the Hall–Petch relation.

The Hall–Petch plot for commercially pure (CP) Ti (A-70, similar to Grade 4) and Armco-Fe is given in Figs. 3.6 and 3.7, respectively [23–26]. Here, one can also see experimental data for several UFG materials produced by SPD. In the case of CP Ti, the data are presented for HPT-processed UFG Ti–6 % Al–4 % V [27] and also for UFG Ti (Grade 4) processed by ECAP and further thermo-mechanical treatment (TMT) [28]. For the UFG CP Ti, the σ_y values are higher than those could be predicted by the Hall–Petch relation for the given grain sizes. For UFG Fe, the data on tensile mechanical tests are presented only in [29], but there is evidence on microhardness H_v that is demonstrated in Fig. 3.7 using the ratio $\sigma_y = H_v/3$. The data for HPT-processed UFG steel 20 with 0.2 % C content are also presented here [30]. Similar to CP Ti, there is a considerable excess of experimental σ_y values (for steel 20) over the values predicted from the Hall–Petch relation.

Thus, the new phenomena of 'superstrength' of nanostructured metals and alloys produced by SPD can be observed for various materials reflecting the 'positive' slope of the Hall–Petch relation as demonstrated in Fig. 3.1 (curve 2). 'Superstrength' in bulk nanostructured materials can be of different origin. First, it can result from additional—already known—strengthening mechanisms, i.e., solid solution strengthening, precipitation strengthening, and dislocation strengthening [5, 31]. However, the influence of new strengthening mechanisms is also possible—these arise from the change in grain boundary structure and lead to further strength enhancement [15, 32].

Recently, based on experimental studies of materials obtained by vacuum deposition [33], Firstov et al. [34] reported a 'positive' slope of the Hall–Petch relation, where for the grain size range $d_{cr2} < d < d_{cr1}$, the exponent of d in Eq. 3.1

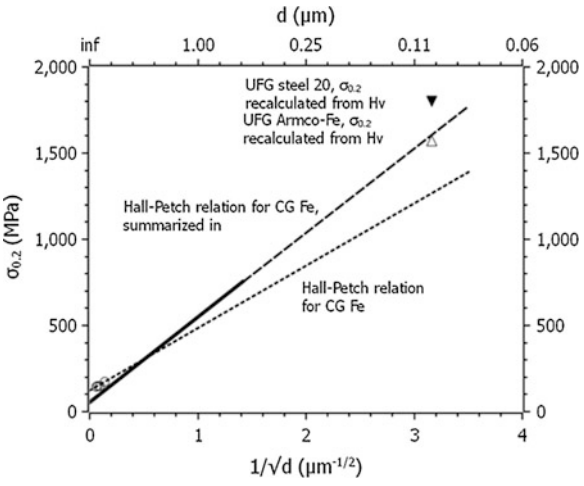

Fig. 3.6 The Hall-Petch relation for Armco-Fe [25] and iron [26] and data on the yield stresses of UFG Fe [23, 29] and steel 20 [30]

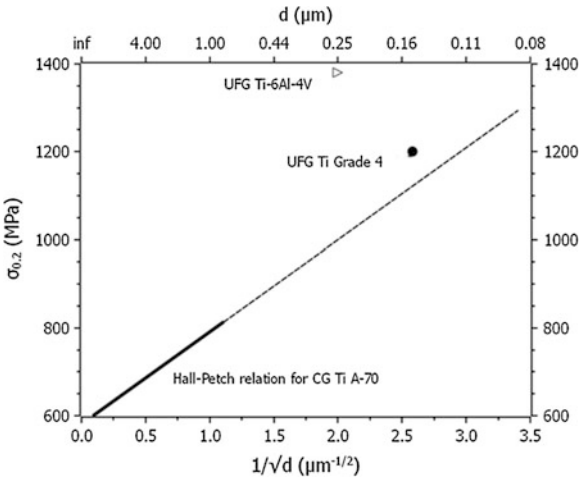

Fig. 3.7 The Hall–Petch relation for Ti and A-70 [24] and data on the yield stresses of UFG Ti [28] and T–6 % Al–4 % V alloy [27]

varied from −1/2 to −1, and for $d < d_{cr1}$, the exponent of d was equal to −3 with the presence of grain boundary segregations.

For SPD-processed metals, it is difficult yet to speak in terms of definite values for the exponent of d in Eq. 3.1 due to low statistics of experimental data presently available. However, it is possible that the presence of two characteristic grain size values is also valid for nanostructured SPD materials. Indeed, as it has been already pointed out, the presence of non-equilibrium grain boundaries is typical for the majority of SPD-processed materials, but their influence on mechanical properties becomes considerable when the grain size is below 500–1000 nm [35]. When the grain size decreases down to 100 nm and less, grain boundary segregations provide a significant contribution to the overall strength. Recently, this topic was addressed in [12], where it was shown that high strength of the UFG Al alloys was directly related to the formation of Mg segregations at grain boundaries revealed in the alloys by 3D APT technique [12, 36, 37]. Because in UFG materials deformation takes place by dislocations generated at grain boundaries and moving through a grain to be captured by an opposite grain boundary, the rate-controlling mechanism is the 'dislocation–grain boundary' interaction. In this case, the elevated concentration of solutes in grain boundaries can suppress emission of dislocations from such boundaries due to solute drag, and as a result, the stress needed to emit a dislocation increases.

Recently, this finding was confirmed for the case of UFG stainless steel 316 produced by HPT at different temperatures [38]. Earlier, it was found that the HPT 316 steel processed at room and elevated temperatures demonstrates similar strength despite the difference in grain size and dislocation density [39, 40]. In [38], it was shown that the steel, SPD processed at room temperature, exhibits no pronounced grain boundary segregations and fits well the Hall–Petch relation extrapolated to the corresponding grain size. However, the steel processed at 400 °C was found to contain complex Si–Cr–Mo grain boundary segregations, and its strength

considerably exceeded the value predicted by the Hall–Petch law. Similar idea was used to explain enormous increase (from 1360 MPa to 2230 MPa) in yield stress of a 316 steel subjected to HPT at room temperature followed by subsequent annealing at 500 °C for 1 h [41]. The authors suggested that it can be explained by the fact that thermal treatment leaded to formation of grain boundary segregations which became precursors for G-phase observed in grain boundaries after further long-term annealing.

These findings on the role of SPD-induced GB segregations open a way for a new direction in nanostructural design of SPD-processed materials and also may be used in grain boundary segregation engineering of the other types of nanomaterials [42, 43].

This point is in good agreement with the experimental data and also makes it possible to explain considerably higher strength values observed in the UFG alloys in comparison with pure metals. At the same time, the task of oncoming research is to explore the segregations and determine which elements, and the level of their concentrations, produce the most influence on strength enhancement in bulk nanostructured materials. This point is also important in answering the question of the precise origin of very high strength in nanostructured multiphase alloys that possess the most strength among metallic nanomaterials, which was recently discussed in [44].

High ductility in metallic materials is another very important property for their structural use. It is essential for metal-forming operations as well as to avoid catastrophic failure in load-bearing applications during their service life. The ductility of materials is defined as the extent to which a material can be plastically deformed. Two measures of ductility will be considered below. First, uniform elongation is the maximum strain where homogeneous plastic flow (uniform reduction of cross-sectional area) is still observed and beyond which a diffuse necking begins. The uniform elongation is determined by competition between plastic flow and materials resistivity to macro-localization of plastic flow. It can be important in stretch-metal-forming operations. The second measure, elongation to failure (often referred to as total elongation to fracture or engineering strain at fracture), is a sum of uniform elongation and necking elongation. The latter is controlled by competition between localized plastic flow and fracture processes.

It has been a long-standing goal for materials scientists to synthesize structural materials with balanced combinations of high strength and high ductility. However, during the last decade, it has been widely demonstrated that a major grain refinement, down to the nanometer range, may lead to a very high hardness and strength in various metals and alloys, but nevertheless, these materials invariably exhibit low ductility under tensile testing [6, 45, 46]. A similar tendency is well known for metals subjected to heavy straining by other processes such as rolling, extrusion, or drawing. Strength and ductility are the key mechanical properties of any material, but these properties typically have opposing characteristics. Thus, materials may be strong or ductile, but they are rarely both. The reason for this dichotomy is of a fundamental nature. Indeed, the plastic deformation mechanisms associated with the generation and movement of dislocations may not be effective in ultrafine

grains. This is generally equally true for SPD-processed materials. Thus, most of these materials have a relatively low ductility, but they usually demonstrate significantly higher strength than their coarse-grained counterparts. It is important to note that SPD processing leads to a reduction in the ductility which is generally less than in more conventional deformation processing techniques such as rolling, drawing and extrusion. For example, experiments were conducted to compare the strength and ductility of the AA3004 processed by ECAP and cold-rolling (CR) [47]. As illustrated by the data plotted in Fig. 3.8, the yield strength increased monotonically with the increasing equivalent strain imparted into the alloy by either CR or ECAP [48]. However, it is apparent also that the overall ductility exhibits different trends for these two processing methods. After one ECAP pass, equivalent to a strain of ~ 1, the elongation to failure decreases from ~ 32 to ~ 14 %. At the same time, there is no additional reduction in the ductility with additional ECAP passes. By contrast, CR decreases the ductility by a similar magnitude initially, but thereafter, the ductility continues to decrease with increasing rolling strain although at a slower rate. Consequently, ECAP processing of the alloy leads ultimately to a greater retention of ductility than conventional CR.

Typically, in the nanostructured metallic materials, plastic deformation localizes at the very early stage of plastic deformation (1–3 %) resulting in necking, followed by a specimen failure. Various strategies to improve low ductility of the nanostructured metals and alloys have been proposed [31, 49, 50]. These strategies could be divided into two groups which we would define as (1) 'mechanical' strategies and (2) 'microstructural' strategies. The 'mechanical' strategies employ the mechanical characteristics of the UFG materials such as their work hardening ability and/or strain rate sensitivity. These mechanical characteristics can be varied by changing the testing parameters such as temperature and/or strain rate. The 'microstructural' strategies are based on the idea of intelligent microstructural design.

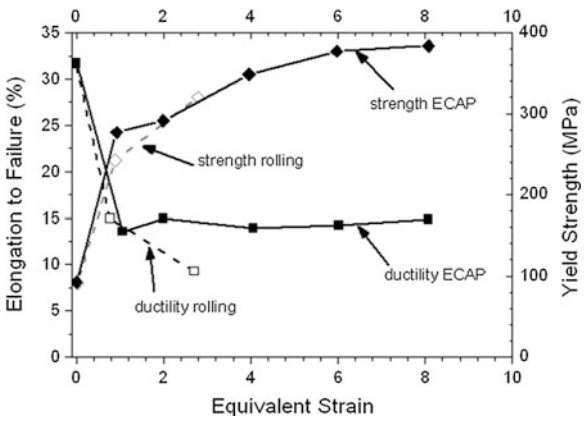

Fig. 3.8 A comparison of yield strength and ductility for an Al-3004 alloy processed by cold-rolling or ECAP. The figure is reproduced from [48] with the permission from the publisher

For tensile behavior, the uniform strain is usually in good agreement with the well-known Considère criterion [51],

$$(\mathrm{d}\sigma/\mathrm{d}\varepsilon) = \sigma \tag{3.4}$$

which is a geometric criterion stating that when the work hardening rate, ($\mathrm{d}\sigma/\mathrm{d}\varepsilon$), decrease to the level of the flow stress, σ, macro-localization of plastic deformation (necking) should occur resulting in a specimen failure. The nanostructured metallic materials are usually characterized by increased strain rate sensitivity even at low temperatures compared to their coarse-grained counterparts [49, 50]. Therefore, the Hart criterion [52] is more appropriate to predict the uniform elongation of the nanostructured metals and alloys:

$$(\mathrm{d}\sigma/\mathrm{d}\varepsilon) = (1 - m)\sigma \tag{3.5}$$

where m is the strain rate sensitivity index. It follows from Eq. 3.5 that the uniform elongation can be enhanced by (1) increasing the work hardening rate $\mathrm{d}\sigma/\mathrm{d}\varepsilon$ and/or (2) the strain rate sensitivity m.

Meanwhile, since the mechanical characteristics of the materials are also determined by their microstructure, it can be outlined that manipulation with the microstructure is the major tool to enhance the ductility of the nanostructured alloys.

In this connection, findings of extraordinarily high strength and good ductility in several bulk UFG metals produced by SPD are of special interest [53–57]. It is important to consider in detail the three different approaches that were used in the earlier investigations.

In the first study, high-purity (99.996 %) Cu was processed at room temperature using ECAP with a 90° clockwise rotation around the billet axis between consecutive passes in route B_C [54]. The strength and ductility were measured by uniaxial tensile tests, and the resulting engineering stress–strain curves are shown in Fig. 3.9 for the Cu samples tested at room temperature in the initial coarse-grained condition and in three processed states [54]. It is apparent that the initial coarse-grained Cu with a grain size of about 30 μm has a very low yield stress with significant strain hardening and a large elongation to failure. CR of the Cu with reduction ratio of 60 % significantly increases the strength (curve 2 in Fig. 3.9), but dramatically decreases the elongation to failure. This result is consistent with the classical mechanical behavior of metals that are plastically deformed. The same tendency is true also for Cu subjected to two passes of ECAP. However, further straining of Cu to 16 passes of ECAP (curve 4 in Fig. 3.9) simultaneously increases both the strength and ductility. Furthermore, the increase in ductility is much more significant than the relatively minor increase in strength. Thus, the data shown in Fig. 3.9 for ECAP-processed Cu clearly demonstrate an enhancement of strength as well as ductility with accumulated deformation due to an increase in the number of passes from 2 to 16 [54]. This is a very remarkable result that for the first time was observed in metals processed by plastic deformation. Accordingly, this effect was

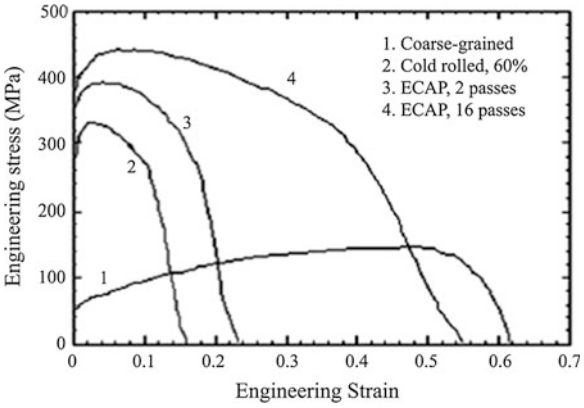

Fig. 3.9 Tensile engineering stress–strain curves for Cu tested at 22 °C with a strain rate of 10^{-3} s^{-1}: The processing conditions for each curve are indicated. The curves are reproduced from [54] with the permission from the publisher

termed the 'paradox of strength and ductility in SPD-processed metals,' and the principles of this paradox are illustrated in Fig. 3.10, where it is apparent that conventional metals lie within the lower shaded quadrant [54]. As shown in Fig. 3.10, for Cu and Al, CR (the reduction in thickness is marked by each datum point) increases the yield strength but decreases the elongation to failure [58, 59]. The extraordinary combination of high strength and high ductility shown in Fig. 3.10 for the nanostructured Cu and Ti after SPD processing clearly sets them apart from the other coarse-grained metals.

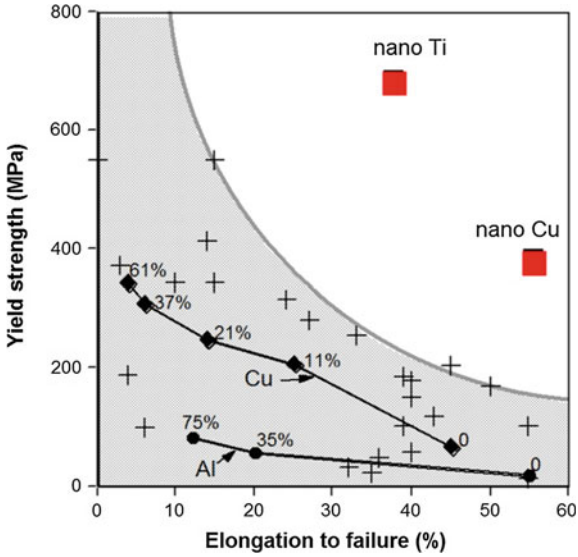

Fig. 3.10 The paradox of strength and ductility in metals subjected to SPD: the extraordinary combination of high strength and high ductility in nanostructured Cu and Ti processed by SPD (*two upper points*) clearly sets them apart from conventional coarse-grained metals (*lower points* relating to metals of 99.5–99.9 % purity) [54]

In recent years, similar tendencies have been reported in a number of metals, including Al [60, 61], Cu [62], Ni [16], and Ti [54, 57], after SPD processing via ECAP, HPT, and ARB. Concerning the origin of this phenomenon, it has been suggested that it is associated with an increase in the fraction of high-angle grain boundaries with increasing straining and with a consequent change in the dominant deformation mechanisms due to the increasing tendency for the occurrence of grain boundary sliding and grain rotation [53, 54].

Another approach to enhance ductility is based on introduction of a bimodal distribution of grain sizes [56, 64]. In [56], nanostructured Cu was produced through a combination of ECAP and subsequent rolling at the liquid nitrogen temperature prior to heating to a temperature of $\sim$450 K. This processing route resulted in the formation of a bimodal structure of micrometer-sized grains, with a volume fraction of around 25 %, embedded in a matrix of nanocrystalline grains. The material exhibited an extraordinarily high ductility but also retained a very high strength. The reason for this behavior is that while the nanocrystalline grains provide strength, the embedded larger grains stabilize the tensile deformation of the material. Other evidences for the importance of grain size distribution come from investigations on Zn [63], Cu [64], and Al alloys [65]. Furthermore, the investigation of Cu [64] showed that bimodal structures may increase the ductility not only during tensile testing but also during cyclic deformation. This observation is also important in improving the fatigue properties of materials, as discussed in Sect. 3.1.2.

Some microstructural modification may not only increase the strength at expense of ductility (or to increase ductility sacrificing strength), but also improve both ductility and strength [68]. Given that the low ability for strain hardening in nanostructured materials is caused by the limitations for accumulating dislocations and other defects in nanostructured materials, these strategies are based on modifying the nanostructural features to promote accumulation of dislocations [46]. This idea was successfully realized in a commercial Al–Zn–Mg–Cu–Zr alloy [66] and an Al–10.8 % Ag alloy [55] subjected to ECAP and subsequent artificial aging. The principle of this approach is illustrated in Fig. 3.11 for the Al–Ag alloy, where the Vickers microhardness is plotted against the aging time at 373 K for samples in a solution-treated (ST) condition and after CR and ECAP [55]. For the ST condition, the hardness is initially low but increases with aging time to a peak value after 100 h (3.6×10^5 s). For the CR condition, the hardness is higher, but there is only a minor increase with aging. The hardness is even higher after ECAP and further increases with aging to a peak value after 100 h. The relatively lower values of hardness recorded after CR in comparison with ECAP are due to the lowerequivalent strain imposed on the sample: These strains were $\sim$1.4 in CR and $\sim$8 in ECAP, so the microstructure after CR consisted of subgrains and cell boundaries having low misorientation angles. It was shown, using scanning TEM, that the peak hardness achieved after ECAP and aging for 100 h is due to precipitation within the grains of spherical particles with diameters of $\sim$10 nm and elongated precipitates with lengths of $\sim$20 nm. The spherical particles were identified as η-zones consisting of arrays of solute atoms lying parallel to the (001) planes, and the elongated precipitates were identified as the platelike γ' particles. It was shown also that additional

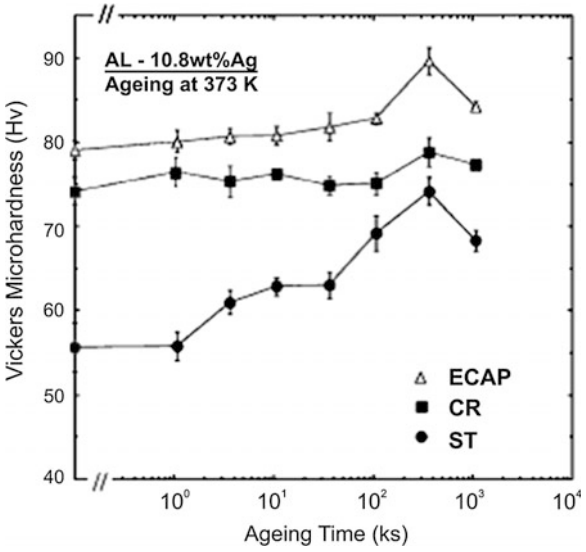

Fig. 3.11 Variation of the Vickers microhardness with aging time for the Al–10.8 % Ag alloy after solution treatment (ST), cold-rolling (CR), and ECAP [55]

aging up to 300 h led to a growth in the γ' particles and a very significant reduction in the density of the fine η-zones, thereby giving a consequent loss in hardening at the longest aging time recorded in Fig. 3.11. Introduction of artificial aging after ECAP has an important influence on the stress–strain behavior at room temperature, as demonstrated in Fig. 3.12, where the tensile stress–strain curves are shown after ECAP and after ST, CR, and ECAP with additional aging for 100 h at 373 K: Each sample in Fig. 3.12 was tested at room temperature at an initial strain rate of 10^{-3} s^{-1} [55]. Thus, ST and artificial aging give a reasonable tensile strength, an extensive region of uniform strain and good ductility, whereas CR and aging give an increased strength but very limited uniform strain and a marked reduction in the total ductility. For the ECAP condition, the strength is high in the absence of aging, but there is a negligible region of uniform strain and no significant strain hardening. By contrast, the sample processed by ECAP and aged for 100 h shows a similar high strength, a region of strain hardening and good ductility. In practice, the uniform strain of $\sim$0.14 achieved in this specimen is similar to the uniform strain of $\sim$0.17 in the sample after ST and aging, and the elongation to failure of $\sim$0.40 is comparable to, and even slightly exceeds, the elongation of $\sim$0.37 recorded in the ST and aged condition. These results demonstrate, therefore, the potential for producing high strength and good ductility in precipitation-hardened alloys. Furthermore, although the results documented in Figs. 3.11 and 3.12 relate to a model Al–Ag alloy, it is reasonable to anticipate that it should be possible to achieve similar results in commercial engineering alloys where the aging treatments are generally well documented. Indeed, this approach was successfully realized also on AA7075 [68] and AA2024 [69].

The next strategy in nanostructural design to improve strength and ductility relies on introduction of high density of twins, which could also assist effective

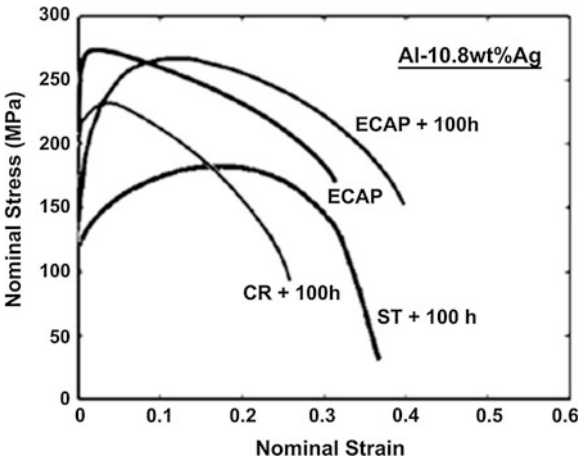

Fig. 3.12 Tensile plots of stress versus strain at room temperature for the Al–10.8 % Ag alloy after solution treatment (ST) or cold-rolling (CR) with aging at 373 K for 100 h or ECAP without subsequent aging and ECAP with aging at 373 K for 100 h [55]

dislocation accumulation inside grains. This was demonstrated on pulsed electrodeposited Cu where the extraordinary strength (about 1 GPa) with reasonable ductility was observed [70]. In SPD-processed materials, nanotwins can be introduced via low-temperature processing and/or deformation at high strain rate. The first way was realized on the example of nanostructured Cu with twins produced by ECAP followed by cryogenic drawing and cryogenic rolling [71]. Dynamic plastic deformation (deformation at high strain rate) in combination with liquid nitrogen temperature allowed to increase dramatically the strength of Cu retaining ductility in [72]. The other approaches involve lowering stacking fault energy (SFE) to promote partial dislocation slip [73], the abovementioned low dislocation density and high-angle grain boundaries formation and multiple phases and phase transformations [74].

It is worth also noting that in the nanostructured metals processed by SPD, both strength and ductility can be improved by performing mechanical tests at lower temperature and/or high strain rate [68, 75]. As an example, Fig. 3.13 displays the tensile engineering stress–strain curves of UFG Ti with a grain size of 260 nm tested at room temperature and 77 K [67, 75]. At room temperature, the Ti has some ductility and a small uniform elongation, as shown by curve A obtained at a strain rate of 10^{-3} s^{-1}. However, at 77 K, the strength of the material is drastically elevated to $\sim$1.4 GPa. There is also a simultaneous increase in the elongation to failure, and this increases with strain rate up to a maximum close to $\sim$20 %, as shown in Fig. 3.13 where curves B–D are for strain rates of 10^{-3} s^{-1}, 10^{-2} s^{-1}, and 10^{-1} s^{-1}, respectively. These results for strength and ductility are better than, or at least comparable to, those of Ti alloys with a high percentage of alloying elements. Here, pronounced necking is delayed even for this very strong metal, resulting in a large area under the stress–strain curve and a generally tough behavior of the material. For comparison, curve E shows the initial 18 % of strain for a conventional coarse-grained Ti sample tested at 77 K [67].

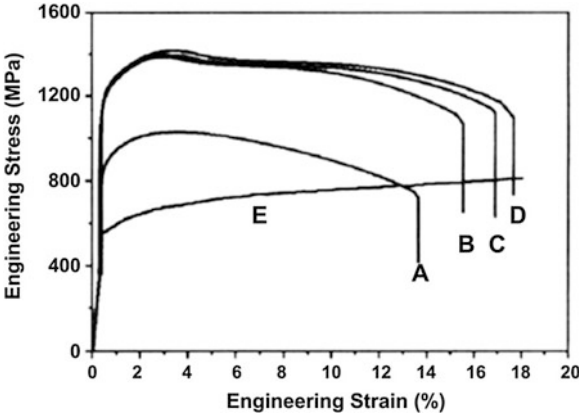

Fig. 3.13 Engineering stress–strain curves for nanostructured Ti where *curve A* is for testing at room temperature at a strain rate of 1×10^{-3} s^{-1} and *curves B–D* for the same Ti tested at 77 K for strain rates of 1×10^{-3} s^{-1}, 1×10^{-2} s^{-1} and 1×10^{-1} s^{-1}, respectively; for comparison, curve E shows the behavior of coarse-grained Ti over the initial 18 % of strain when testing at 77 K [67]. The curves are reproduced from [75] with the permission from the publisher

Another fundamental concept to control ductility is based on manipulation with strain rate sensitivity of material (Eq. 3.5). The UFG Cu with high ductility was found to have higher strain rate sensitivity, m, which is defined as $\{d\ln\sigma/d\ln\dot{\varepsilon}\}$ where σ is the applied stress and $\dot{\varepsilon}$ is the strain rate [54]. Indeed, nanostructured materials as a rule have small strain hardening rate that means a limited capability to store dislocations inside grains. The increased strain rate sensitivity would mean that a mixture of grain boundary sliding and dislocation slip operate the plastic flow, thus providing plastic deformation.

The value of m was equal to ~ 0.14 for ECAP-processed Cu taken through 16 passes compared with a value of m of ~ 0.06 for ECAP-processed Cu taken through only 2 passes. A high value for the strain rate sensitivity indicates viscous flow and renders the material more resistant to necking and, therefore, more ductile. Increased strain rate sensitivity was also revealed in a number of other studies [61, 76]. It was recently demonstrated that the m-value in the UFG Al alloys at room temperature can be increased up to 0.24 via manipulation with the chemical composition of grain boundaries [77] that can lead to the extraordinarily high ductility at room temperature. At the same time, there are also some reports illustrating low values of m in the SPD-processed materials. It is possible that these apparent differences are due to microstructural features in the samples since the microstructures formed during SPD processing may differ significantly depending upon the processing conditions.

As a rule, the ductility of UFG metallic materials is examined through tensile or compression tests representing uniaxial mechanical load. However, an additional question is peculiarity of deformation behavior of SPD materials under multiaxial loading typical for commercial metal-forming processes. Recent works showed that even at limited elongation to failure values measured by tensile tests, the SPD

materials can demonstrate the same technological plasticity as their coarse-grained counterparts [78]. This is attributed to heterogeneity of plastic flow combined with dislocation glide and grain boundary sliding. This makes SPD materials to be not only attractive research objects but also reliable candidates for advanced industrial applications from technological point of view even if their uniaxial ductility is reduced in comparison with their coarse-grained counterparts.

In conclusion, recent results show that grain refinement by SPD can lead to a unique combination of strength and ductility in metallic materials. Such superior mechanical properties are highly desirable in the development of advanced structural materials for the next generation [5, 11, 53]. However, the achievement of these properties is associated with the tailoring of specific microstructures which, in turn, are determined by the precise processing regimes and the nature of any further treatments. This strategy represents the art and science of nanostructuring for advanced properties using SPD techniques [14].

3.1.2 *Fatigue Properties of Nanostructured Metallic Materials*

Fatigue occurs when a material is subjected to repeated loading and unloading. If the loads are above a certain threshold, microscopic cracks will begin to form at the stress concentrators such as the surface, persistent slip bands (PSBs), and microstructural heterogeneities (second-phase precipitates, particles, pores, etc.). Eventually, a crack will reach a critical size, the crack will propagate suddenly, and the structure will fracture. The nominal maximum stress values that cause such failure may be much lower than the ultimate tensile strength or yield strength of material. Therefore, fatigue considerations are very important in materials engineering. There are three main forms of fatigue: high-cycle fatigue (HCF), low-cycle fatigue (LCF), and thermal–mechanical fatigue (TMF). In this chapter, we focus on HCF and LCF of nanostructured metallic materials. The principal distinction between HCF and LCF is the region of the stress–strain curve, where the repetitive application of load (and resultant deformation or strain) is taking place. HCF is characterized by low-amplitude high-frequency elastic strains, whereas LCF is the mode of material degradation when plastic strains are induced [79].

The fatigue properties of bulk nanostructured metallic materials have been widely studied over the last two decades, and comprehensive overviews of these activities can be found in [80–83].[1] Most of these investigations have clearly shown

[1]It should be noted that size of specimens is the main limitation for investigation of fatigue behavior of SPD-processed nanostructured metallic materials. Thus, in most of investigations, ECAP-processed objects were studied, which have size sufficient for the preparation of fatigue specimens. However, very recent modifications and/or upscaling of other SPD techniques, such as HPT, allowed fabrication of larger samples. Research on fatigue behavior of nanostructured metallic materials produced by other SPD techniques has just started [84].

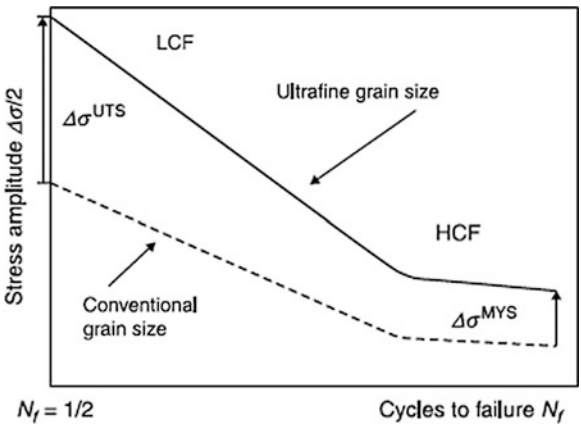

Fig. 3.14 Schematic Woehler (S–N) diagram showing the effect of grain refinement on fatigue life. The diagram is reproduced from [80] with the permission from the publisher

that the nanostructured metallic materials show enhanced fatigue life compared to the coarse-grained materials, which has been related to unique microstructure of nanostructured metallic materials and their enhanced mechanical properties. The outcomes of fatigue studies can be roughly generalized as follows: The higher the increase in fatigue life at a given amplitude, the higher the strength amplitude [80]. As nanostructured metallic materials have much higher enhanced ultimate tensile strength, the sustainable stress level at a given fatigue life is markedly increased in the LCF regime. As the stress amplitude decreases, the plastic strain amplitude decreases and work hardening is reduced. Therefore, in the HCF regime, the sustainable stress levels of nanostructured metallic materials at a given fatigue life are higher compared to those of the coarse-grained counterparts, but the difference is not that significant as in the LCF regime (as shown schematically in Fig. 3.14) [80].

3.1.2.1 High-Cycle Fatigue Behavior of Nanostructured Metallic Materials

Although grain refinement down to ultrafine or nanoscale can dramatically enhance tensile strength of metallic materials (see Sect. 3.1.1), their HCF properties are often not enhanced as significantly as tensile strength. For instance, the ratio of the endurance fatigue limit σ_{fo} to the ultimate tensile strength σ_{UTS} (σ_{fo}/σ_{UTS}) was found to be lower for most of the nanostructured metallic materials compared to their coarse-grained counterparts [80, 81]. This is clearly seen from Table 3.2, where data on mechanical properties of some nanostructured metallic materials produced via SPD are listed. However, a significant increase of this ratio was observed in some cases, for example, in the friction stir-processed AA7075 in [85] or in ECAP-processed Fe–36 % Ni Invar in [86].

Sometimes, standard thermo-mechanical processing might even lead to somewhat better HCF properties in the coarse-grained materials than in their nanostructured counterparts. This was demonstrated in comparison with HCF properties

Table 3.2 Mechanical properties of some nanostructured metallic materials produced via SPD

Material	Processing; grain size	$\sigma_{0.2}$ (MPa)	σ_{UTS} (MPa)	ε_f (%)	σ_{fo} (MPa)	σ_{fo}/σ_{UTS}	References
CP Cu	CG; d = 35 μm	140	240	–	65	0.27	[87]
	ECAP 10p; d = 0.2 μm	440	480	–	80	0.17	
AA5056	CG T6,	276	310	12	50	0.16	[88]
	ECAP 8p, d = 0.2 μm	392	442	7	116	0.26	[89]
AA6106Zr	CG, ST, AA	250	350	23	175	0.5	[90]
	ECAP 4p, d = 0.2 μm	570	590	9	225	0.38	
Fe–36 % Ni Invar	CG	275	490	40	137	0.28	[86]
	ECAP 12p, d = 0.18 μm	835	912	52	330	0.36	
CP Ti (VT1)	CG; d = 25 μm	380	460	26	238	0.52	[91]
	ECAP 8p; d = 0.3 μm	650	810	15	380	0.47	[92]
CP Ti (Grade 2)	CG; d = 105 μm	248	418	42	210	0.50	[93]
	CR; d = 15 μm	380	460	26	238	0.52	[94]
	ECAP 6p; d = 0.3 μm	635	669	33	350	0.52	[93]
Ti–6Al–4V	HR; d = 3 μm	900	930	20	550	0.59	[95]
	ECAP 4p; d = 0.16 μm	1340	1370	14	620	0.45	
SM490 steel	CG; d = 12.5 μm	424	691	25	275	0.40	[96]
	TMT; d = 0.8 μm	653	796	18	400	0.50	

d—grain size, $\sigma_{0.2}$—yield strength, σ_{UTS}—ultimate tensile strength, ε_f—elongation to failure, σ_{fo}—endurance limit (on the basis of 10^7 cycles and stress ratio R = −1), *CR*—cold-rolling, *HR*—hot-rolling, *ST*—solution treatment, *AA*—artificial aging, *TMT*—thermo-mechanical treatment, *CG*—coarse grained

of AA5056 and Al–Mg–Sc alloys in coarse-grained condition and after ECAP processing [97]. Such a little improvement (or no improvement) in fatigue life observed in the nanostructured metallic materials in HCF regime can be related to insignificant increase in resistance against crack nucleation in these materials, since the fatigue life in the HCF is determined by the resistance of material to the crack nucleation. As it is difficult for slip bands to pass through the HAGBs, intergranular cracking by piling up of dislocations at grain boundaries is more likely to occur at HAGBs than in grain interior or at LAGBs, where dislocations can be transported into adjacent grain by shear bands [98].

The HCF response in nanostructured metallic materials is also strongly determined by their chemical composition. For example, it was shown that increasing Mg content in the Al alloys resulted in longer fatigue life for the same stress amplitude [89, 99]. Significantly enhanced fatigue properties in high-cycle regime were also demonstrated by an AA6106 with Zr and Sc additions in [90] and by an Al–6Mg–Sc alloy in [100] that can be attributed to a higher content of Sc [100] or combination of Zr with Sc [90], resulting in a high volume fraction of strengthening

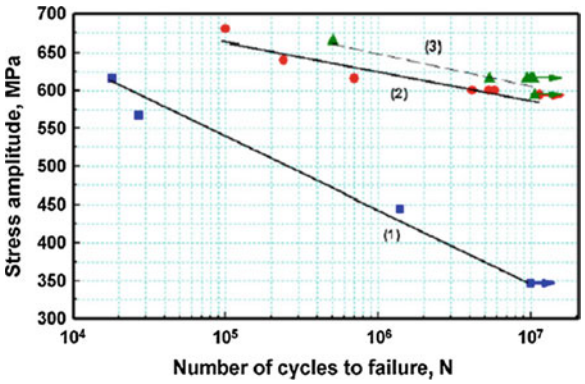

Fig. 3.15 Dependence of the stress amplitude on the number of cycles for smooth samples of coarse-grained CP Ti (*curve 1*), nanostructured CP Ti after ECAP and thermal mechanical treatment (TMT) (*curve 2*), and after ECAP + TMT and additional annealing at 350 °C for 6 h (*curve 3*). The figure is reproduced from [101] with the permission from the publisher

particles when optimum aging treatment is applied. Significant improvement of fatigue performance was reached via nanostructuring also in Ti-based materials. For example, in CP Ti, grain refinement via ECAP led to an increase in the fatigue limit by nearly 50 % [87, 101]. It can also be further enhanced, if the SPD-processed Ti is subjected to additional TMT and annealing, as shown in Fig. 3.15 [101]. Similar effect was also observed in the SPD-processed Ti–6Al–4V ELI alloy [95]. Notable improvement of HCF properties was observed in the ECAP-processed Fe–36 % Ni Invar (Table 3.2), which showed many advantages compared with other commercially available dimensionally stable alloys [86]. In particular, (i) the conventional yield stress increased after ECAP by a factor of 3 depending on the number of ECA passes; (ii) the improvement of HCF life by an order of magnitude was attained; (iii) the ductility of UFG Invar was also notably better than that of its conventional counterparts; (iv) due to this good ductility, the LCF properties were also significantly improved; and finally, (v) the resistance to crack propagation attested by LCF testing was regarded as rather high, supposing good reliability of ECAP-processed Invar in engineering applications.

In the very high-cycle fatigue (VHCF) regime, where the number of cycles to failure is much higher than 10^7, the fatigue life of the nanostructured pure metals remains high compared to the coarse-grained ones, as was observed in pure Cu [102] and pure Al [103]. However, the VHCF behavior of the nanostructured alloys can be influenced by their microstructure, since the strength of the weakest phase or weakest microstructural detail and the area of maximum localized plastic deformation determine the crack initiation sites in the VHCF regime [103].

3.1.2.2 Low-Cycle Fatigue Behavior of Nanostructured Metallic Materials

The LCF behavior of the nanostructured metallic materials is very complex, since ultrafine and nanograins have a low ability to sustain cyclic loads in the LCF regime. This was related to the limited ductility on monotonic and cycling deformation promoting early crack initiation as well as higher fraction of grain boundaries favorable for crack propagation in the nanomaterials [81]. Unlike coarse-grained metals, their nanostructured counterparts usually show no significant increase of stress amplitude (cyclic hardening) (Fig. 3.16) or its decrease (cyclic softening) when they are cyclically deformed under constant strain amplitude [97, 104, 105]. The cyclic softening ratio in this case is nearly zero (Fig. 3.17). This kind of response strongly depends on the chemical composition [97] and microstructure of metals and alloys [104] (Fig. 3.17). The nanostructure in the SPD-processed pure metals is usually unstable, both mechanically and thermally. Microstructural instabilities in the form of dynamic grain coarsening in the nanostructured pure metals (Fig. 3.18a) and/or formation of fatigue shear bands have been proposed (Fig. 3.18b) as possible reasons for softening effect [97, 104, 106].

For instance, UFG pure Al showed cyclic softening [81], whereas an increase of Mg content in the Al alloys suppressed cyclic softening and even increased cyclic hardening effect. Artificial aging of the cryorolled AA2024 introducing nanosized *S* precipitates in the microstructure resulted in little cyclic hardening (negative cyclic softening ratio), whereas naturally aged material showed cyclic softening [107] (Fig. 3.17). The LCF life is mainly controlled by fatigue crack propagation. The fatigue crack growth behavior in the nanostructured Al alloys was also found to be different from that in the coarse-grained ones [108–110]. The standard crack growth rate da/dN versus stress intensity factor range ΔK plots for the nanostructured materials showed the same stages of crack propagation as in the coarse-grained materials. However, the fatigue 'threshold' ΔK_{th} corresponding to

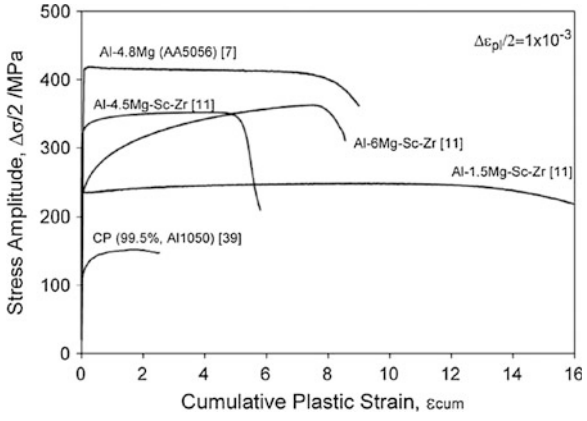

Fig. 3.16 Cyclic response of ECAP-processed Al and various Al–Mg alloys under the same constant plastic strain amplitude. The figure is reproduced from [81] with the permission from the publisher

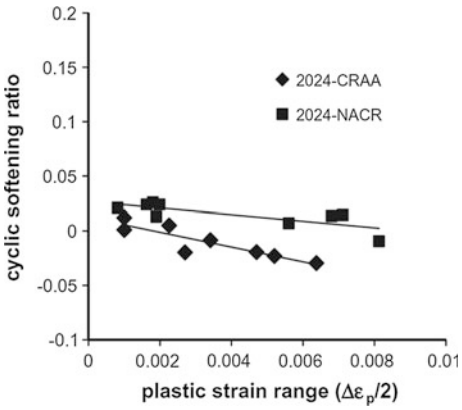

Fig. 3.17 Cyclic softening ratio as a function of strain amplitude for an Al2024 alloy produced via cryorolling followed by natural aging (NACR) or cryorolling followed by artificial aging (CRAA). This image is reproduced from [107] with the permission from the publisher

the low-end limit of the curves decreased after SPD processing in pure Al [109], AA5056 [110], and Al–1.5MgScZr [108].

SPD processing can lead to improvement of the LCF properties also in Mg alloys [111]. For example, ECAP processing (for 1–2 passes) of the AZ31B alloy led to significant improvement of the LCF life due to grain refinement as well as reorientation of grains, though it was reduced with further ECAP pressing. The orientation dependence (anisotropy) of the LCF properties in this material was also demonstrated [111]. The LCF life is mainly controlled by fatigue crack propagation. The fatigue crack growth behavior in the NS metals was found to be different from that in the coarse-grained counterparts [108–110]. The standard crack growth rate da/dN versus stress intensity factor range ΔK plots for the nanostructured materials showed the same stages of crack propagation as in the coarse-grained materials. However, the fatigue 'threshold' ΔK_{th} corresponding to the low-end limit of the curves decreased after SPD processing in CP Al and a range of Al alloys [108–110]. Similar results were reported for CP Ti [112], where ECAP processing reduced ΔK_{th} and led to the higher cyclic crack growth rate. A lower crack growth rate and a lower fatigue limit due to texture softening and reduction of crack nucleation resistance were reported for the ECAP-processed AZ31 alloy [113].

3.1.2.3 Strategies to Increase Fatigue Properties of Nanostructured Metallic Materials

Analysis of literature on fatigue performance of nanostructured metallic materials shows that intelligent microstructural design is the main approach to improve their fatigue behavior [80]. Microstructure of these materials can be tuned via optimization of the SPD processing parameters, such as temperature, strain, strain rate,

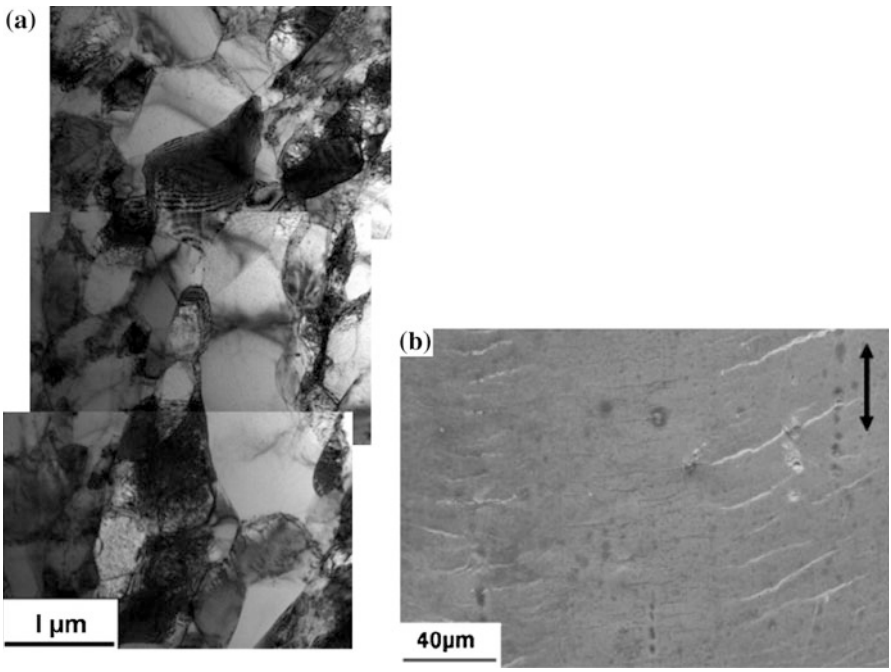

Fig. 3.18 **a** TEM image of the cryorolled CP Al fatigued at a strain amplitude of $\Delta\varepsilon_p = 0.0015$ showing the locally coarsened grains; **b** surface relief of face surface of cryorolled AA2024 tested at strain amplitude of $\Delta\varepsilon_p = 0.0056$ showing shear bands (*double arrow* indicates the stress axis). The images are reproduced from [104, 107] with the permission from the publishers

and strain path. Intelligent microstructural design can improve HCF properties dramatically. For example, a large enhancement in fatigue life by one order of magnitude in HCF regime was achieved in the AA6061 after a single ECAP pass leading to the formation of subgrains [98]. However, this effect disappeared after the alloy was pressed further for 4 passes due to significant increase of HAGB fraction. On the contrary, the AA2124 showed a higher fatigue life after 8 ECAP passes than that after 4 ECAP passes (Fig. 3.19), and complex microstructure consisting of grains/subgrains was observed in both conditions [114]. Microstructure evolution during SPD processing is determined to large extent by chemical composition of the material. Therefore, microstructure and fatigue properties can be also tuned via appropriate selection of kind and amount of alloying elements in the alloys.

Enhancement of ductility of nanomaterials is particularly useful for improvement of properties in the LCF regime, where plastic strain amplitudes dominate the fatigue life. The ductility of nanostructured metallic materials is often enhanced via their heat treatment after SPD which results in decrease of dislocation density in the interior of nanograins, as well as in relaxation of non-equilibrium grain boundaries. For example, this approach was successfully applied to nanostructured CP Ti in

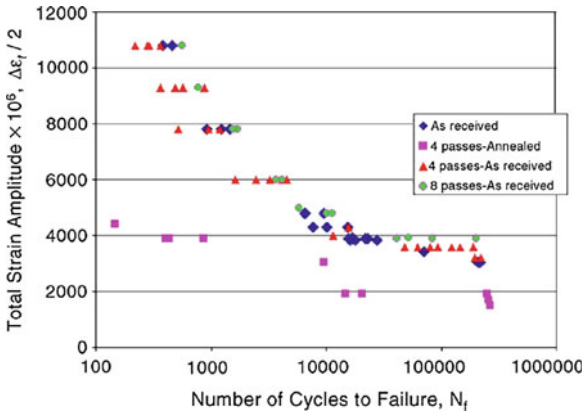

Fig. 3.19 Strain–life fatigue for the AA2124 in the coarse-grained condition and after ECAP for 4 and 8 passes. The image is reproduced from [114] with the permission from the publisher

[101] (Fig. 3.15). Very promising fatigue properties in the LCF and HCF regimes can be achieved by introducing the so-called bimodal grain size distributions, where nanograins having the size of several hundred nanometers are embedded into matrix of coarse grains having the size of several microns [81]. Such bimodal microstructures can be also generated via heat treatments of nanostructured metallic materials, though it cannot be done in every material.

Cyclic stability and fatigue life can be also enhanced via manipulation with shear banding. On the one hand, it was suggested that disposition of macroscopic shear banding should improve fatigue life [80]. This can be done, for example, via stabilization of nanostructures against growth of nanograins during cyclic deformation, as coarse grains can act as sites for the formation of shear bands. On the other hand, higher fatigue ductility and consequently higher fatigue life of cryo-rolled CP Al coincided with a much higher density of shear bands in [115]. It was shown that grain coarsening within the macroscopic shear bands increases the capacity of these shear bands to accommodate strain by eliminating the heavily worked regions from the shear band, allowing additional strain to be accommodated in those regions. These large strain-free grains are softer than their ultrafine-grained surroundings, and this encourages further localization of deformation within the shear bands [116]. However, such effect may not be expected in other nanostructured materials. Special attention should be paid to the as-SPD nanostructures formed in the material, since macroscopic shear bands can grow from shear bands induced into material during SPD processing.

3.1.3 Wear Resistance

Wear resistance is another very important property for metallic materials used in moving structural parts [117]. The wear of a component leads to an increased clearance and to loss of precision. For example, during the service of total joint

replacements, there are inevitable sliding contacts between the femoral cup and the tibial of acetabular head during motion of the human body. These contacts generate wear debris, and they produce a dimensional loss for the bioimplants that may cause serious health problems for the patient [118]. Therefore, a high wear resistance of material yields a longer service life of component. As is well known, the higher the strength, the better the wear resistance of metallic materials [117]. So, it could be expected that nanostructuring should improve this property. However, investigations show that there is no consistent effect of nanostructuring on wear properties. The obtained results are often contradictory and can be divided into three groups [119] as shown in Table 3.3.

1. ***Nanostructured metallic materials show increased wear resistance***. In [119], it was demonstrated that the wear resistance of the Al–2, 3, and 5 % Cu improves with increasing number of ECAP passes leading to increased hardness for all alloy compositions (Fig. 3.20a). This effect was found to increase with increasing load applied (Fig. 3.20a). Nanostructuring of the AA2024 via mechanical milling and hot pressing led to a dramatic reduction of the wear rate to 0.012 mg/m (0.079 mg/m for the coarse-grained T6 material) [120]. The friction coefficient was reported to decrease in the nanostructured AA6060 and AA2024 alloys [120, 121]. These effects were related to the increased hardness of the SPD-processed alloys since a clear correlation between the hardness and wear resistance was observed [119, 120]. Similar results were also observed on Zn-based alloys processed by ECAP [122, 123]. Nanostructuring of metallic materials can also affect the wear mechanisms [119, 120]. Analysis of the worn surfaces and wear debris showed that adhesion and delamination were mainly operating in the Al–Cu alloys and contribution of adhesion wear increased with increasing number of ECAP passes [119]. Both mechanisms were also reported for the AA6060 in both coarse-grained and UFG conditions, though less surface damage and smaller laminated debris resulting in a smaller wear mass loss were observed in the as-ECAP samples. Adhesive and abrasive wear mechanisms seen in the coarse-grained T6 AA2024 alloy were replaced by delamination and oxidation in the nanostructured AA2024 [120]. Adhesion as the dominant wear mechanisms was also reported for the HPT-processed Al–Al_2O_3 nanocomposites [124].
2. ***Nanostructuring of metallic materials does not affect their wear resistance***. In [125], the authors were surprised that significant improvement of mechanical strength in pure Ti (Grade 2) due to nanostructuring via ECAP processing did not lead to any improvement of its wear resistance independently on the applied pressure. This finding was mainly attributed to the tribochemical reaction leading to oxidative wear with the abrasive effect in Ti. As is well known, the dominant wear mechanism is the oxidative wear in pure Ti and also Ti alloys, which controls the weight loss during sliding. The studies on wear surface showed that a thick mechanically unstable oxide layer appeared on the sliding surface of the Ti samples in both coarse-grained and nanostructured conditions due to tribochemical reactions and frictional temperature [126] (Fig. 3.21). This

Table 3.3 Effect of SPD nanostructuring on wear properties of various metallic materials

Material	SPD method	Wear rig	Lubrication condition	Effect of SPD nanostructuring on friction coefficient	Effect of SPD nanostructuring on wear resistance	References
Al-1050	ECAP	Reciprocating sliding tester	Unlubricated	No effect	Decreases	[119]
Al–Al_3Ti	ECAP	Block-on-disk	n/a	n/a	No effect	[127]
Al–Cu	ECAP	Pin-on-disk	Unlubricated	n/a	Increases	[132]
Al–12 % Si	ECAP	Pin-on-disk	Unlubricated	n/a	Decreases	[129]
Al-1100	ARB	Pin-on-disk	Unlubricated	n/a	Decreases	[130]
Al-5052	ARB	Pin-on-disk	Unlubricated	n/a	Decreases	[130]
Al-6061	ARB	Pin-on-disk	Unlubricated	n/a	Decreases	[128]
Al–Al_2O_3	HPT	Ball-on-disk	Unlubricated	n/a	Increases	[124]
Cu–10 % Al–4 % Fe	ECAP	Ring-on-block	Unlubricated	Reduced	Increases	[133–135]
AZ61 alloy	ECAP	Pin-on-disk	Unlubricated	n/a	No effect	[128]
Low-carbon steel	SMAT	Reciprocating sliding tester	Unlubricated	Reduced	Increases	[136]
Low-carbon steel	ECAP	Pin-on-disk	Unlubricated	n/a	Decreases	[130]
Pure Ti	ECAP		Unlubricated	Reduced	Increases	[137]
Pure Ti	ECAP	SRV oscillating tester	Unlubricated	No effect	Increases	[138]
Pure Ti	HE	Pin-on-disk	Unlubricated	n/a	No effect	[139]
Pure Ti	HE	Pin-on-disk	Various conditions	n/a	Decreases	[139]
Pure Ti	ECAP	Pin-on-disk	Unlubricated	n/a	No effect	[125]
Pure Ti (Grade 2)	HPT	Microscratch testing	Unlubricated	No effect	Increases	[140]
Pure Ti (Grade 2) + TiN coating	HPT	Microscratch testing	Unlubricated	Reduced	Increases	[141]
TiNi	ECAP	Ring-on-block	Unlubricated	n/a	Increases	[142]
Zn–40 % Al–2 % Cu–2 % Si	ECAP	Pin-on-disk	Unlubricated	Reduced	Increases	[122]
Zn–8 % Al	ECAP	Block-on-ring	Lubricated by oil	n/a	Increases	[123]

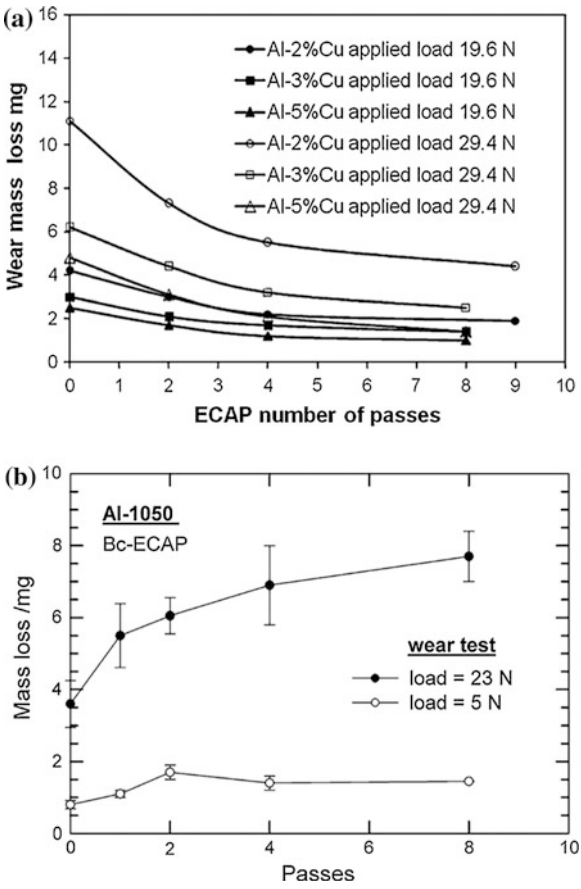

Fig. 3.20 **a** The effect of number of ECAP passes and the copper content on the wear mass loss in Al–2, 3 and 5 % Cu alloys (the sliding distance is 268.6 m under applied load of 29.4 N). The image is reproduced from [132] with the permission from the publisher; **b** the effect of number of ECAP passes on the wear mass loss in AA1050 at loads of 5 and 23 N. The image is reproduced from [119] with the permission from the publisher

Ti oxide layer plays a dominant role in determining the wear resistance of Ti independently of its grain size, so it 'masks' the effect of strengthening of nanostructure on the wear resistance. Wear-induced plastic deformation resulted also in microstructural changes in the subsurface regions (deformed region) due to the local thermal and thermo-mechanical processes. Nanostructuring of pure Ti resulted in thicker deformed region (Fig. 3.21). No significant effect of nanostructuring was seen in the Al–Al_3Ti composite in [127] and AZ61 Mg alloy in [128]. It should be noted that wear behavior of the composite materials is also determined by size and shape of reinforcements which can be affected by SPD processing.

3. ***Nanostructured metallic materials show degraded wear resistance***. Effect of number of ECAP passes on the wear mass loss in the AA1050 alloy is shown in Fig. 3.20b [119]. Wear mass loss gradually increases with increasing number of ECAP passes when a load of 29 N is applied although hardness of the material increases with increasing number of ECAP passes saturating only after 4 passes.

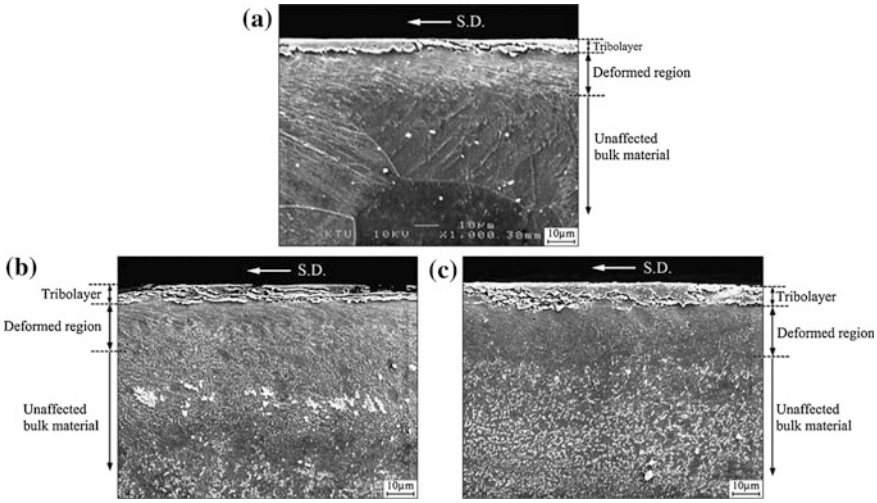

Fig. 3.21 Subsurface regions of **a** coarse-grained Ti and nanostructured Ti processed using ECAP through **b** 8E route and **c** 12E route. The wear tests were performed for a period of 2.63 h corresponding to a sliding distance of 10.40 km under a pressure of 1.5 MPa and at a sliding speed of 1.1 m s^{-1}. The image is reproduced from [125] with the permission from the publisher

At a lower applied load of 5 N, the wear mass loss slightly increases with increasing number of ECAP passes and saturates after 2 passes. No significant effect of ECAP processing on the friction coefficient was found [119]. Similar observations were reported for the Al–12 % Si alloy [129] processed by ECAP, CP Al [130, 131] and AA5052 [130] processed by ARB, and dual-phase steel processed by ECAP [130]. Analysis of the wear mechanisms showed that abrasive wear in the coarse-grained CP Al was replaced by delamination of the deformed surface layer in the ARB-processed material [131]. Higher oxidation rate leading to higher weight loss was reported for the ECAP-processed Al–12 % Si alloy [129]. ARB processing of the AA5052 resulted in significantly smaller wear debris [130], whereas an opposite effect was observed in the ECAP-processed AA1050 tested under load of 23 N [119]. A decrease of wear resistance in the Al alloys after SPD processing was mainly related to the loss of strain hardening capability [119, 130], to non-equilibrium grain boundaries [130, 131], and to intensive cracking at the interface of martensite and ferrite phases [130].

As it is clearly seen, no clear relationship between microstructure and wear properties can be outlined based on the available experimental results. Generally, wear mechanisms and wear properties are significantly affected by testing parameters such as applied load, sliding speed, application of lubricants, and pin material. More systematic studies on a wide range of SPD-processed metallic materials with greater respect to their microstructure are needed to optimize microstructural parameters in order to achieve high properties. Nevertheless, Table 3.3 clearly

demonstrates that various nanostructured metallic materials with increased wear resistance can be successfully fabricated by existing SPD techniques.

3.2 Improved Physical Properties

Nanostructuring of metals and alloys by SPD processing allows to improve various functional properties. This section focuses on the effect of nanostructuring on electrical conductivity, magnetic properties, and irradiation resistance of metallic materials.

3.2.1 Electrical Conductivity

Electrical conductivity is another very important functional property of metallic materials. Electrical conductivity in metals is a result of the movement of electrically charged particles. The atoms of metal elements are characterized by the presence of valence electrons—electrons in the outer shell of an atom that are free to move about. These 'free electrons' allow metals to conduct an electric current. Because valence electrons are free to move, they can travel through the lattice that forms the physical structure of a metal. Under an electric field, free electrons move through the metal much like billiard balls knocking against each other, passing an electric charge as they move [143, 144]. The transfer of energy is strongest when there is little resistance. On a billiard table, this occurs when a ball strikes against another single ball, passing most of its energy onto the next ball. If a single ball strikes multiple other balls, each of those will carry only a fraction of the energy. By the same token, the most effective conductors of electricity are metals that have a single valence electron that is free to move and causes a strong repelling reaction in other electrons. This is the case in the most conductive metals, such as Ag, Cu, and Au, which have a single valence electron that moves with little resistance and causes a strong repelling reaction. Al with three valence electrons comes as the fourth most conductive metal. Their properties are compared in Table 3.4. Ag and

Table 3.4 Properties of pure metals with the highest electrical conductivity

Metal	Electrical conductivity (MS/m)	Electrical resistivity[2] (10^{-8}, Ω m)	Density (g/cm^3)	Melting point (°C)
Silver	62.1	1.6	10.5	961
Copper	58.5	1.7	8.9	1083
Gold	44.2	2.3	19.4	1064
Aluminum	36.9	2.7	2.7	660

[2]Resistivity is the opposite of electrical conductivity, evaluating how strongly a metal opposes the flow of electric current

Au are noble metals and do not attract much interest of engineering due to extremely high price. Cu and Al are currently the most widely used metals in electrical engineering and electronics.

Mechanical strength and electrical conductivity are the most important properties of conducting materials. However, high strength and high electrical conductivity are mutually exclusive in metallic materials, and trade-off between strength and conductivity is always encountered in developing conducting materials [157]. Pure Cu and Al having high electrical conductivity show very low mechanical strength (Table 3.5). The alloying of pure metals, strain hardening, or introduction of precipitates dramatically improve their mechanical strength due to suppression of dislocation glide. But all strengthening methods lead to a degradation of electrical conductivity, since the latter is determined by the scattering of conductive electrons due to disturbances in the crystal structure including thermal vibrations, solute atoms, and crystal defects [158]. This is clearly seen from the electrical conductivity–yield strength plot for coarse-grained pure Cu and its alloys presented in Fig. 3.22: The electrical conductivity of most conventional Cu alloys ranges from $\sim$30 to $\sim$85 % of International Annealed Copper Standard (IACS).

The key to making strong but conductive metals is to generate an appropriate microstructure in which dislocation glide is effectively blocked, while the scattering of conducting electrons is minimized. The effective resistivity of a metal ρ, by virtue of Matthiessen's rule, is normally written as

$$\rho = \rho_T + \rho_R, \tag{3.6}$$

where ρ_R is called the residual resistivity and is due to the scattering of electrons by lattice defects and impurities [158]. For nearly perfect crystals of high purity, the resistivity is dominated by phonon scattering ρ_T which is temperature dependent and nearly linear in absolute temperature. For polycrystalline metallic materials, the temperature-independent residual resistivity ρ_R can be split up into several contributions as [152, 156]

$$\rho_R = \rho_{ss} + \rho_p + \rho_d + \rho_v + \rho_{gb}, \tag{3.7}$$

where ρ_{ss} is the resistivity due to scattering of solute atoms dissolved in the matrix, ρ_p the resistivity added by second-phase particles, ρ_d and ρ_v resistivity due to dislocations and vacancies, and ρ_{gb} resistivity due to scattering on grain boundaries. It should be noted that the ρ_p part in turn can consist of several parts if several types of second-phase precipitates (such as Guinier–Preston zones, non-coherent precipitates, coherent precipitates) are present in the microstructure. In alloys, the ρ_{ss} and ρ_p parts provide the highest contribution to its effective resistivity, whereas scattering of electrons at grain boundaries (i.e., ρ_{gb} part) is insignificant. As it was discussed in Sect. 3.1.1, grain size hardening provides the highest contribution to total strength of nanostructured metallic materials. Therefore, pure nanostructured metals should demonstrate much higher strength with slightly lower conductivity compared to their coarse-grained counterparts. This was first demonstrated by Lu

Table 3.5 Mechanical properties of some nanostructured Cu- and Al-based materials produced via SPD

Material	Processing; grain size d	Yield strength (MPa)	Ultimate tensile strength (MPa)	Elongation (%)	Electrical conductivity at RT, IACS (%)	References
99.95Cu	CG	62	172	40	~100	[145]
99.96Cu	ECAP 8p; d = 0.44 μm + coarser grains	360*	375*	–	96	[146]
HP Cu	PED; d = 0.4 μm + nanotwins	900	1068	12	96.9	[70]
HP Cu	DPD at LNT; d = 66 nm + nanotwins	610		8	95	[147]
99.999Cu (powder)	BM at LNT; d = 54 nm	688	770	7*	51	[148]
OF Cu	ARB 8 cycles; $w \approx 400$ nm	360*			96*	[149]
DLP Cu	ARB 8 cycles; w = 190 nm	472			74*	
Cu–1Fe–0.017Pb	CG	160*			90*	
	ARB 8 cycles; $w \approx 250$ nm	405*			85*	
ADS Cu–0.5Al_2O_3	ECAP 4p; d = 0.37 μm	525#*	535*	14.3*	86.7	[150]
ADS Cu–1.1Al_2O_3	ECAP 4p; d = 0.35 μm	565#*	575*	15.8*	81.8	
Cu–0.36Cr	ECAP 8p + AA;	390*	445	23	77	[151]
Cu–0.44Cr–0.21Zr	ECAP 8p + AA;	690*	710	12	76	
Cu–0.8Cr–0.05Zr	ECAP 8p + AA; d = 0.2 μm	580*	595	14	78	
Cu–5 at.%Nb	MA + compaction at 600 °C; d = 17 nm	1090*			25	[152]
	MA + compaction at 600 °C + AA at 900 °C; d = 40 nm	~1000			~50	
Cu–0.5Cr–0.12Ag	CG HT;	295*	430	20*	75	[153]
	HPT at RT; d = 0.2 μm	480*	530*	13*	30*	
	HPT at RT + AA at 450 °C; d = 0.2 μm + nanoprecipitates	820*	840	10	85	
99.5Al	CG	28	76	39	61.3	[145]
AA6201	CG T81	310	331	6	54	
Al–0.60Mg–0.45Si	ECAP-PC 6p + AA; d = 0.5 μm +nanoprecipitates	275	289	14	55.7	[154]
AA6060	CG T6		250	8	53.6	[155]
	HPT at RT; d = 0.18 μm		525	5	51.8	
	HPT at 180 °C; d = 0.35 μm + nanoprecipitates		347	7	58.1	

(continued)

Table 3.5 (continued)

Material	Processing; grain size *d*	Yield strength (MPa)	Ultimate tensile strength (MPa)	Elongation (%)	Electrical conductivity at RT, IACS (%)	References
AA6063	CG, SST		100	25	52.9	[155]
	Coarse grained, T6		200	14	54.5	
	UFG, ECAP-PC at 100 °C		264	13	51.8	
	UFG, ECAP-PC at 100 °C + aging at 130 °C		308	16	58.6	
AA6201	CG T81; d = 65 μm		330	6.1	53.6	[156]
	HPT at RT; d = 0.13 μm		510	2.5	47.7	
	HPT at RT + HPT at 130 °C; d = 0.28 μm + nanoparticles		412	4.9	55.6	
	HPT at RT + HPT at 180 °C; d = 0.44 μm + nanoparticles		365	8.8	58.4	

d—grain size, *w*—mean spacing of high-angle lamellar boundaries, IACS—International Annealed Copper Standard, HP—high purity, AA—artificial aging, TMT—thermo-mechanical treatment, CG—coarse grained, OF—oxygen free, DLP—deoxidized low phosphorous, PED—pulsed electrodeposition, ADS—alumina dispersion strengthened, MA—mechanical alloying, DPD—dynamic plastic deformation, BM—ball milling, RT—room temperature, LNT—liquid nitrogen temperature
Chemical composition of materials is provided in wt%, if not otherwise specified
*The value is estimated from experimental curves provided in the given reference
#0.5 % offset strength

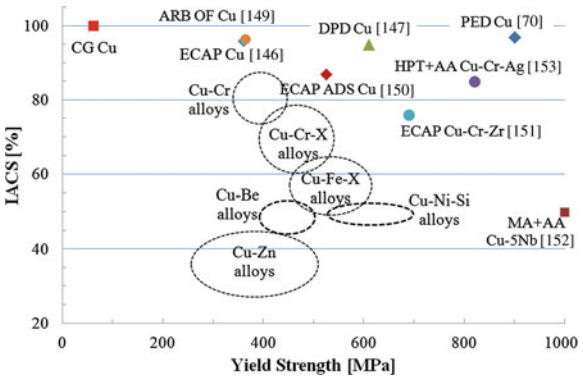

Fig. 3.22 Room temperature electrical conductivity (in IACS) versus yield strength for CG pure Cu and Cu-based alloys and their nanostructured counterparts obtained via SPD processed

et al. [70] on nanostructured Cu foil of high purity synthesized by pulsed electrodeposition technique. Nanograins with an average size of 400 nm had a high density of nanotwins of the {111}/[112] type with perfectly coherent and atomically sharp twin boundaries, which also act as strong barriers to dislocation motion, thus providing additional strengthening effect. This nanocrystalline Cu with the average twin/matrix lamellar thickness of 15 nm demonstrated unique combination of extremely high yield strength of 900 MPa and electrical conductivity of 96.9 % of IACS at room temperature (Table 3.5), which was just a few percent less than the conductivity of oxygen-free (OF) high-conductivity coarse-grained Cu [70]. The slightly elevated resistivity of the nano-Cu was ascribed dominantly to the intrinsic grain boundary scattering [159]. Since the technological applications of foils are very limited, further research activities focused on fabrication of bulk nanostructured Cu with similar properties. In [147], the same research group successfully applied dynamic plastic deformation at liquid nitrogen temperature to Cu cylinders with 18 mm in diameter and 25 mm in height. Such processing conditions ensured effective suppression of dislocation recovery, and the critical stress required for twinning was exceeded. The as-processed bulk Cu samples had nanostructure with an average grain size of 66 nm and nanoscale twins showing yield strength of 610 MPa and electrical conductivity of 95 % of IACS at room temperature (Table 3.5) [147]. Higuera-Cobos and Cabrera [146] subjected bulk CP Cu samples to ECAP processing resulting in the formation of bimodal microstructure with some coarse grains (several micrometers in size) embedded into UFG matrix with an average grain size of 440 nm. Again, a good combination of enhanced yield strength, 360 MPa, and high electrical conductivity, 96 %, of IACS, was found (Table 3.5). UFG sheets of OF Cu and deoxidized low phosphorous (DLP) Cu showing similar level of properties were successfully processed via ARB by Takata et al. [149]. However, high-strength nanocrystalline Cu obtained via two-step ball milling process and in situ consolidation demonstrated very low electrical conductivity of 51 % of IACS in [148]. Such significant degradation of electrical conductivity was related to impurities induced from the balls and jar during milling

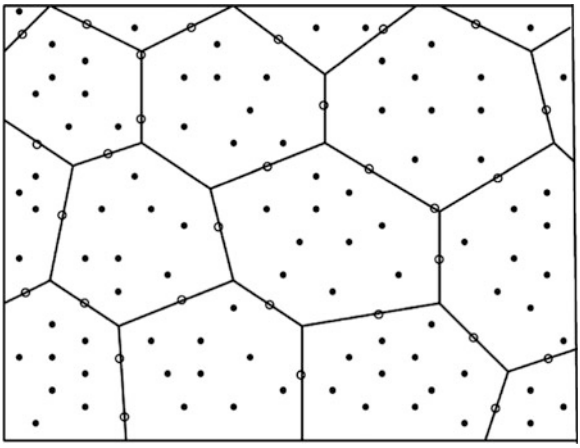

Fig. 3.23 Nanostructure with nanodispersed particles to be achieved to demonstrate a combination of high strength, good electrical conductivity, and enhanced thermal stability in alloys

process as well as to some possible micro- and nanoscale porosity significantly contributing to the resistivity.

In the alloys, nanostructuring provides unique opportunity to improve dramatically both mechanical strength and electrical conductivity. Enhanced mechanical strength can be achieved due to grain size hardening and dispersion hardening (see Sect. 3.1.1). Analysis of Eq. 3.7 shows that matrix should be maximally purified from the solute atoms and the most effectively scattering second-phase precipitates in order to minimize the scattering of conducting electrons in the microstructure and, thus, to further enhance the electrical conductivity [156]. This new approach illustrates the schematic presentation of an 'ideal nanostructure' to be achieved in the alloys to demonstrate a combination of increased strength, electrical conductivity, and thermal stability (Fig. 3.23). The nanoprecipitates in such structure should be the least scattering conductive electrons, and their significant amount should be located in the grain boundaries, thus suppressing mobility of grain boundaries and grain growth. Such nanostructures can be generated via SPD processing in two ways:

1. *Nanostructuring of alloy* (*solid solution*) via *SPD processing at ambient temperature followed by artificial aging for precipitation*. SPD processing at room temperature typically can result in significant grain refinement down to nanoscale, whereas the subsequent artificial aging leads to decomposition of solid solution, i.e., reduction of content of solute atoms in the matrix, and formation of nanoprecipitates of the required morphology. For example, in the case of the Al–Mg–Si alloys, one should avoid GP zones and β'' precipitates as conductive electrons are most effectively scattered on these types of precipitates. This approach was successfully applied to the Cu–0.5Cr–0.12Ag alloy in [153]. The solution-treated material was subjected to HPT processing at room temperature which led to grain refinement (Fig. 3.24a), improvement of mechanical strength to 480 MPa, and reduction of electrical conductivity from 75 to 30 % (Table 3.5). The subsequent artificial aging dramatically increased both yield

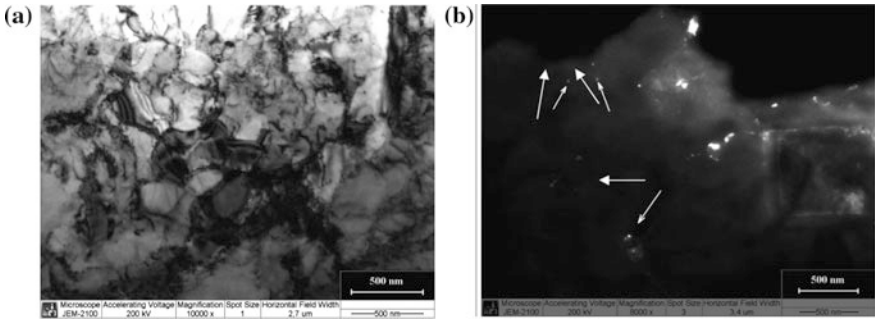

Fig. 3.24 **a** Nanostructure in the Cu–0.5Cr–0.12Ag alloy after HPT processing at RT; **b** formation of Cr nanoparticles (*marked by arrows*) in the nanostructure presented in (**a**) during artificial annealing at 500 °C for 30 min

strength to 820 MPa and electrical conductivity to 85 % due to decomposition of solid solution and formation of Cr nanoparticles (Fig. 3.24b; Table 3.5). It should be noted that precipitation kinetics is accelerated in the SPD-processed alloys due to higher diffusion coefficient because of high density of lattice defects and increased volume fraction of grain boundaries [160–162]. Therefore, a careful study of the effect of artificial aging parameters (temperature and time) on the microstructure and properties needs to be performed in order to determine the optimum aging parameters for given alloy after given SPD processing.

2. *Nanostructuring of alloy* via *SPD processing at elevated temperatures* (*250–500 °C for Cu alloys, 100–200 °C for Al alloys,* etc.) Grain refinement during SPD processing of alloys at elevated temperatures can be accompanied by dynamic aging which manifests itself in decomposition of supersaturated solid solution and formation of nanoprecipitates [153, 154, 156, 163, 164]. This effect has been related to significantly enhanced dislocation density and vacancy concentration leading to a dramatic increase of effective diffusion coefficient during SPD processing of alloys [161, 165]. This results in accelerated precipitation kinetic as the latter is controlled by diffusion of solute atoms [166]. For instance, it was observed on friction stir-processed AA2024 alloy that plastic deformation increases the precipitation kinetics at the temperatures below 300 °C [166]. At higher temperatures, the influence of plasticity on the volume fraction of precipitates was negligible. In [162], evolution of second-phase precipitates during ECAP processing of the AA7136 at 200 °C was found to be 50 times faster than during conventional aging treatments at the same temperature. Similar observations were also reported for the Al–Zn–Mg alloys in [20]. In the presence of deformation during the heat treatment, the precipitate morphology can be profoundly modified. In [167], dynamic aging during ECAP-PC processing of an AA6061 at 100 °C led to the formation of spherical β' nanoprecipitates, although rod-shaped β' precipitates are typically formed in this alloy during conventional artificial aging. This was attributed to the strong dislocation activity during ECAP processing and the resulting shear of precipitates.

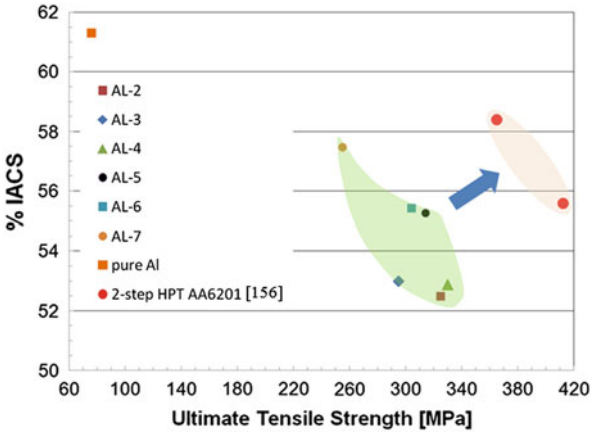

Fig. 3.25 Electrical conductivity (in IACS) of the various Al–Mg–Si alloys (AL-2–AL-7) used in electrical engineering for overhead power lines is plotted versus their ultimate tensile strength [168] and compared with the properties of a nanostructured AA6201 produced by two-step HPT processing [156]

In the recent new strategy [156], SPD processing at room temperature provides grain refinement in alloy, while further SPD processing promotes purification of matrix from solute atoms and second-phase precipitates of undesired morphology (ies). In some cases, just SPD processing at elevated temperatures is sufficient to achieve required nanostructure. In Fig. 3.25, electrical conductivity and strength of some commercial Al–Mg–Si alloys used for overhead power lines [168] are compared with the properties of nanostructured AA6201 alloy after two-step HPT processing (HPT processing at room temperature followed by HPT processing at elevated temperature). It is seen that the latter processing led to dramatic improvement of both electrical conductivity and strength (Table 3.5; Fig. 3.25).

Very recent research activities have focused on the effect of nanostructuring via SPD processing on superconductivity of superconductors [169–171]. It was reported that HPT processing not only improves mechanical strength in Nb (which is a well-known superconducting metal), but also increases the critical temperature for superconductivity due to the quantum confinement effect and size-independent superconductivity (Fig. 3.26), while the critical current density increases after HPT because of the vortex-pinning effect by lattice defects such as dislocations and grain boundaries [169].

However, an opposite behavior was demonstrated by the HPT-processed Nb–47 wt% Ti alloy (material for superconducting magnets) in [171]. The transition temperature in this material initially decreased with increasing shear strain and saturated to a steady-state level at large shear strains ($\gamma > 800$). This observation was rationalized based on dissolution of Ti in Nb during HPT processing. Further annealing of the HPT-processed specimens resulted in the elemental decomposition and enhancement of transition temperature and mechanical strength.

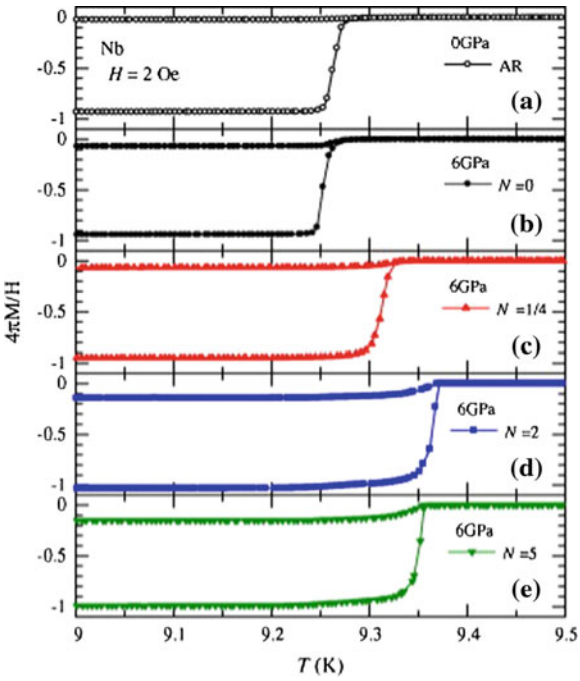

Fig. 3.26 Temperature dependence of the magnetization $M(T)$ of Nb in the magnetic field $H = 2$ Oe: **a** as-received coarse-grained material. **b–e** HPT-processed samples with different revolution numbers N. The figure is reproduced from [169] with the permission from the publisher

It can be outlined that nanostructuring of conducting materials can provide unique opportunity to dramatically improve mechanical strength without significant degradation of electrical conductivity in pure metals, whereas both strength and conductivity can be significantly enhanced in alloys via intelligent nanostructural design. Nanostructuring also appears as an effective approach to achieve both high strength and enhanced superconductivity in superconductors.

3.2.2 Magnetic Properties

Most of magnetic materials of industrial interests are ferromagnetic materials. Ferromagnetic materials with the demagnetized state do not show magnetization although they have spontaneous magnetization. This is because the ferromagnetic materials are divided into many magnetic domains. Within the magnetic domains, the direction of magnetic moment is aligned. However, the direction of magnetic moments varies at magnetic domain walls so that it can reduce the magnetostatic energy in the total volume. When domain wall can easily migrate, the ferromagnetic material can be easily magnetized at low magnetic field. This type of ferromagnetic materials is referred to as ***soft magnetic material*** and is suitable for applications of magnetic cores or recording heads. When domain wall is difficult to migrate,

magnetization of the ferromagnetic material occurs only when high magnetic field is applied. In other words, this type of ferromagnetic materials is difficult to magnetize, but once magnetized, it is difficult to demagnetize. These materials are referred to as ***hard magnetic materials*** and are suitable for applications such as permanent magnets and magnetic recording media [172].

Soft magnetic materials are one of the most investigated classes of functional materials. Their microstructure can be amorphous or crystalline with grain sizes ranging from some nanometers in nanocrystalline soft magnetic materials to several centimeters in transformer steels [172]. Most of them are available as powders, ribbons, and thin films and are used in a huge variety of industrial applications such as motors, generators, transformers, sensors, or microelectronic devices. Earlier investigations showed the strong influence of nanostructuring via SPD on magnetic hysteresis characteristics of soft magnetic metals, such as Ni [173, 174], Co [175], Fe, and Fe–Si [176]. A sharp increase in the coercivity Hc was revealed in pure metals after SPD processing. It was demonstrated that coercivity in nanostructured pure Ni strongly depends on grain size, dislocation structure, and the non-equilibrium state of the grain boundaries [174]. For example, SPD-processed specimens subjected to recovery annealing at 100 and 200 °C had different values of coercivity by $\sim$40 %, though their grain sizes were nearly the same. At the same time, at 200 °C, an intense recovery of non-equilibrium grain boundaries was observed. As the temperature of annealing increased, a further decrease in the value of Hc was correlated with increasing grain size. An analogous regularity was revealed in Co processed via HPT [177]. TEM investigations of the domain structure of nanostructured Co with a grain size of about 100 nm used the Lorentz method. It was established that the magnetic domain sizes were significantly larger than the grain sizes and remagnetization was conditioned by the movement of domain walls, but at the same time, this movement was hampered by non-equilibrium grain boundaries.

In [176], five sets of soft magnetic metals, such as pure Fe, pure Ni, Fe–3 wt% Si, Fe–6.5 wt% Si, and Fe–17 wt% Co, were subjected to HPT processing at different temperatures (−196, 20, and 450 °C) up to strain levels, where a saturation of the microstructural refinement was observed. Depending on the material, the average grain sizes in the steady state varied from 300 nm at 450 °C to 30 nm at −196 °C. The coercivity was characterized in a magnetic closed system by using ring-shaped samples. Magnetic measurements obtained on ring-shaped samples give a much higher accuracy for determining the coercivity. The coercivity of the deformed materials first increased with decrease in grain size (Fig. 3.27). Once the crystallite size was far below 100 nm, the coercivity showed a strong decrease (Fig. 3.27). When the grain size becomes comparable to the magnetic exchange length, coupling over the grain boundaries occurs [178]. For magnetic materials, a maximum in coercivity versus the grain size occurs at the single-domain particle size, which is close to a grain size of about 100 nm, however depending on the material parameters (anisotropy energy, etc.). At this grain size, a pinning of the domain walls at grain boundaries can be expected. For smaller grain sizes, the

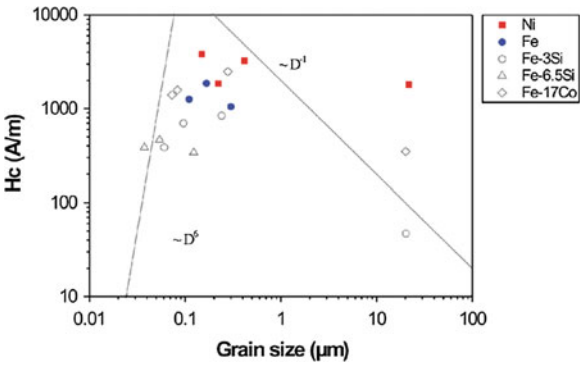

Fig. 3.27 Coercive force H_C as a function of the grain size for five soft magnetic materials. The figure is reproduced from [176] with the permission from the publisher

'effective' anisotropy is reduced due to exchange coupling which causes a dramatic reduction of coercivity with decrease in grain size.

A significant increase in the coercive force was also observed in hard magnetic alloys (such as Fe–Pd [179], RE–Fe–B [180–184], Fe–Cr–Co [185], and Cu–Co [186, 187]) processed by SPD. This is very important for practical applications and manufacturing of permanent magnets. However, the origin of Hc changes in these alloys has a more complex character and it is caused not only by the formation of a nanostructure but also by changes in the phase composition. For example, as in R–Fe–B (RE = Nd, Pr) system alloys which have attracted much research and practical interest in recent years. These alloys are used for fabrication of sintered [188] and hot deformed [189] permanent magnets with record values of magnetic force. The influence of HPT at room temperature and subsequent annealing on magnetic properties and structural changes in the cast $Pr_{20}Fe_{73.5}B_5Cu_{1.5}$ alloy was studied in [184]. In addition to the basic tetragonal $R_2Fe_{14}B$ phase (2:14:1), bcc (α-Fe type) and hcp (Pr rich) phases were present in the initial cast alloy. The basic magnetic phase 2:14:1 was in the form of very coarse dendritic grains and α-Fe additions constituted about 8 vol%, while the non-ferrite hcp phase constituted 25 vol%. At small strains, the alloy was characterized by stable phase composition and formation of a substructure with a mean subgrain size of less than 300 nm and a high density of dislocations. With increasing strain, the amount of the 2:14:1 phase relative to the amount of the bcc phase decreased, and in the alloy with the high strain, an amorphous phase was observed within the whole sample volume, while the 2:14:1 phase and other crystalline phases were not detected. Such microstructural evolution has also significantly affected the magnetic properties of the $Pr_{20}Fe_{73.5}B_5Cu_{1.5}$ alloy. Figure 3.28 shows Hc values of the alloy processed to varying strain (HPT rotation angle). In the initial state, Hc of the alloy was 20 kA/m, whereas after upset straining, Hc increased to 192 kA/m, grew further with increasing rotation angle, and reached the peak value at the angle range of 2–5. Annealing of the deformed samples restored the phase composition of the initial

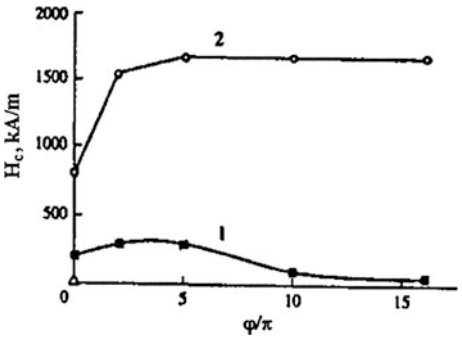

Fig. 3.28 Dependence of the coercitive force Hc of the $Pr_{20}Fe_{73.5}B_5Cu_{1.5}$ alloy in as-deformed (1) and annealed at 600 °C (2) conditions as a function of the HPT rotation angle (shear strain). The figure is reproduced from [184] with the permission from the publisher

alloy, but the grain size of the 2:14:1 phase did not exceed 300 nm and the amount of the α-Fe phase decreased sharply. As a result, annealing leads to a significant increase in the Hc value (Fig. 3.28). Thus, the application of the SPD method at room temperature with subsequent annealing resulted in a record value of Hc > 1600 kA/m for the $Pr_{20}Fe_{73.5}B_5Cu_{1.5}$ alloy. This value exceeded significantly the Hc values in permanent magnets fabricated from the same alloy via sintering or hot deformation.

In [179], a FePd alloy was nanostructured by severe plastic deformation following two different routes: Ordered and disordered states were processed by HPT. A grain size in a range of 50–150 nm was obtained in both cases (Fig. 3.29a, b). HPT induced some significant disordering of the long-range-ordered L10 phase. However, TEM analysis clearly showed that few ordered nanocrystals had remained in the deformed state. The deformed materials were annealed to achieve nanostructured long-range-ordered alloys. The transformation proceeded via a first-order transition characterized by the nucleation of numerous ordered domains along grain boundaries. The influence of the annealing conditions (temperature and time) on the coercivity was studied for both routes (Fig. 3.29d). It was demonstrated that starting with the disorder state prior to HPT and annealing at low temperature (400 °C) leads to the highest coercivity (about 1.8 kOe) (Fig. 3.29d).

There is also a body of research on magnetic properties of nanostructured Cu–Co alloys having a pronounced giant magnetoresistance (GMR) effect. In [186], the as-cast Cu–Co alloys with 2.2 and 4.9 wt% Co were subjected to HPT processing that dramatically refined the microstructure. For the as-cast Cu–2.2 wt% Co alloy, magnetization was only 79 emu/g_{Co} at the vanishing 1/H, which was about 50 % of the saturation magnetization for Co. After HPT, the alloy demonstrated typical superparamagnetic behavior without any tendency to saturation, namely J = 18 emu/g_{Co} at 1/H → 0, which was only about 11 % of pure Co. The absence of the saturation and such low J values in the Cu–2.2 wt% Co alloy were due to nanosize of all Co particles in the HPT samples, which was below the ferromagnetic limit for Co (4–10 nm). High fraction of coarser ferromagnetic Co grains in the Cu–2.2 wt%

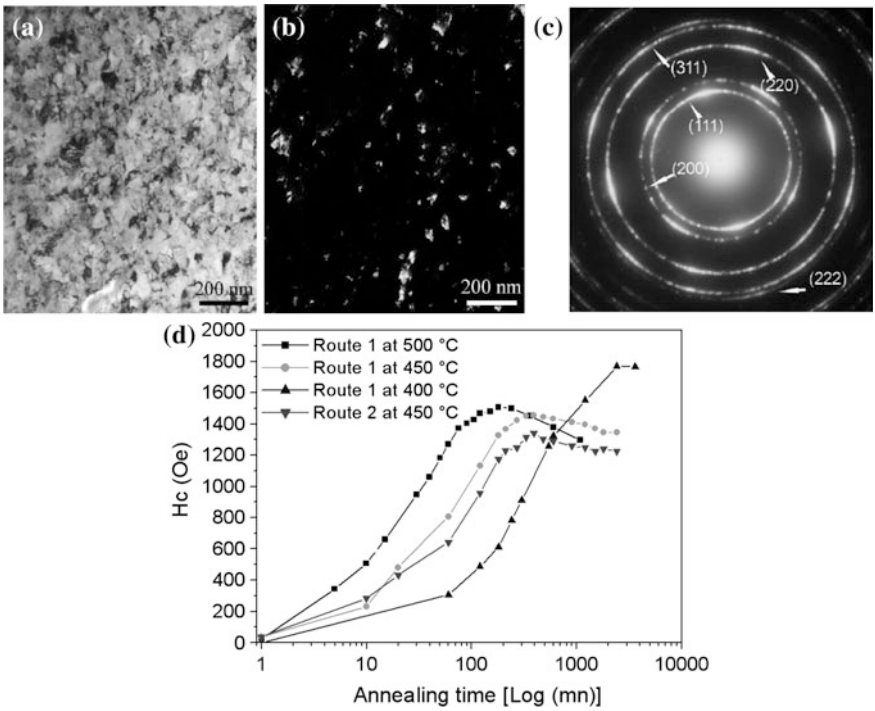

Fig. 3.29 TEM images of the FePd alloy processed by HPT (route 1—HPT of the disordered state); **a** *bright-field image* showing the nanoscaled structure, **b** *dark-field image* obtained by selecting with an aperture a part of the (111) fcc ring and showing few isolated nanoscaled grains, **c** SAED pattern with Debye–Scherrer rings characteristic of a polycrystalline structure with a very small crystallite size, **d** evolution of the coercivity of the FePd alloy processed by routes 1 and 2 as a function of the aging time for different temperatures. The figure is reproduced from [179] with the permission from the publisher

Co alloy resulted in a different behavior of the material. The magnetization of the as-cast alloy reached the saturation at J_s = 135 emu/g_{Co}. It was somewhat lower than the J_s for Co. The magnetization of the HPT-treated alloy did not saturate, although it was about three times higher at 1/H → 0 in comparison with the Cu–2.2 wt% Co alloy. Evolution of magnetic properties of the Cu–6.5 wt% Co alloy during ECAP processing with varying parameters was studied in [187]. The significant increase of the magnetic coercivity after first ECAP pass was related to a pinning effect of lattice defects for the movement of magnetic domain walls. Additional increase in the coercivity after further processing through route A was attributed to the refinement of the ferromagnetic Co particles to 10–30 nm through intense shear by ECAP. The magnetic anisotropy was prominent when the material was processed through route A, but was negligible through routes Bc and C (Fig. 3.30). The anisotropy occured because precipitate particles were successively elongated through route A with increasing number of ECAP passes, but they

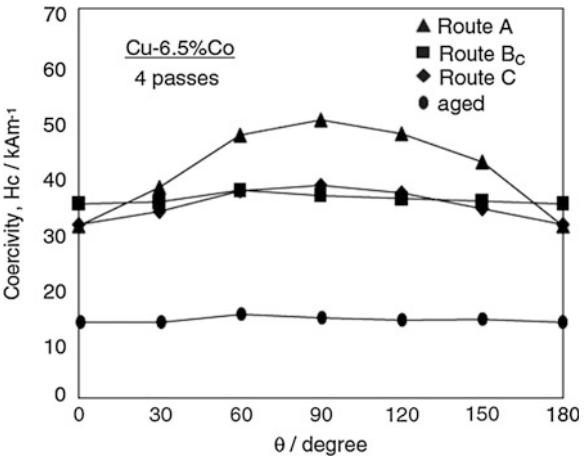

Fig. 3.30 Plots of coercivity with respect to rotation angle after 4 passes of ECAP through *route A*, *route* B_C, and *route C*. The figure is reproduced from [187] with the permission from the publisher (in the label, 'aged' stands for coarse-grained material)

reserved the original equiaxed shape while pressing through routes B_C and C after 2 passes.

SPD techniques have been also successfully utilized for compacting nanopowders. Metal–ceramic powder mixtures consisting of Co (ferromagnetic) and NiO (antiferromagnetic) phases were compacted by HPT both with and without a prior ball milling [190]. Enhanced coercivity of the obtained materials was ascribed to the Co particle size refinement, the increase of stacking faults, and the magnetic coupling between Co and NiO phases. Nanostructured Ni with an average grain size of 20 nm obtained via HPT consolidation of ball milled powders in [191] is another example. However, it should be noted that such materials are usually characterized by enhanced contamination and are often not fully dense, which can degrade their magnetic properties [191].

It is seen that intelligent nanostructural design using SPD processing and possibly further annealing treatments can dramatically improve magnetic properties of both soft and hard magnetic materials. The outstanding properties of nanomaterials arise from the fact that the grain size becomes comparable with the magnetic exchange length, which causes the so-called exchange domains resulting in strongly modified magnetic properties compared to the coarse-grained materials.

3.2.3 Irradiation Resistance of Bulk Nanostructured Metallic Materials

Global demand for electric power is being accelerating in present-day world from year to year. In view of the development of new types of reactors and a decrease of the traditional raw energy resources, this share will increase. Controlled nuclear fusion energy development will allow the mankind to generate the energy mainly by fusion reactors in the future. One of the challenges is the task of developing

radiation-resistant materials for advanced energy technologies [192, 193]. Indeed, the materials composing, for example, fusion components have to operate reliably in highly radiated environment. The properties of solids are subjected to be significantly modified by different kinds of high-energy particles and radiation fluxes (fast neutrons, γ- and *X*-radiation). Such irradiation causes changes in materials' microstructure expressed by irregularity in oriented crystal structure, radiation-induced defects (vacancies, clusters, dislocation loops, etc.) leading to degradation of their mechanical properties—bulging, limpness, accelerated creep of the radiation-exposed constructions.

Materials used in fission and fusion reactors are permanently in the conditions of irradiation by high fluxes of fast neutrons. Collisions of neutrons with atoms result in displacement cascades and the formation of non-equilibrium point defects such as vacancies, self-interstitials, and their clusters [193, 194]. At high doses of irradiation, these defects are accumulated that lead to a number of unwanted effects: radiation swelling (volume increase due to vacancies), radiation growth of anisotropic (textured) materials (a directional increase in one dimension), radiation creep, radiation work hardening, and simultaneous embrittlement [193–195]. In addition, nuclear reactions under the effect of neutrons result in the formation of a series of foreign elements with a subsequent accumulation of gaseous impurities and changes of phase composition. The most troublesome problems are the radiation swelling and growth, which change the shape and dimensions of fuel elements and other components of reactor cores, a decrease in thermal conductivity of fuel rod claddings and in the space between them that results in violations of the work regime of reactors and a decrease of the available fuel burn-up. In some materials, significant volume changes (up to several percent) are accumulated after the fluence of the order of $10^{23–26}$ m^{-2} that for typical values of the flux $10^{17–19}$ m^{-2} s^{-1} occurs in a few months [196]. These problems will be even more critical for fusion reactors, in which neutron flux is much higher than that in fast breeder reactors.

Therefore, a safe, reliable, and economical operation of nuclear power reactors critically depends on the radiation resistance of materials used in nuclear engineering. In view of this, fundamental research toward the development of radiation-resistant materials is a very important multidisciplinary task of condensed matter physics, materials science and nuclear engineering.

The rate of accumulation of radiation damages and related property changes to a great extent depend on the chemical composition and structure of materials. Thus, there are two main ways to decrease the harmful effects of irradiation. The first one is the change of main components of steels and alloys and doping by small additions of different elements. This method allows decreasing of one or two of the consequences of irradiation, but can result in a deterioration of other properties. For instance, austenitic steel has high mechanical properties but is largely prone to swelling, while another steel, ferritic–martensitic one, swells not much, but quickly embrittles [197–199]. For an efficient control of radiation resistance properties of materials, this first method is to be combined with the second one.

The second way to increase the irradiation resistance is the modification of microstructure, increase of the density of dislocations, and decrease of the grain

size. The reduction of defect accumulation rate in this case is associated with the sink role of dislocations and grain boundaries for vacancies and interstitials. Reduction of the grain size is especially efficient for this purpose. At grain sizes less than 10 μm, a drastic decrease of radiation swelling is observed [200]. Defect-free layers with the thickness of about 10–30 nm in the vicinity of grain boundaries are often observed [201]. In stainless steel, a decrease of the grain size from 3.7 to 0.5 μm results in an order of magnitude reduction in radiation swelling [196].

In this relation, nanostructured materials are currently attracting a considerable interest as potential radiation-resistant materials. Up to date, a few studies focused on the microstructure changes in nanocrystals during ion and proton irradiation have been carried out. In [202], through a measurement of electrical resistivity, it was shown that the accumulation of point defects in nanocrystalline Au with the grain size of 23 nm occurs significantly more slowly than that in a polycrystal with the grain size of 10 μm. In [203], electron microscopic studies of the microstructure of irradiated nanocrystalline Pd and ZrO_2 with varying grain sizes were carried out. The density of point defect clusters decreased by a factor of 3–4 when the grain size is reduced from 100 to 40 nm. For smaller grain sizes, no defects were observed.

In a series of papers [204–206], molecular dynamics simulations of the evolution of displacement cascades have been carried out for Ni nanocrystals with the grain sizes of 5 and 12 nm for primary knock-on atom values in the range from 5 to 30 keV. These studies have revealed significant differences in the formation of primary defects in nanocrystals from that in single crystals. Due to the high mobility of interstitials, these defects sink at grain boundaries and triple junctions and annihilate with the free volumes there. The structure of grain boundaries during this process does not change significantly. In the grains enriched by vacancies, stacking fault tetrahedra are formed similarly to single crystals. But in some cases, in nanocrystals, the vacancies are completely absorbed by grain boundaries. At high energies of primary knock-on atoms, dislocation networks are formed near grain boundaries upon the resolidification of a thermal spike region. These networks annihilate the excess volume associated with vacancies. The preferred sites for the sink of interstitials are grain boundary dislocations and triple junctions. Molecular dynamics simulations conducted in [207] also demonstrate that the grain boundary structure at the nanoscale regime strongly affects the primary radiation damage state, with the grain boundary acting as a sink for interstitials.

Thus, both the experimental data and simulations have demonstrated that grain boundaries and junctions in nanocrystals can efficiently absorb interstitials and hamper the accumulation of point defect clusters, thus resulting in slowing down the volume expansion due to displacement cascades.

However, the scarce data available to date do not allow drawing qualitative conclusions on the structure and mechanical property changes of nanomaterials under irradiation. Moreover, the results cited have been obtained using a model irradiation of thin nanocrystalline films by ions and thus do not allow one to make conclusions on the mechanical property changes of bulk materials under real reactor irradiation. Molecular dynamics simulations can predict the behavior of defects

only in a short timescale, and the role of grain boundaries in the evolution of defects during long-term irradiation has not been studied systematically.

In all of the cited works, nanocrystalline metals were prepared by inert gas condensation method which produced small-sized samples that limits the feasibility of studies of mechanical properties and especially of applications. To explore fully the potentials of the use of nanostructured materials in nuclear power engineering, a systematic study of the properties of bulk nanostructured materials under neutron irradiation is needed.

As it was already shown in Chap. 2, bulk nanostructured materials with advanced properties meeting the requirements of particular applications can be tailored by nanostructuring through SPD processing, which imposes extremely large plastic strain on materials without changing their geometry [208–214]. The most developed SPD method, ECAP, is especially attractive from the viewpoint of fabrication of structural nanomaterials for nuclear engineering.

Quite recently, proton irradiation experiments have been carried out on nanocrystalline Ni and Cu–0.5Al_2O_3 synthesized by ED and SPD [215]. In irradiated samples, no defects except for stacking fault tetrahedrons were observed and the density of the latter was much lower than that in coarse-grained polycrystals. Other studies on ion irradiation of nanocrystalline TiNi shape memory alloys [216] and nanostructured 316 stainless steel produced by HPT [217, 218] also testify a great potential of these materials as radiation-resistant ones. For example, X-ray studies of the TiNi alloy with a grain size of 23 nm showed no tendency for radiation-induced disordering of crystal structure (Fig. 3.31) [216]. These data inspire that SPD method will allow the fabrication of nanomaterials efficiently resisting radiation swelling and embrittlement.

The major weakness of most ion irradiation techniques is that the examined region usually is a fraction of a micron from the ion-incident surface which introduces some uncertainty in our ability to correlate the ion results with predicted bulk behavior attained during neutron irradiation. However, the data on the effect of high-dose neutron irradiation on stability of commercial nanostructured materials in the environment of real reactors are poorly presented in the literature. The first publications in this area were focused on the 321 stainless steel produced by ECAP [219] and low-carbon steel produced by ECAP-C [220, 221]. In [219], a study of ECAP 321 steel before and after the neutron irradiation at temperature $\sim$350 °C in the reactor BOR-60 with the maximum damage dose 5.3 dpa was carried out. The ECAP-processed steel demonstrated the thermal stability (up to 650 °C) of irradiation hardening after the neutron irradiation. However, the steel after ECAP was characterized by a rather wide distribution of grain sizes and substructures, so a conclusion of further studies to clarify and explain the observed regularities was drawn. Studies in [220, 221] focused on steel 10 produced by ECAP-C, which was subjected to neutron irradiation with the maximum dose of 1.37 dpa. High number densities of nano-Mn–Si-enriched precipitates were observed in both coarse-grained and UFG steels after irradiation (Fig. 3.32). However, the number density and the radius of the clusters were larger in the case of the UFG steels due to the shorter path that the defects need to diffuse before they reach the grain

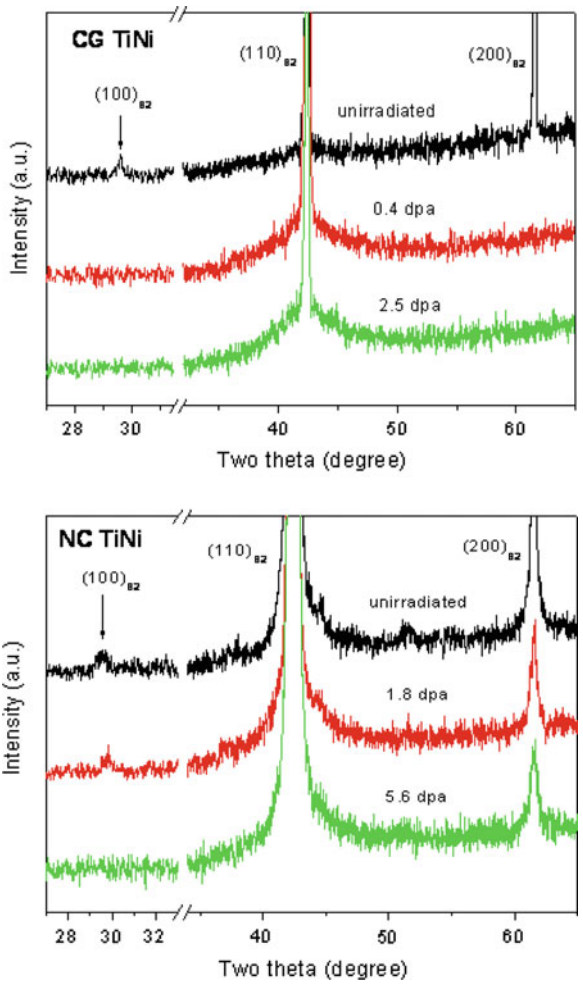

Fig. 3.31 X-ray studies revealed better irradiation resistance of nanostructured TiNi produced by HPT (with an average grain size of about 23 nm) as compared to CG TiNi (80 μm). The figure is reproduced from [216] with the permission from the publisher

boundary and hence less defect recombination probability in the matrix. The fact that these small clusters were not observed before irradiation confirms that their formation was radiation-induced. The hardness and strength of UFG steel showed minor changes after irradiation as compared to CG one indicating less radiation hardening effect (Fig. 3.33). The irradiation hardening in the UFG steel was mainly due to the irradiation-induced clusters. In general, UFG steel revealed better irradiation tolerance; however, the pronounced precipitation effects and stability of these nanoprecipitates should be carefully considered in future studies.

Thus, preliminary studies demonstrate that nanostructuring of metals by the use of SPD methods can be capable of producing new materials, which will have enhanced radiation resistance. To make a fundamental basis for the development of these materials, there is a need to study the processes occurring in nanocrystals

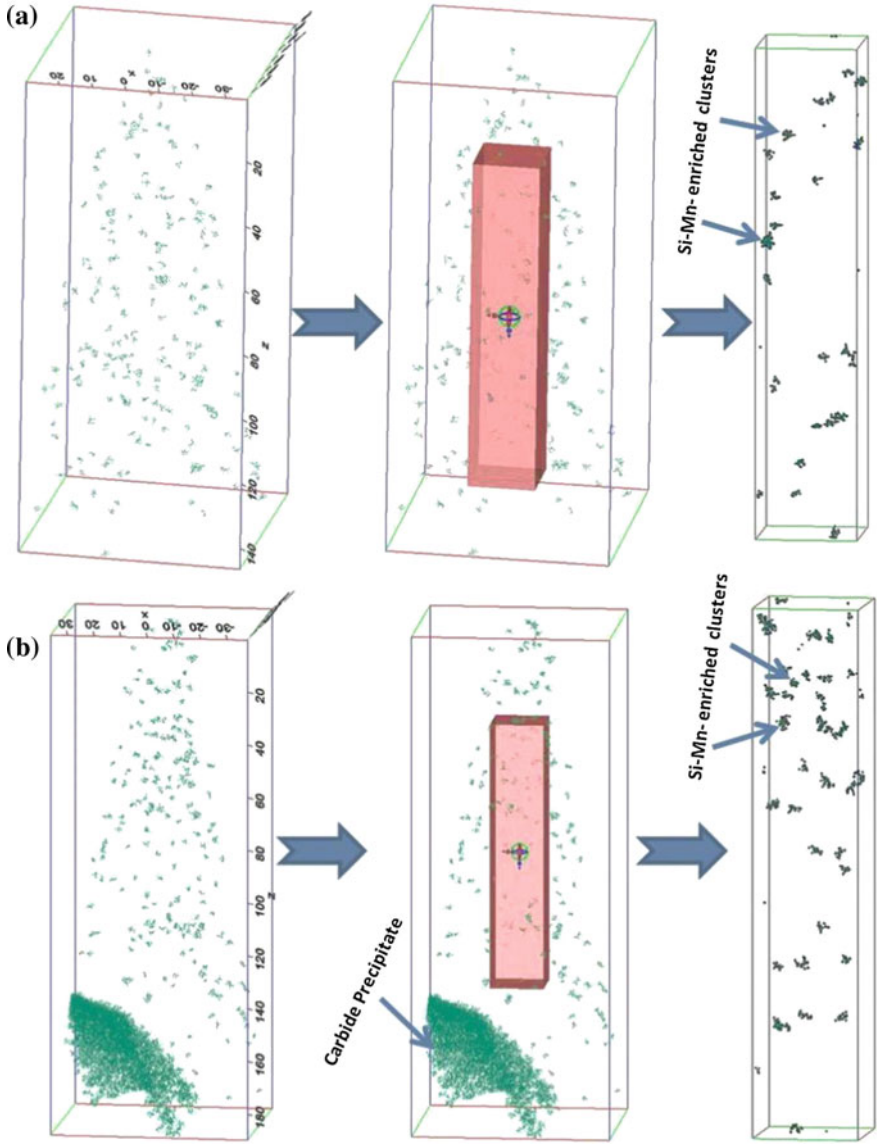

Fig. 3.32 Si–Mn-enriched cluster distribution postneutron irradiation for **a** CG and **b** UFG steels. The dimension of the interior (*colored*) boxes is 20 × 20 × 100 nm. The figure is reproduced from [221] with the permission from the publisher

during irradiation, changes in the structure and mechanical properties of nanocrystals under long-term irradiation.

Up to date, radiation resistance investigations of bulk nanostructured materials have been just started, but have already demonstrated promising results and

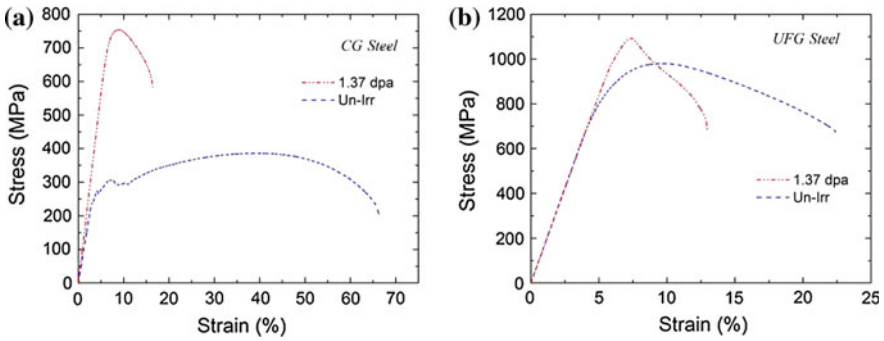

Fig. 3.33 Engineering stress–engineering strain curves for UFG **a** and CG **b** steel before and after irradiation to 1.37 dpa. The figure is reproduced from [221] with the permission from the publisher

important tendency in enhancing a radiation tolerance of metals by their nanostructuring. The origin and physical background of radiation-resistant behavior of bulk nanostructured materials is a primary task to be investigated for establishing a scientific fundament to improve essentially radiation-resistant properties of commercial alloys used in energy industry. The second task is manufacturing of pilot articles from SPD-processed commercial alloys (austenitic steels) and their tests under irradiation. The combination of high mechanical and radiation-resistant properties makes bulk nanostructured metallic materials to be of a high potential being applied to the future energy technologies.

3.3 Enhanced Chemical Properties

This section is about chemical properties of nanostructured metallic materials processed via SPD. We focus on two main functional properties, corrosion resistance and biocompatibility, which are important for applications.

3.3.1 Corrosion Resistance

Corrosion, the property of a material to deteriorate its properties due to interaction with the environment, especially chemically aggressive one, is an old problem for the industry since the very beginning. The embrittlement of a metal, leading to cracking of metallic materials inducing catastrophic failures of constructions, inspired the challenge to modify microstructures to survive hostile conditions. Materials required by different branches of industry are generally described by corresponding standards, but they are not flexible enough to reflect the industry needs. Development of corrosion-resistant metallic materials for advanced

applications is a topical task for modern materials science with attention to both effectiveness and security of the cutting-edge technologies and ecological security taking into consideration risks of global warming and industrial disasters. The problem of utmost importance is development of new functional materials with reasonable corrosion resistance to be used in new-generation applications.

Corrosion resistance was shown to be significantly enhanced in several nanocrystalline metals and alloys as compared to their coarse-grained counterparts. A tendency for localized corrosion was observed to be lower for electrodeposited (ED) nanocrystalline Ni [222]. The origin of better corrosion resistance for nanocrystalline metals was a subject of discussion and was attributed to increased breakdown potential and a better resistance to anodic dissolution as a result of lower porosity. Evidence provided to substantiate these hypotheses or cogent reasons for not observing a higher localized corrosion (such as pitting or intergranular attack) even in the presence of such a high volume fraction of grain boundaries has not been conclusive. The discovery of grain boundaries in ED nanocrystalline Ni to be predominantly coherent low-sigma coincidence site lattices (Σ3 CSLs) has been attributed to the possible origin of its superior corrosion resistance. Recently, it has been demonstrated [222] that grain refinement, independent of the processing route, leads to the formation of high-angle boundaries and provides corrosion resistance to down-hole alloys. This breakthrough and recent advances in processing technology to engineer high-strength corrosion-resistant metallic nanomaterials will enable the design of nanostructured metallic materials specifically for the oil and gas industry.

However, for the case of bulk nanostructured materials processed via SPD, it is necessary to note that up to now, there is no unified opinion on their corrosion properties. The fundamentals of the effect of grain size on corrosion behavior in different metallic materials were discussed in overview [223]. One can find in the literature a wide diversity in the data obtained on different nanostructured materials subjected to corrosion in different environments. In case of nanostructured CP Ti, it was shown that simultaneous enhancement of both mechanical strength and corrosion properties in aggressive environments, such as HCl and H_2SO_4 solutions, is possible [224–226]. Corrosion resistance of SPD-processed Ti is determined not only by grain size, but also by the crystallographic texture developed during SPD processing [226]. Particularly, basal planes of CP Ti offer higher corrosion resistance independently of grain size. Dislocation density can also significantly affect corrosion properties of this material. Very recently, it was demonstrated that corrosion resistance of the SPD-processed CP Ti can be further improved without any loss of mechanical strength via proper annealing treatments due to reduction of dislocation density and residual stresses (Fig. 3.34) [227]. Very similar results were reported for SPD-processed Mg alloy AZ61 tested in 0.1 M NaCl solution [228].

On the other hand, authors of [229] demonstrated that UFG samples of 321 (08Cr18Ni10) austenitic stainless steel exhibit less corrosion resistance than their coarse-grained counterparts in NaCl environment and higher stability in H_2SO_4 at room temperature, whereas in [230], an enhanced corrosion rate of UFG ferritic steel produced by SPD was observed in H_2SO_4 solution. Besides, the data published in [231] testify that SPD processing of interstitial-free steel does not lead to

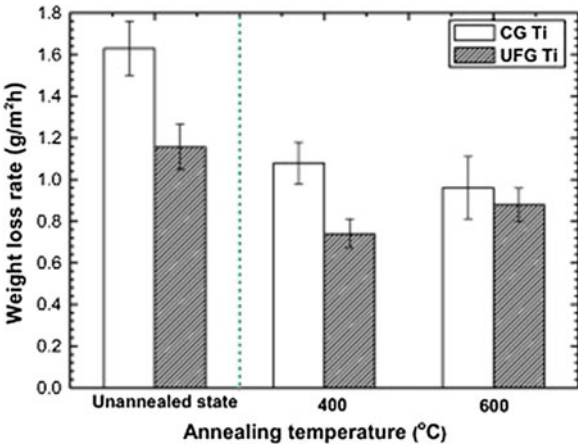

Fig. 3.34 The weight loss measurement test results of the coarse-grained Ti and SPD-processed Ti in a 0.5 M H_2SO_4 solution before and after annealing at different temperatures for 2 h. The figure is reproduced from [227] with the permission from the publisher

considerable change in corrosion properties in NaCl. It should be noted that crystallographic texture of steels can also affect their corrosion resistance. Particularly, it was shown that the pitting corrosion susceptibility of the grains of 316LVM stainless steel is dependent on the crystallographic planes [232]. The planar orientation {111} and {100} parallel to the surface had the highest resistance to pitting corrosion, and a lower pitting resistance was expected for the crystallographic planes with lower atomic density. So pitting susceptibility index (PSI) of the surface can be predicted based on texture measurements, and pitting resistance of steels can be improved by designing the desired crystallographic texture [232]. In [233], corrosion resistance of pure Mg in NaCl solution tended to degrade with increasing ECAP passes. Macroscopic preferential corrosion and grain boundary corrosion were observed in ECAPed pure Mg. The former resulted from the inhomogeneous strain distribution in the ECAPed samples, and the latter correlated with the stored energy around the deformed grain boundaries. Similar results, showing higher corrosion rate of ECAP processed pure AZ91 alloy than the as-cast state, were also reported in [234].

Grain refinement down to nanoscale can significantly affect the local corrosion behavior of metallic materials. In [235], nanostructured Al–Mn alloy subjected to immersion in 3.5 % NaCl artificial seawater for 168 h had fewer and finer pits compared to its coarse-grained counterpart due to the energy equilibration between non-equilibrium grain boundaries and intragranular defects as well as due to the finer Al_6Mn particles. Refinement of β-$Mg_{17}Al_{12}$ phase to nanoscale size via ECAP processing of the AZ61 Mg alloy decreased its susceptibility to microgalvanic corrosion [228]. An increased pit initiation resistance was reported also for Al–Mg alloys and AA5083 subjected to short-term corrosion testing [236], AA5052 [237],

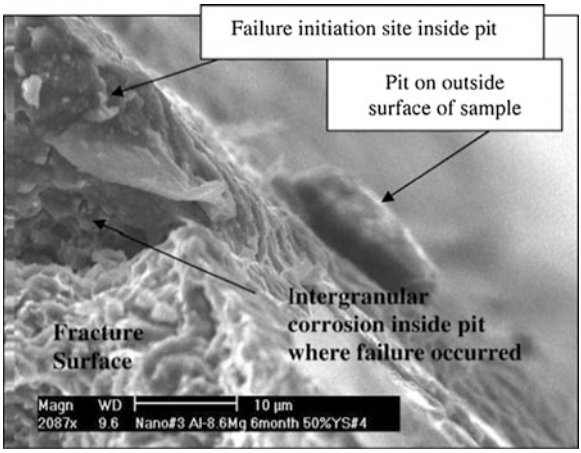

Fig. 3.35 SEM micrograph of the nanostructured Al–8.6 Mg after 6 months of alternate immersion in 3.5 % NaCl in the 50 % YS condition. Inside the pit intergranular corrosion is obvious. The image is reproduced from [236] with the permission from the publisher

AA6082 [238]. However, the long-term pit resistance of the nanostructured Al alloys shows an ambiguous character [236, 239]. The pitting depth in the nanostructured Al–Mg alloys was larger than that in the conventional material and also varied with varying Mg content [239]. This effect was related to susceptibility of the nanostructured Al alloys to intergranular corrosion (Fig. 3.35), whereas their coarse-grained counterparts are non-susceptible [236, 239].

Some nanostructured metallic materials attract significant interest of biomedical engineering (this is considered more in detail in Sects. 3.3.2 and 4.1). The biocorrosion response of nanostructured CP Ti processed by different ECAP routes was also studied in simulated body fluid [240, 241]. The nanostructured CP Ti produced by ECAP showed better corrosion resistance than the CG CP Ti in the Hank's solution due to the formation of highly stable oxide film on metal surface with higher grain boundary fraction. Crystallographic texture also significantly affected the corrosion response of the nanostructured material in the simulated body fluid. In [242], the ECAP and back pressure ECAP-processed AZ31 alloys (tested in the Hank's solution) exhibited corrosion rate similar to that of the as-extruded one, but the corrosion rate slightly increased after 1–2 passes ECAP or backpressure ECAP and further decreased after 4-pass procedure. One possible explanation could be attributed to the accumulative residual strains during deformation leading to more energy restored in the deformed grains and grain boundaries, which results in higher sensitivity of deformed grains and grain boundaries. Another explanation might be related to the gradual transformation of subgrain boundaries from low-angle type to high-angle ones after ECAP by absorbing dislocations generated during processing, and high-angle grain boundaries are more susceptible to chemical attack with higher grain boundary energies. Additionally, severe local corrosion was also observed for the 1–3 passes ECAP or back pressure

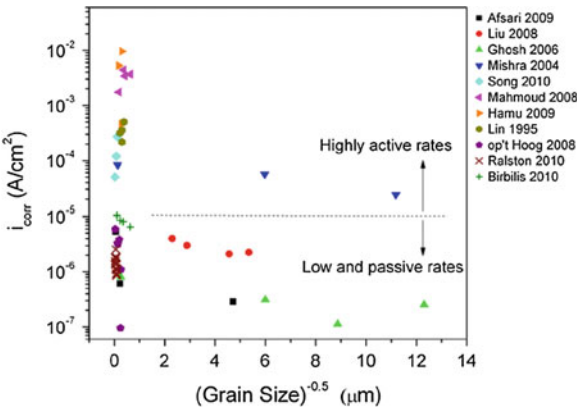

Fig. 3.36 The effect of grain size on corrosion rate (expressed as A cm^{-2}) for different materials and environments. The figure is reproduced from [243] with the permission from the publisher

ECAP-processed AZ31 alloy [242]. Compared to the as-extruded AZ31 alloy, the samples after ECAP or back pressure ECAP procedure showed much smaller sized corrosion pits on the surface after removing the corrosion product.

Generally, it can be outlined that nanostructured metallic materials show complex corrosion behavior depending on the environment. Careful analysis of all data available in the literature was performed in [243], and all the data in the literature were separated into two main classes (Fig. 3.36):

- range of material–environment combinations showing low-to-passive corrosion rates (≤10 μA cm^{-2}),
- range of material–environment combinations exhibiting highly active corrosion rates (≫10 μA cm^{-2}).

It was found that the data belonging to the first class tend to follow the Hall–Petch-type law where corrosion resistance can be presented as [243]

$$i_{\text{corr}} = (A) + (B)d^{-1/2} \tag{3.8}$$

where A is a function of the environment (as the same material with the same microstructure can have a different corrosion rate in different electrolytes) and B is a material constant determined by chemical composition of the material and its purity. This effect was experimentally observed on a wide range of metallic materials exhibiting some level of passivity (which have oxide on the metal surface). Figure 3.37 illustrates this effect for pure Mg, $Ni_{50.5}Ti_{49.5}$, Ni–Cu, and pure Al with different average grain sizes achieved using different processing routes (ECAP, cryorolling, drawing, etc.) [243–248]. This was related to the fact that grain refinement allows different rates of oxide growth on the surface. Since the oxide film conduction rate on surface is governed by grain boundary density, UFG and nanostructures are expected to be more corrosion resistant. In the absence of an oxide film on the surface (at dissolution rates of ≫10 μA cm^{-2}), UFG and nanostructures containing high grain boundary densities will enhance overall surface

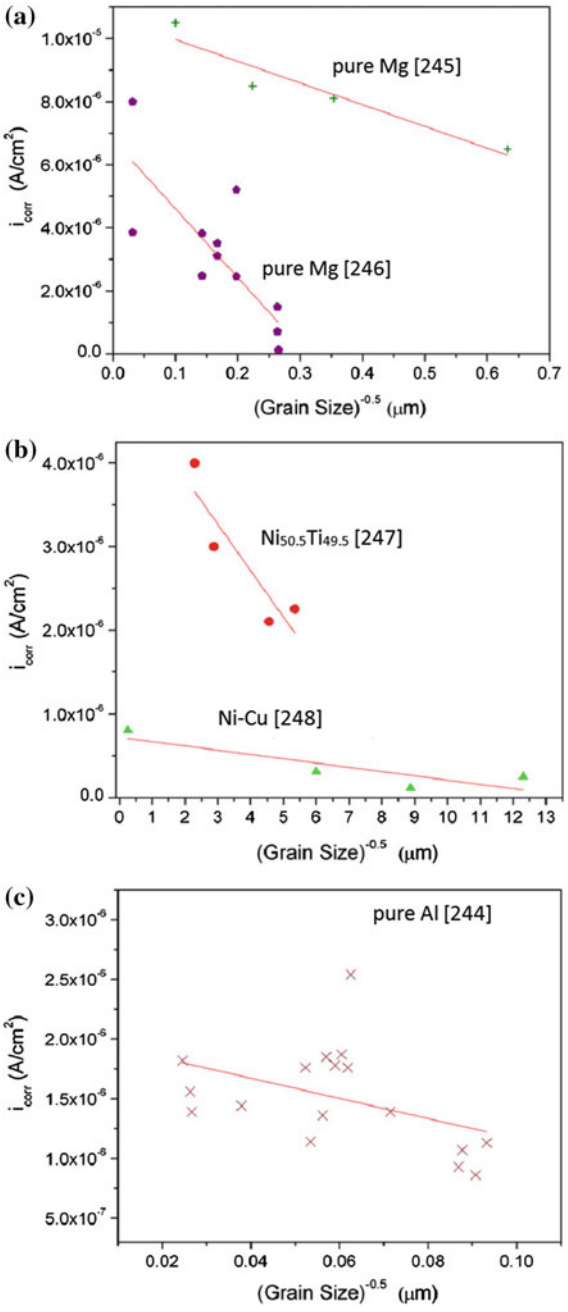

Fig. 3.37 The relationship between corrosion rate and grain size for low-to-passive current densities. The figure is reproduced from [243] with the permission from the publisher

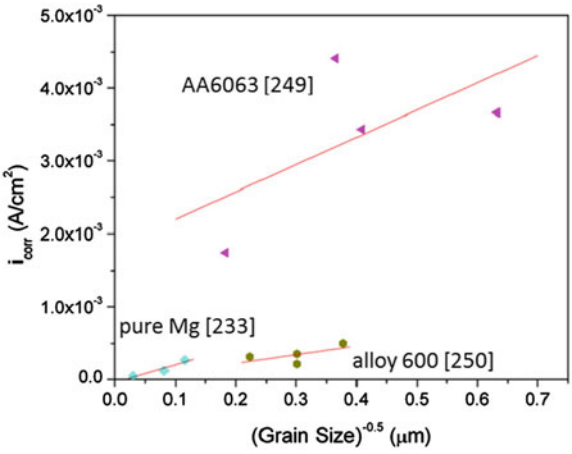

Fig. 3.38 The relationship between corrosion rate and grain size for high current densities in AA6063, pure Mg, and alloy 600. The figure is reproduced from [243] with the permission from the publisher

reactivity and, consequently, the corrosion rate as demonstrated for pure Mg, AA6063, and alloy 600 in Fig. 3.38.

This section clearly shows that there is no a general consensus in the literature as to the effect of nanostructuring on corrosion resistance. The reason for these controversial results is obviously connected with microstructural features of nanostructured metallic materials. Deformation processing imparts significant physical and chemical changes to the material in addition to the grain refinement that, in turn, considerably affects the demonstrated functional properties including corrosion behavior. Thus, systematic investigations of corrosion stability of SPD nanostructured materials and revealing its dependence on nanostructural parameters remain as one of the most challenging tasks in modern materials science.

3.3.2 Biocompatibility

For a long time, metallic biomaterials have been successfully used for fabrication of surgical implants due to their high strength combined with good formability, sufficient fatigue properties, and resistivity to fracture [251]. In addition to mechanical stability under physiological strains and stresses, the implant materials should be able to perform with an appropriate host response in a specific situation, i.e., to be biocompatible. This means that a material has to perform and not simply exist in the tissues, that the response which it evokes has to be appropriate for the application, and that the nature of the response to a specific material and its appropriateness may vary from one situation to another. The key to understand biocompatibility is the determination of which chemical, biochemical, physiological, physical, or other mechanisms become operative, (and why), under the highly specific conditions associated with contact between biomaterials and the tissues of the body and what are the consequences of these interactions [252]. Nowadays, just three metallic

systems Co–Cr-based alloys, Fe–Cr–Ni alloys (stainless steels), and pure Ti and Ti-based alloys have been used for implantation, since other systems do not possess required level of mechanical properties and/or biocompatibility [251]. The Co–Cr alloys are sought for medical applications because of their combination of corrosion resistance, wear resistance, and high strength. Increasing amounts of Cr added in solid solution to Co, up to 35 wt%, enhances corrosion resistance through the presence of a passive chromium oxide film. Stainless steels are the most widely used family of alloys for medical applications. They contain 17–21 wt% Cr which imparts good corrosion resistance due to the adherent chromium oxide film that forms and heals in the presence of oxygen. From the viewpoint of corrosion resistance, Ti is superior to other surgical metals due to the formation of a very stable passive layer of TiO_2 on its surface. Also, Ti has the low elastic modulus (twofold lower compared to Co–Cr alloys or stainless steels), which results in less stress shielding and associated bone resorption around Ti implants. Furthermore, Ti has the lower density and produces less artifacts on computer tomography and magnetic resonance imaging [253–255]. Pure Ti has low mechanical strength and fatigue endurance, so it has been alloyed by V and Al for improvement of mechanical properties. Currently, Ti–6Al–4V is the most widely used surgical Ti alloy.

Biocompatibility of biomaterial strongly depends on interrelated responses of both parts of the biomaterial–tissue complex and the interfacial processes. When placed in the tissues of the body, various reactions to a material may be seen over time. Within the host, one can envisage a sequence of events, potentially involving the interaction between proteins and other physiological macromolecules with the biomaterial surface, the initiation of inflammatory and/or immune responses, and then the repair and/or regeneration processes that may lead to stable equilibrium between material and host. The biomaterials are required to optimize the rate and quality of bone apposition to them, to minimize the rate of release of corrosion or degradation products and the tissue response to them, to minimize the rate of wear debris release and the tissue response to this debris, and to optimize the biomechanical environment in order to minimize disturbance to homeostasis in the bone and surrounding soft tissue [252].

In the last decade, there has been a breakthrough in studying the potential applications of bulk nanostructured metallic biomaterials in biomedical engineering, focusing on the effect of nanostructuring on cell/bacteria response. Few comprehensive review articles focused on this topic have been published very recently [251, 256, 257]. In 2004, Webster and Ejiofor [258] provided the first evidence of increased osteoblast adhesion on Ti, Ti–6Al–4V alloy and Co–Cr–Mo compacts with nanometer compared to conventionally sized particles. The increased cell adhesion was related to higher percentage of grain boundaries on the surface of nanomaterials considering that osteoblasts adhere specifically at grain boundaries. In two years, this group demonstrated that nanostructuring of these materials not only enhanced osteoblast adhesion, but also increased osteoblast metabolic activities leading to calcium deposition [259]. However, it should be noted that the studied compacts were not fully dense and had porosity of 5–10 %,

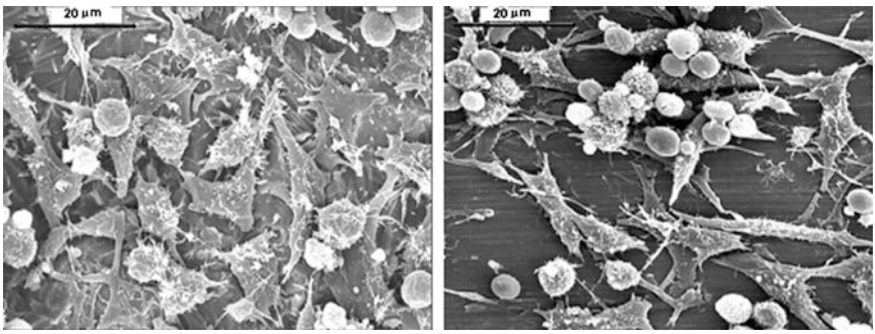

Fig. 3.39 Occupation of the mice fibroblast cells L929 after 24 h on the surface after hydrofluoric acid treatment of the nanostructured (*left*) and coarse-grained (*right*) CP Ti (Grade 4). The image is reproduced from [262] with the permission from the publisher

so, strictly speaking, the reported observations cannot be related only to the grain size effect. Later, research activities were more focused on fully dense bulk nanostructured metallic biomaterials produced via SPD processing [260–270], though nanostructuring of pure Ti via ECAP for application in medical implants was patented already in 2002 [271]. It was demonstrated that apart from ultrahigh strength (see Sect. 4.1), the nanostructured pure Ti has also increased bioreactivity. Preliminary cytocompatibility tests utilizing fibroblast mice cells L929 were carried out with hydrofluoric acid surface etching being performed prior to cell exposure [262]. The cell attachment investigation showed that fibroblast colonization of the CP Ti (Grade 4) surface increases after nanostructuring (Fig. 3.39). Further research focused on interactions of human bone marrow-derived mesenchymal stem cells (hMSCs) during the initial stages of cell attachment and spreading on the surface of nanostructured Ti [267]. The effect of nanostructuring was found to be quite striking: 40 min after seeding the biovolume of the hMSCs was up to 2.5 times greater on the ECAP-processed CP Ti than on the conventional coarse-grained material (Fig. 3.40; Table 3.6). Surface characterization by a range of techniques showed that the main factor responsible for the observed acceleration of hMSC attachment and spreading on CP Ti due to grain refinement in the bulk is the attendant changes in surface topography on the nanoscale [267]. Such acceleration of the initial attachment of hMSCs on Ti surfaces may prevent their apoptosis on the implant surface [272].

The nanostructured stainless steels also provide enhanced cell growth and proliferation [268, 270]. This was demonstrated on a 316L stainless steel processed using the phase reversion concept that allows to obtain grain size from nanograined to coarse-grained structure [270]. Grain refinement from 22 µm to 320 nm resulted in the increase of yield strength from 350 to 768 MPa without any significant reduction in ductility. The higher attachment on the substrate with the smallest grain size was visible within the first hour of culture (Fig. 3.41a), suggesting that the cell attachment to the surface was influenced by the grain structure of the steel substrate

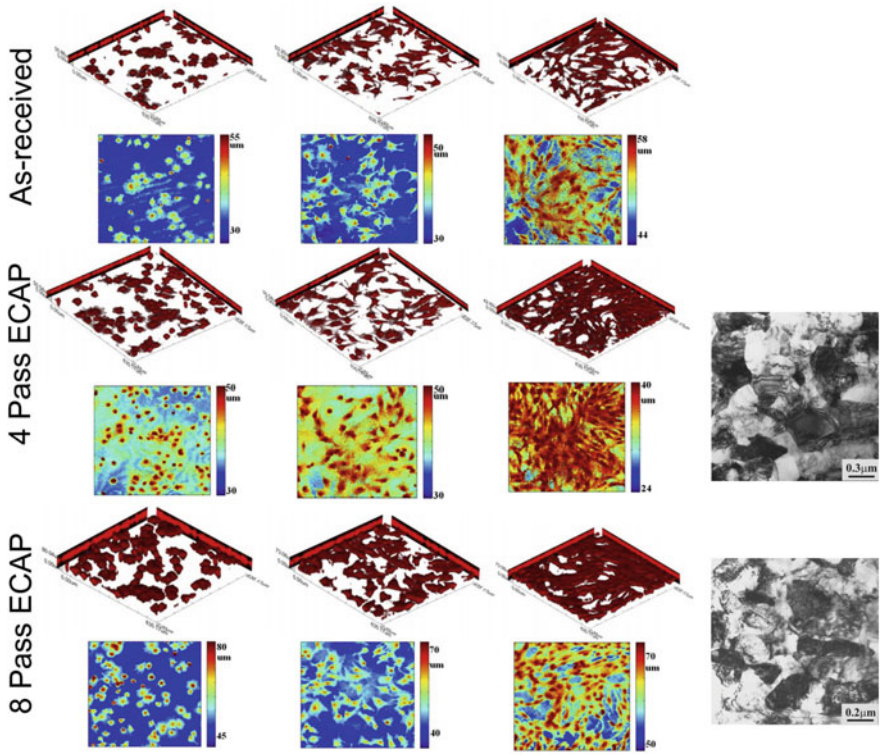

Fig. 3.40 Confocal scanning laser microscopy images of human bone marrow-derived mesenchymal stem cells on the surface of the as-received and ECAP-processed pure Ti (Grade 2) for different cultivation times (40 min, 2 h and 24 h) and corresponding TEM images of the ECAP-processed pure Ti. All images are reproduced from [267] with permission of the publisher

Table 3.6 Biovolume ($\mu m^3\ \mu m^{-2}$) of human bone marrow-derived mesenchymal stem cells on the surfaces of coarse-grained and nanostructured CP Ti (Grade 2)

Titanium, condition	Incubation time		
	40 min	2 h	24 h
Coarse grained	7.5 ± 0.2	22.0 ± 1.2	32.0 ± 5.2
ECAP 4 passes	15.2 ± 2.8	29.9 ± 2.3	37.1 ± 0.8
ECAP 8 passes	19.4 ± 5.3	38.0 ± 0.4	41.2 ± 0.7

The table is reproduced from [267] with the permission from the publisher

and was not a function of cell development or adaptation over time. With increasing time increases, the surface characteristics such as hydrophilicity started having a significant effect on cell attachment and proliferation. Similarly, cell metabolism measured by mitochondrial reduction of MTT was again higher for the nanograined steel and decreased with increasing grain size for tests conducted for 1 h to 7 days,

even though the cell density on all surfaces increased over time, indicating cytocompatibility of steels. Examination of individual proteins (fibronectin, actin, and vinculin) also indicated strong interplay between grain size and expression level of proteins. In a manner similar to cell attachment data, the fibronectin expression by preosteoblasts was greater on nanograined steel than on the coarse-grained substrate (Fig. 3.41b, c), as documented by a distinct network with stronger fluorescence intensity of immunostained fibronectin. The expression level of vinculin, a protein that forms focal contacts and actin stress fibers, after 48 h of culture, also showed a higher expression level at the edges and well-defined stress fibers on nanograined steel than on substrates with higher grain size (Fig. 3.41d). The expression level of vinculin from nanograins to coarse grains was lower, and actin was less prominent with increase in grain size (Fig. 3.41d, e). The very strong effect of grain size on osteoblast parameters (cell area, perimeter, Feret's diameter) is clearly demonstrated in Fig. 3.42.

No research on grain refinement in Co–Cr alloys with the aim to improve their biocompatibility can be found in the literature. Partly, it is related to the fact that superalloys are very hard to deform, so their nanostructuring in bulk via SPD processing cannot be performed. Ultrafine grain size can be achieved in Co–Cr alloys via their conventional forging using conditions that induce a novel mechanism of dynamic recrystallization, as described by Yamanaka et al. [273, 274]. It should be noted that conventional Co–Cr alloys have high mechanical strength, so surface nanostructuring can be envisaged as a strategy to improve biocompatibility of the material [275]. One technique of particularly high potential is surface mechanical attrition treatment (SMAT) [276–281]. SMAT induces large deformation in surfaces by recurring impact of hard spheres. Thus, induced surface deformation results in the formation of microstructures containing high densities of strengthening defects, including twins and the intersecting twin systems, dislocation walls, microbands, highly disoriented polygonal submicronic grains, and randomly oriented nanograins below the surface. The SMAT technique has been successfully applied to Co [276] and other difficult to deform metals, such as Ni_3Al [277], Fe_3Al [278], and Fe–30Ni [279]. The hierarchical textured surfaces obtained via SMAT on pure Ti and Ti–6Al–4V alloy showed enhanced cell attachment, spreading, viability, and alkaline phosphatase activity [280]. Biocompatibility improvement was also reported for CP Ti subjected to low-temperature plasma treatment that not only refined the surface grains to nanosize, but also altered the surface roughness and surface chemical composition [281].

There is now an increasing interest to use biodegradable metallic materials in various medical device applications, as discussed in the recent overviews [282, 283]. The biodegradable materials for implants and stents should satisfy a number of requirements toward medical materials, in particular high reliability, bioresorbability, and biodegradability (making the second surgery to remove an implant superfluous), required elastic modulus and strength, drug release option, etc. Nanostructured metals (Mg and Fe) and based on them porous composites have a great potential to satisfy all these requirements, with their biodegradability and bioresorbability (achieved by combining biodegradable magnesium and iron

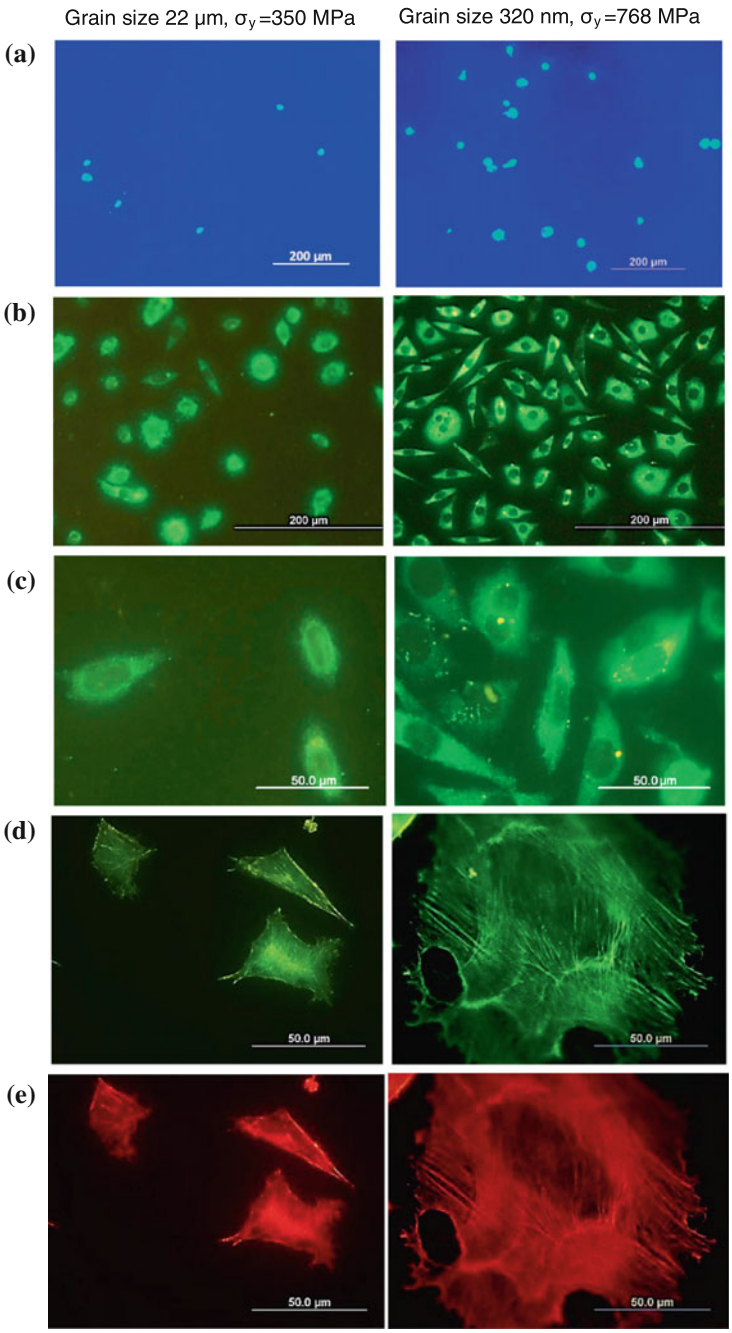

Fig. 3.41 Fluorescence micrographs illustrating the effect of grain size in the 316L stainless steel on **a** preosteoblast cell nuclei stained with Hoechst 33258 after 1-h culture; **b**, **c** immunocytochemistry of fibronectin expressed by preosteoblasts after incubation for 48 h; **d** the organization and assessment of vinculin focal contacts; and **e** actin stress fibers of preosteoblasts cultured for 48 h. The micrographs are reproduced from [270] with the permission from the publisher

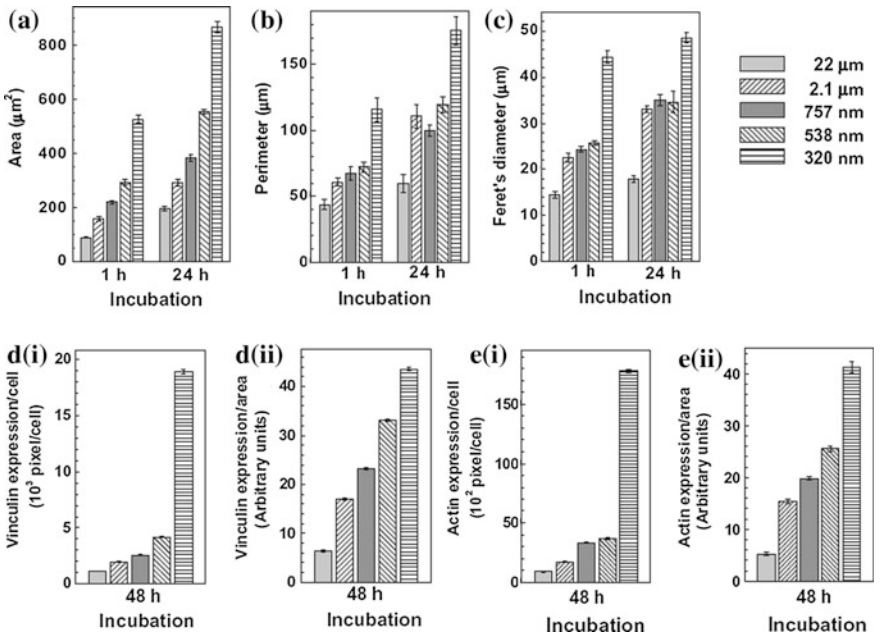

Fig. 3.42 Cytomorphometric evaluation of osteoblast parameters (cell area, perimeter, Feret's diameter). Data are mean ± SD ($n = 3$, $p < 0.05$), indicating a statistical difference from coarse-grained to nanograined 316L stainless steel with various grain sizes (22 μm, 2.1 μm, 757 nm, 538 nm, 320 nm). The figure is reproduced from [270] with the permission from the publisher

components), high strength (achieved by nanostructuring as well as iron reinforcement/skeleton in Mg), controlled corrosion behavior (by choosing the Mg/Fe distributions), required elastic modulus, enhanced possibility of bone adaptation, and controlled drug release option (achieved by macro- and microporosity) [283–287].

First studies of biocompatibility of SPD-processed Mg alloys [242, 288] show promising results of their increased potential as enhanced biodegradable materials encouraging further fast development of research in the field. Particularly, ECAP (also with backpressure) processing of the AZ31 Mg alloy has dramatically improved mechanical strength and reduced corrosion rate of the material without any degradation of its biocompatibility. The multipass ECAP (and also back pressure)-processed AZ31 alloy exhibited acceptable toxicity to MG63 cells with grade I toxicity (according to ISO 10993-5), which is comparable as other conventional Mg alloys, such as Mg–Ca [289] and Mg–Zn [290], showing good biocompatibility from the in vivo studies. However, 3-pass backpressure ECAP processed alloy indicated grade II toxicity, which may be attributed to the higher Mg and Al concentration leading to the osmolarity shock to the cells [242]. Thus, the optimum processing parameters should be carefully chosen for fabrication of

Mg alloys with set of required multifunctional properties for biomedical applications. Again, attention should be paid to the crystallographic texture developed during SPD processing, since the control of texture in Mg and Mg-based implants could be used to tailor the mechanical properties and the resorption rates without compromising cytocompatibility [291]. Surface modifications can be also utilized for further improvement of its biological properties [292, 293].

It is clearly seen that grain size and surface features of metallic biomaterials have significant effect on absorption of proteins that mediate cell adhesion and control and enhance subsequent cell functions and tissue growth. Relative increase in surface area and enhanced reactivity are the distinctive intrinsic aspects of nanostructured metallic biomaterials giving them the potential to manipulate their interaction with cells, and there are certain grain size thresholds that stimulate the mechanoreceptive responses in specific cells. Although there are numerous reports indicating that grain refinement can promote cell adhesion and subsequent activities, still more systematic studies are required to address the fundamental gaps in determining the mechanisms governing the specific cell response to nanograins. Most studies have focused on evaluating short-term response of cells to nanostructure, and supplementary in vivo studies are needed to validate their functionality in mediating the bone response.

References

1. Hall, E.O.: The deformation and ageing of mild steel: III discussion of results. Proc. Phys. Soc. B **64**, 747 (1951)
2. Petch, N.J.: The cleavage strength of polycrystals. J Iron Steel Inst. **174**, 25 (1953)
3. Valiev, R.Z.: Structure and mechanical properties of ultrafine grained metals. Mater. Sci. Eng. **59**, A234–A236 (1997)
4. Valiev, R.Z., Langdon, T.G.: Principles of equal-channel angular pressing as a processing tool for grain refinement. Prog. Mater Sci. **51**, 881 (2006)
5. Morris, D.G. In: Whang, S.H. (ed.) Nanostructured Metals and Alloys. Processing, Microstructure, Mechanical Properties and Applications, p. 297. Woodhead Publishing Limited, Cambridge (2011)
6. Zhu, Y.T., Han, B.Q., Lavernia, E.J.: In: Zehetbauer, M.J., Zhu, Y.T. (eds.) Bulk Nanostructured Materials, p. 89. WILEY-VCH Verlag GmbH & Co, Weinheim (2009)
7. Ovid'ko, I.A. In: Whang, S.H. (ed.) Nanostructured Metals and Alloys. Processing, Microstructure, Mechanical Properties and Applications, p. 430. Woodhead Publishing Limited, Cambridge (2011)
8. Zehetbauer, M.J., Estrin, Y.: In: Zehetbauer, M.J., Zhu, Y.T. (eds.) Bulk Nanostructured Materials, p. 109. WILEY-VCH Verlag GmbH & Co, Weinheim (2009)
9. Koch, C.C. In: Zehetbauer, M.J., Zhu Bulk, Y.T. (eds.) Nanostructured Materials, p. 3. WILEY-VCH Verlag GmbH & Co, Weinheim (2009)
10. Pande, C., Cooper, K.: Nanomechanics of Hall-Petch relationship in nanocrystalline materials. Prog. Mater Sci. **54**, 689 (2009)
11. Mayers, M.A., Mishra, A., Benson, D.J.: Mechanical properties of nanocrystalline materials. Prog. Mater Sci. **51**, 427 (2006)

12. Valiev, R.Z., Enikeev, N.A., Murashkin, M.Y., Kazykhanov, V.U., Sauvage, X.: On the origin of extremely high strength of ultrafine-grained Al alloys produced by severe plastic deformation. Scripta Mater. **63**, 949 (2010)
13. Valiev, R.Z., Enikeev, N.A., Murashkin, M.Y., Aleksandrov, S.E., Goldshtein, R.V.: Superstrength of ultrafine-grained aluminum alloys produced by severe plastic deformation. Doklady Phys. **55**(6), 267 (2010)
14. Valiev, R.Z., Langdon, T.G.: The art and science of tailoring materials by nanostructuring for advanced properties using SPD techniques. Adv. Eng. Mater. **12**, 677 (2010)
15. Valiev, R.Z., Enikeev, N.A., Langdon, T.G.: Towards superstrength of nanostructured metals and alloys produced by SPD. Kovove Mater. **49**, 1 (2011)
16. Krasilnikov, N., Lojkowski, W., Pakiela, Z., Valiev, R.Z.: Tensile strength and ductility of ultrafine-grained nickel processed by severe plastic deformation. Mater. Sci. Eng., A **37**, 330 (2005)
17. Thompson, A.W.: Yielding in nickel as a function of grain or cell size. Acta Metall. **23**, 1337 (1975)
18. Xiao, C., Mirshams, R.A., Whang, S.H., Yin, W.M.: Tensile behavior and fracture in nickel and carbon doped nanocrystalline nickel. Mater. Sci. Eng., A **301**, 35 (2001)
19. Ebrahimi, F., Bourne, G.R., Kelly, M.S., Matthews, T.E.: Mechanical properties of nanocrystalline nickel produced by electrodeposition. Nanostr. Mater. **11**, 343 (1999)
20. Hughes, D.A., Hansen, N.: Microstructure and strength of nickel at large strains. Acta Mater. **48**, 2985 (2000)
21. Tsuji, N.: In: Zhu, Y.T., Varyukhin, V. (eds.) Nanostructured Materials by High-Pressure Severe Plastic Deformation, p. 227. Springer, Netherlands (2006)
22. Furukawa, M., Horita, Z., Nemoto, M., Valiev, R.Z., Langdon, T.G.: Factors Influencing the flow and hardness of materials with ultrafine grain sizes. Phil. Mag. A **78**, 203 (1998)
23. Valiev, R.Z., Ivanisenko, Y.V., Rauch, E.F., Baudelet, B.: Structure and deformation behaviour of Armco iron subjected to severe plastic deformation. Acta Mater. **44**, 4705 (1996)
24. Jones, R.L., Conrad, H.: The effect of grain size on the strength of alpha titanium. Trans. Met. Soc. AIME **245**, 779 (1969)
25. Charit, I., Murty, K.L.: Effect of radiation exposure on the Hall-Petch relation and its significance of radiation embrittlement in iron and ferritic steels. Trans. SMiRT **19**, 1–6 (2007)
26. Malow, T.R., Koch, C.C.: Mechanical properties, ductility, and grain size of nanocrystalline iron produced by mechanical attrition. Metall. Mater. Trans. A **29**, 2285 (1998)
27. Sergueeva, A.V., Stolyarov, V.V., Valiev, R.Z., Mukherjee, A.K.: Superplastic behavior of ultrafine-grained Ti-6Al-4V alloys. Mater. Sci. Eng., A **323**, 318 (2002)
28. Semenova, I.P., Salimgareeva, G., Da Costa, G., Lefebvre, W., Valiev, R.Z.: Enhanced strength and ductility of ultrafine-grained Ti processed by severe plastic deformation. Adv. Eng. Mater. **12**, 803 (2010)
29. Ivanisenko, Y., Sergueeva, A.V., Minkow, A., Valiev, R.Z., Fecht, H.J. In: Zehetbauer, M.J., Valiev, R.Z. (eds.) Nanomaterials by Severe Plastic Deformation, p. 453. Wiley-VCH, Weinheim (2004)
30. Chukin, M.V., Koptseva, N.V., Valiev, R.Z., Yakovleva, I.L., Zrnik, J., Covarik, T.: The diffraction submicroscopic analysis of the submicrocrystal and nanocrystal structure of constructional carbon steels after equal channel angle pressing and further deformation. Vestnik MGTU **1**, 31 (2008)
31. Sabirov, I., Murashkin, MYu., Valiev, R.Z.: Nanostructured aluminium alloys produced by severe plastic deformation: new horizons in development. Mater. Sci. Eng. A. **560**, 1–24 (2013)
32. Li, J.S.M.: In: Li, J.S.M. (ed.) Mechanical Properties of Nanocrystalline Materials, p. 193. Pan Stanford Publ, Singapore (2011)
33. Firstov, S.A., Rogul, T.G., Marushko, V.T., Sagaydak, V.A.: Structure and microhardness of polycrystalline chromium produced by magnetron sputtering. Issues Mater. Sci. **33**, 201 (2003)

34. Firstov, S.A., Rogul, T.G., Shut, O.A.: Transition from microstructures to nanostructures and ultimate hardening. Funct. Mater. **16**, 4 (2009)
35. Valiev, R.Z., Kozlov, E.V., Ivanov, YuF, Lian, J., Nazarov, A.A., Baudelet, B.: Deformation behaviour of ultra-fine-grained copper. Acta Metall. Mater. **42**, 2467 (1994)
36. Liddicoat, P.V., Liao, X.Z., Zhao, Y., Zhu, Y.T., Murashkin, M.Y., Lavernia, E.J., Valiev, R.Z., Ringer, S.P.: Nanostructural hierarchy increases the strength of aluminium alloys. Nature Comm. **1**, 63 (2010)
37. Valiev, R.Z., Murashkin, M.Y., Bobruk, E.V., Raab, G.I.: Grain refinement and mechanical behavior of the Al alloy subjected to the new SPD technique. Mater. Trans. **50**, 87 (2009)
38. Abramova, M.M., Enikeev, N.A., Valiev, R.Z., Etienne, A., Radiguet, B., Ivanisenko, Y., Sauvage, X.: Grain boundary segregation induced strengthening of an ultrafine-grained austenitic stainless steel. Mater. Lett. **136**, 349–352 (2014)
39. Scheriau, S., Zhang, Z., Kleber, S., Pippan, R.: Deformation mechanisms of a modified 316L austenitic steel subjected to high pressure torsion. Mater. Sci. Eng., A **528**, 2776–2786 (2011)
40. Krawczynska, A.T., Lewandowska, M., Pippan, R., Kurzydlowski, K.J.: The effect of high pressure torsion on structural refinement and mechanical properties of an austenitic stainless steel. J. Nanosci. Nanotech. **13**, 1–4 (2013)
41. Wang, H., Shuro, I., Umemoto, M., Kuo, H.H., Todaka, Y.: Annealing behavior of nano-crystalline austenitic SUS316L produced by HPT. Mater. Sci. Eng., A **556**, 906–910 (2012)
42. Valiev, R.Z., Zhilyaev, A.P., Langdon, T.G.: Bulk Nanostructured Materials: Fundamentals and Applications, 456 p. Wiley-TMS, New York (2013)
43. Raabe, D., Herbig, M., Sandlöbes, S., Li, Y., Tytko, D., Kuzmina, M., Ponge, D., Choi, P.P.: Grain boundary segregation engineering in metallic alloys: a pathway to the design of interfaces. Curr. Opin. Solid State Mater. Sci. **18**, 253–261 (2014)
44. Raabe, D., Choi, P.P., Li, Y., Kostka, A., Sauvage, X., Lecouturier, F., Hono, K., Kirchheim, R., Pippan, R., Embury, D.: Metallic composites processed via extreme deformation: toward the limits of strength in bulk materials. MRS Bull. **35**, 982 (2010)
45. Morris, D.G. (ed.): Mechanical Behaviour of Nanostructured Materials. Trans. Tech. Publications, Uetikon-Zurich (1998)
46. Koch, C.C.: Optimization of strength and ductility in nanocrystalline and ultrafine grained metals. Scripta Mater. **49**, 657 (2003)
47. Horita, Z., Fujinami, T., Nemoto, M., Langdon, T.G.: Equal-channel angular pressing of commercial aluminum alloys: grain refinement, thermal stability and tensile properties. Metall. Mater. Trans. **31A**, 691 (2000)
48. Zhu, Y.T., Langdon, T.G.: The fundamentals of nanostructured materials processed by severe plastic deformation. JOM **56**(10), 58 (2004)
49. Zhao, Y., Zhu, Y.T., Lavernia, E.J.: Strategies for improving tensile ductility of bulk nanostructured materials. Adv. Eng. Mater. **12**, 76 (2010)
50. Ma, E.: Eight routes to improve the tensile ductility of bulk nanostructured metals and alloys. JOM **58**(4), 49 (2006)
51. Dieter, G.E.: Mechanical Metallurgy. McGraw-Hill, Boston (1986)
52. Hart, E.W.: Theory of the tensile test. Acta Metal. Mater. **15**, 351 (1967)
53. Valiev, R.Z.: Nanostructuring of metals by severe plastic deformation for advanced properties. Nat. Mater. **3**, 511–516 (2004)
54. Valiev, R.Z., Alexandrov, I.V., Lowe, T.C., Zhu, Y.T.: Paradox of strength and ductility in metals processed by severe plastic deformation. J. Mater. Res. **17**, 5 (2002)
55. Horita, Z., Ohashi, K., Fujita, T., Kaneko, K., Langdon, T.G.: Achieving high strength and high ductility in precipitation-hardened alloys. Adv. Mater. **17**, 1599 (2005)
56. Wang, Y., Chen, M., Zhou, F., Ma, E.: High tensile ductility in a nanostructured metal. Nature **419**, 912 (2002)
57. Valiev, R.Z., Sergueeva, A.V., Mukherjee, A.K.: The effect of annealing on tensile deformation behavior of nanostructured SPD titanium. Scripta Mater. **49**, 669 (2003)

58. Parker, E.R.: Materials Data Book for Engineers and Scientists. McGraw-Hill, New York (1967)
59. Brandes, E.A., Brook, G.B. In: Smithells Metals Reference Book, 7th edn, Chap. 22. Butterworth–Heinemann, Oxford (1992)
60. Hoeppel, H.W., May, J., Eisenlohr, P., Goeken, M.: Strain-rate sensitivity of ultrafine-grained materials. Z. Metallkd. **96**, 566 (2005)
61. May, J., Hoeppel, H.W., Goeken, M.: Strain rate sensitivity of ultrafine-grained aluminium processed by severe plastic deformation. Scripta Mater. **53**, 189 (2005)
62. Dalla Torre, F., Lapovok, R., Sandlin, J., Thomson, P.F., Davies, C.H.J., Pereloma, E.V.: Microstructures and properties of copper processed by equal channel angular extrusion for 1–16 passes. Acta Mater. **52**, 4819 (2004)
63. Zhang, X., Wang, H., Scattergood, R.O., Narayan, J., Koch, C.C., Sergueeva, A.V., Mukherjee, A.K.: Studies of deformation mechanisms in ultra-fine-grained and nanostructured Zn. Acta Mater. **50**, 4823 (2002)
64. Mughrabi, H., Hoeppel, H.W., Kautz, M., Valiev, R.Z.: Annealing treatments to enhance thermal and mechanical stability of ultrafine-grained metals produced by severe plastic deformation. Z. Metallkd. **94**, 1079 (2003)
65. Park, Y.S., Chung, K.H., Kim, N.J., Lavernia, E.J.: Microstructural investigation of nanocrystalline bulk Al–Mg alloy fabricated by cryomilling and extrusion. Mater. Sci. Eng., A **374**, 211 (2004)
66. Zhao, Y.H., Zhu, Y., Lavernia, E.J.: Strategies for improving tensile ductility of bulk nanostructured materials. Adv. Eng. Mater. **12**, 769–778 (2010)
67. Ebrahimi, F., Bourne, G.R., Kelly, M.S., Matthews, T.E.: Mechanical properties of nanocrystalline nickel produced by electrodeposition. Scripta Mater. **11**, 343 (1999)
68. Zhao, Y.H., Liao, X.Z., Cheng, S., Ma, E., Zhu, Y.T.: Simultaneously increasing the ductility and strength of nanostructured alloys. Adv. Mater. **18**, 2280 (2006)
69. Cheng, S., Zhao, Y.H., Zhu, Y.T., Ma, E.: Optimizing the strength and ductility of fine structured 2024 Al alloy by nano-precipitation. Acta Mater. **55**, 5822 (2007)
70. Lu, L., Shen, Y.F., Chen, X.H., Qian, L.H., Lu, K.: Ultrahigh strength and high electrical conductivity in copper. Science **304**, 422 (2004)
71. Zhao, Y.H., Bingert, J.F., Liao, X.Z., Cui, B.Z., Han, K., Sergueeva, A.V., Mukherjee, A.K., Valiev, R.Z., Langdon, T.G., Zhu, Y.T.: Simultaneously increasing the ductility and strength of ultra-fine-grained pure copper. Adv. Mater. **18**, 2949 (2006)
72. Tao, N., Lu, K.: Dynamic plastic deformation (DPD): a novel technique for synthesizing bulk nanostructured metals. J. Mater. Sci. Tech. **23**(6), 771 (2007)
73. Ungar, T., Balogh, L., Zhao, Y.H., Zhu, Y.T., Horita, Z., Xu, C., Langdon, T.G.: Acta Mater. **56**, 809 (2008)
74. Son, Y.I., Lee, Y.K., Park, K.T., Lee, C.S., Shin, D.H.: Ultrafine grained ferrite-martensite dual phase steels fabricated via equal channel angular pressing: microstructure and tensile properties. Acta Mater. **53**, 3125 (2005)
75. Wang, Y., Ma, E., Valiev, R.Z., Zhu, Y.: Tough nanostructured metals at cryogenic temperatures. Adv. Mater. **16**, 328 (2004)
76. Li, Y.I., Zeng, X.H., Blum, W.: Transition from strengthening to softening by grain boundaries in ultrafine-grained Cu. Acta Mater. **52**, 5009 (2004)
77. Valiev, R.Z., Murashkin, MYu., Kilmametov, A.R., Straumal, B.B., Chinh, N.Q., Langdon, T.G.: Unusual super-ductility at room temperature in an ultrafine-grained aluminum alloy. J. Mater. Sci. **45**, 4718 (2010)
78. Moreno-Valle, E.C., Monclus, M.A., Molina-Aldareguia, J.M., Enikeev, N., Sabirov, I.: Biaxial deformation behavior and enhanced formability of ultrafine-grained pure copper. Metall. Mater. Trans. A **44**, 2013–2399 (2013)
79. Suresh, S.: Fatigue of Materials, p. 679. Cambridge University Press, Cambridge (1998)
80. Hoeppel, H.W., Goeken, M.: Fatigue behavior in nanostructured metals. In: Whang, S.H. (ed.) Nanostructured Metals and Alloys: Processing, Microstructure, Mechanical Properties and Applications, p. 507. Woodhead Publishing Limited (2011)

81. Estrin, Y., Vinogradov, A.: Fatigue behavior of light alloys with ultra-fine grain structure produced by severe plastic deformation: an overview. Int. J. Fatigue **32**, 898–907 (2010)
82. Hoeppel, H.W., Kautz, M., Xu, C., Murashkin, M., Langdon, T.G., Valiev, R.Z., Mughrabi, H.: An overview: fatigue behavior of ultra-fine grained metals and alloys. Int. J. Fatigue **28**, 1001–1010 (2006)
83. Mughrabi, H., Hoeppel, H.W., Kautz, M.: Fatigue and microstructure of ultra-fine grained metals produced by severe plastic deformation. Scripta Mater. **51**, 807–812 (2004)
84. Murashkin, M., Sabirov, I., Prosvirnin, D., Ovid'ko, I., Terentiev, V., Valiev, R., Dobatkin, S.: Fatigue behavior of an ultra-fine grained Al-Mg-Si alloy processed by high-pressure torsion. Metals **5**, 578 (2015)
85. De, P.S., Mishra, R.S., Smith, C.B.: Effect of microstructure on fatigue life and fracture morphology in an aluminum alloy. Scripta Mater. **60**, 500–503 (2009)
86. Vinogradov, A., Hashimoto, S., Kopylov, V.I.: Enhanced strength and fatigue life of ultra-fine grain Fe-36Ni Invar alloy. Mater. Sci. Eng., A **355**, 277 (2003)
87. Vinogradov, A., Hashimoto, S.: Multiscale phenomena in fatigue of ultra-fine grain materials —an overview. Mater. Trans. **42**, 74–84 (2001)
88. Gale, F.W., Totemeier, T.C. (eds.) Smithells Reference Book. Elsevier, Amsterdam (2004)
89. Patlan, V., Vinogradov, A., Higashi, K., Kitagawa, K.: Overview of fatigue properties of fine grain 5056 Al-Mg alloy processed by equal-channel angular pressing. Mater. Sci. Eng., A **300**, 171 (2001)
90. Cavaliere, P., Cabibbo, M.: Effect of Sc and Zr additions on the microstructure and fatigue properties of AA6106 produced by equal-channel-angular-pressing. Mater. Charact. **59**, 197 (2008)
91. Stolyarov, V.V., Latysh, V.V., Valiev, R.Z., Zhu, Y.T. In Lowe, T.C., Valiev, R.Z. (eds.) Investigations and Applications of Severe Plastic Deformation, p. 367. Kluwer Publishers, Dordrecht (2000)
92. Vinogradov, AYu., Stolyarov, V.V., Hashimoto, S., Valiev, R.Z.: Cyclic behavior of ultrafine-grain titanium produced by severe plastic deformation. Mater. Sci. Eng., A **318**, 163–173 (2001)
93. Kim, W.J., Hyun, C.Y., Kim, H.K.: Fatigue strength of ultrafine-grained pure Ti after severe plastic deformation. Scripta Mater. **54**, 1745–1750 (2006)
94. Vinogradov, A., Hashimoto, S.: Fatigue of severely deformed metals. Adv. Eng. Mater. **5**, 351 (2003)
95. Saitova, L.R., Höppel, H.W., Göken, M., Semenova, I.P., Valiev, R.Z.: Cyclic deformation behavior and fatigue lives of ultrafine-grained Ti-6AL-4V ELI alloy for medical use. Int. J. Fatigue **31**, 322–331 (2009)
96. Chapetti, M.D., Miyata, H., Tagawa, T., Miyata, T., Fujioka, M.: Fatigue strength of ultra-fine grained steels. Mater. Sci. Eng., A **381**, 331–336 (2004)
97. Vinogradov, A., Washikita, A., Kitagawa, K., Kopylov, V.I.: Fatigue life of fine-grain Al–Mg–Sc alloys produced by equal-channel angular pressing. Mater. Sci. Eng., A **349**, 318–326 (2003)
98. Chung, C.S., Kim, J.K., Kim, H.K., Kim, W.J.: Improvement of high-cycle fatigue life in a 6061 Al alloy produced by equal channel angular pressing. Mater. Sci. Eng., A **337**, 39–44 (2002)
99. May, J., Dinkel, M., Amberger, D., Hoeppel, H.W., Goeken, M.: Mechanical properties, dislocation density and grain structure of ultrafine—grained aluminum and aluminum—magnesium alloys. Metall. Mater. Trans. A **38**, 1941–1945 (2007)
100. Avtokratova, E.V., Kaibyshev, R.O., Sitdikov, OSh: Fatigue of a fine-grained high-strength Al-6Mg-Sc alloy produced by equal-channel angular pressing. Phys. Met. Metall. **105**, 532 (2008)
101. Semenova, I.P., Salimgareeva, G.K., Latysh, V.V., Lowe, T.C., Valiev, R.Z.: Enhanced fatigue strength of commercially pure Ti processed by severe plastic deformation. Mater. Sci. Eng., A **503**, 92–95 (2009)

102. Lukas, P., Kunz, L., Svoboda, M. In: Proceedings of 9th International Fatigue Conference, 2006, FT62
103. Hoeppel, H.W., May, J., Prell, M., Goeken, M.: Influence of grain size and precipitation state on the fatigue lives and deformation mechanisms of CP aluminium and AA6082 in the VHCF-regime. Int. J. Fatigue **33**, 10–18 (2011)
104. Malekjani, S., Hodgson, P.D., Cizek, P., Hilditch, T.B.: Cyclic deformation response of ultrafine pure Al. Acta Mater. **59**, 5358–5367 (2011)
105. Canadinc, D., Maier, H.J., Gabor, P., May, J.: On the cyclic deformation response of ultrafine-grained Al–Mg alloys at elevated temperatures. Mater. Sci. Eng., A **496**, 114–120 (2008)
106. Mughrabi, H., Hoeppel, H.W.: Cyclic deformation and fatigue properties of ultrafine grain size materials: current status and some criteria for improvement of the fatigue resistance. Mater. Res. Soc. Symp. Proc. **B2.1.1**, 634 (2001)
107. Malekjani, S., Hodgson, P.D., Cizek, P., Sabirov, I., Hilditch, T.B.: Cyclic deformation response of UFG 2024 Al alloy. Int. J. Fatigue **33**, 700–709 (2011)
108. Huebner, P., Kiessling, R., Biermann, H., Vinogradov, A.: Fracture behaviour of ultrafine-grained materials under static and cyclic loading. Int. J. Mater. Res. **97**, 1566–1570 (2006)
109. Huebner, P., Kiessling, R., Biermann, H., Hinkel, T., Jungnickel, W., Kawalla, R., Hoeppel, H.W., May, J.: Static and cyclic crack growth behavior of ultrafine-grained Al produced by different severe plastic deformation methods. Metall. Mater. Trans. A **38**, 1926–1933 (2007)
110. Vinogradov, A., Nagasaki, S., Patlan, V., Kitagawa, K., Kawazoe, N.: Fatigue properties of 5056 Al-Mg alloy produced by equal-channel angular pressing. Nanostr. Mater. **11**, 925–934 (1999)
111. Wu, L., Stoica, G.M., Liao, H.H., Agnew, S.R., Payzant, E.A., Wang, G., Fielden, D.E., Chen, L., Liaw, P.K.: Fatigue-property enhancement of magnesium alloy AZ31B through ECAP. Metall. Mater. Trans. A **38**, 2283–2289 (2007)
112. Hanlon, T., Tabachnikova, E.D., Suresh, S.: Fatigue behavior of nanocrystalline metals and alloys. Int. J. Fatigue **27**, 1147–1158 (2005)
113. Kim, H., Lee, Y., Chung, C.: Fatigue properties of a fine-grained magnesium alloy produced by equal channel angular pressing. Scripta Mater. **52**, 473–477 (2005)
114. Lapovok, R., Loader, C., Dalla Torre, F.H., Semiatin, S.L.: Microstructure evolution and fatigue behavior of 2124 aluminum processed by ECAE with back pressure. Mater. Sci. Eng., A **425**, 36–46 (2006)
115. Malekjani, S., Hodgson, P.D., Stanford, N.E., Hilditch, T.B.: The role of shear banding on the fatigue ductility of ultrafine-grained aluminium. Scripta Mater. **68**, 269–272 (2013)
116. Malekjani, S., Hodgson, P.D., Stanford, N.E., Hilditch, T.B.: Shear bands evolution in ultrafine-grained aluminium under cyclic loading. Scripta Mater. **68**, 821–824 (2013)
117. Zum Gahr, K.H.: Microstructure and Wear of Materials. Elsevier, Amsterdam (1987)
118. Diomidis, N., Mischler, S., More, N.S., Roy, M.: Tribo-electrochemical characterization of metallic biomaterials for total joint replacement. Acta Biomater. **8**, 852–859 (2012)
119. Wang, C.T., Gao, N., Wood, R.J.K., Langdon, T.G.: Wear behavior of an aluminum alloy processed by equal-channel angular pressing. J. Mater. Sci. **46**, 123–130 (2011)
120. Jafari, M., Enayati, M.H., Abbasi, M.H., Karimzadeh, F.: Compressive and wear behavior of bulk nanostructured Al2024 alloy. Mater. Design. **31**, 663–669 (2010)
121. Ortiz-Cuellar, E., Hernandez-Rodriguez, M.A.L., García-Sanchez, E.: Evaluation of the tribological properties of an Al–Mg–Si alloy processed by severe plastic deformation. Wear **271**, 1828–1832 (2011)
122. Purcek, G., Saray, O., Kucukomeroglu, T., Haouaoui, M., Karaman, I.: Effect of equal-channel angular extrusion on the mechanical and tribological properties of as-cast Zn–40Al–2Cu–2Si alloy. Mater. Sci. Eng., A **527**, 3480 (2010)
123. Purcek, G., Karaman, I., Yapici, G.G., Al-Maharbi, M., Kuçukomeroglu, T., Saray, O.: Enhancement in mechanical behavior and wear resistance of severe plastically deformed two-phase Zn–Al alloys. Int. J. Mater. Res. **98**, 332–338 (2007)

124. Edalati, K., Ashida, M., Horita, Z., Matsui, T., Kato, H.: Wear resistance and tribological features of pure aluminum and Al–Al_2O_3 composites consolidated by high-pressure torsion. Wear **310**, 83–89 (2014)
125. Purcek, G., Saray, O., Kul, O., Karaman, I., Yapici, G.G., Haouaoui, M., Maier, H.J.: Mechanical and wear properties of ultrafine-grained pure Ti produced by multi-pass equal-channel angular extrusion. Mater. Sci. Eng., A **517**, 97 (2009)
126. Ming, Q., Yong-zhen, Z., Jian-heng, Y., Jun, Z.: Microstructure and tribological characteristics of Ti–6Al–4V alloy against GCr15 under high speed and dry sliding. Mater. Sci. Eng., A **434**, 71–75 (2006)
127. Sato, H., Elhadad, S., Sitdikov, O., Watanabe, Y.: Effects of processing routes on wear property of Al-Al3Ti alloys severely deformed by ECAP. Mater. Sci. Forum **971**, 584–586 (2008)
128. Kim, Y.S., Ha, J.S., Kim, W.J.: Characteristics of severely deformed 6061 Al and AZ61 Mg alloys. Mater. Sci. Forum **597**, 449–452 (2004)
129. Kucukomeroglu, T.: Effect of equal-channel angular extrusion on mechanical and wear properties of eutectic Al–12Si alloy. Mater. Design. **31**, 782 (2010)
130. Kim, Y.S., Yu, H.S., Shin, D.H.: Low sliding-wear resistance of ultrafine-grained Al alloys and steel having undergone severe plastic deformation. Int. J. Mater. Res. **100**, 871 (2009)
131. Kazemi Talachi, A., Eizadjou, M., Danesh Manesh, H., Janghorban, K.: Wear characteristics of severely deformed aluminum sheets by accumulative roll bonding (ARB) process. Mater. Charact. **62**, 12–21 (2011)
132. Abd El Aal, M.I., El Mahallawy, N., Shehata, F.A., Abd El Hameed, M., Yoon, E.Y., Kim, H.S.: Wear properties of ECAP-processed ultrafine grained Al–Cu alloys. Mater. Sci. Eng., A **527**, 3726–3732 (2010)
133. Gao, L.L., Cheng, X.H.: Effect of ECAE on microstructure and tribological properties of Cu-10 %Al-4 %Fe Alloy. Tribol. Lett. **27**, 221 (2007)
134. Gao, L.L., Cheng, X.H.: Microstructure and dry sliding wear behavior of Cu–10 %Al–4 %Fe alloy produced by equal channel angular extrusion. Wear **265**, 986 (2008)
135. Gao, L.L., Cheng, X.H.: Microstructure, phase transformation and wear behavior of Cu–10 %Al–4 %Fe alloy processed by ECAE. Mater. Sci. Eng., A **473**, 259 (2008)
136. Wang, Z.B., Tao, N.R., Li, S., Wang, W., Liu, G., Lu, J., Lu, K.: Effect of surface nanocrystallization on friction and wear properties in low carbon steel. Mater. Sci. Eng., A **352**, 144 (2003)
137. Stolyarov, V.V., Shuster, L.S., Migranov, M.S., Valiev, R.Z., Zhu, Y.T.: Reduction of friction coefficient of ultrafine-grained CP titanium. Mater. Sci. Eng., A **371**, 313 (2004)
138. La, P., Ma, J., Zhu, Y.T., Yang, J., Liu, W., Xue, Q., Valiev, R.Z.: Dry-sliding tribological properties of ultrafine-grained Ti prepared by severe plastic deformation. Acta Mater. **53**, 5167 (2005)
139. Garbacz, H., Gradzka-Dahlke, M., Kurzydlowski, K.J.: The tribological properties of nano-titanium obtained by hydrostatic extrusion. Wear **263**, 572 (2007)
140. Wang, C.T., Gao, N., Gee, M.G., Wood, R.J.K., Langdon, T.G.: Effect of grain size on the micro-tribological behavior of pure titanium processed by high-pressure torsion. Wear **280–281**, 28–35 (2012)
141. Wang, C.T., Gao, N., Gee, M.G., Wood, R.J.K., Langdon, T.G.: Processing of an ultrafine-grained titanium by high-pressure torsion: an evaluation of the wear properties with and without a TiN coating. J. Mech. Behav. Biomed. Mater. **17**, 166–175 (2013)
142. Cheng, X., Li, Z., Xiang, G.: Dry sliding wear behavior of TiNi alloy processed by equal channel angular extrusion. Mater. Design **28**, 2218 (2007)
143. Rossiter, P.L.: The Electrical Resisitivity of Metals and Alloys. Cambridge University Press, Cambridge (1987)
144. Dugdale, J.S.: The Electrical Properties of Metals and Alloys. Arnold, London (1977)
145. Handbook Committee. In: ASM Handbook. Properties and Selection: Nonferrous Alloys and Special-Purpose Materials, vol. 2. ASM International (1990)

146. Higuera-Cobos, O.F., Cabrera, J.M.: Mechanical, microstructural and electrical evolution of commercially pure copper processed by equal channel angular extrusion. Mater. Sci. Eng., A **571**, 103–114 (2013)
147. Zhang, Y., Li, Y.S., Tao, N.R., Lu, K.: High strength and high electrical conductivity in bulk nanograined Cu embedded with nanoscale twins. Appl. Phys. Lett. **91**, 211901 (2007)
148. Cheng, S., Ma, E., Wang, Y.M., Keckes, L.J., Youssef, K.M., Koch, C.C., Trociewitz, U.P., Han, K.: Tensile properties of in-situ consolidated nanocrystalline Cu. Acta Mater. **53**, 1521 (2005)
149. Takata, N., Lee, S.H., Tsuji, N.: Ultrafine grained copper alloy sheets having both high strength and high electric conductivity. Mater. Lett. **63**, 1757–1760 (2009)
150. Need, R.F., Alexander, D.J., Field, R.D., Livescu, V., Papin, P., Swenson, C.A., Mutnick, D. B.: The effects of equal channel angular extrusion on the mechanical and electrical properties of alumina dispersion-strengthened copper alloys. Mater. Sci. Eng., A **565**, 450–458 (2013)
151. Vinogradov, A., Suzuki, Y., Ishida, T., Kitagawa, K., Kopylov, V.I.: Effect of chemical composition on structure and properties of ultrafine grained Cu–Cr–Zr alloys produced by equal-channel angular pressing. Mater. Trans. **45**, 2187–2191 (2004)
152. Botcharova, E., Freudenberger, J., Schultz, L.: Mechanical and electrical properties of mechanically alloyed nanocrystalline CuNb alloys. Acta Mater. **54**, 3333–3341 (2006)
153. Islamgaliev, R.K., Nesterov, K.M., Bourgon, J., Champion, Y., Valiev, R.Z.: Nanostructured Cu–Cr alloy with high strength and electrical conductivity. J. Appl. Phys. **115**, 194301 (2014)
154. Murashkin, MYu., Sabirov, I., Kazykhanov, V.U., Bobruk, E.V., Dubravina, A.A., Valiev, R.Z.: Enhanced mechanical properties and electrical conductivity in ultrafine-grained Al alloy processed via ECAP-PC. J. Mater. Sci. **48**, 4501 (2013)
155. Bobruk, E.V., Murashkin, MYu., Kazykhanov, V.U., Valiev, R.Z.: Aging behavior and properties of ultrafine-grained aluminum alloys of Al–Mg–Si system. Rev. Adv. Mater. Sci. **31**, 14–34 (2012)
156. Valiev, R.Z., Murashkin, MYu., Sabirov, I.: A nanostructural design to produce high strength Al alloys with enhanced electrical conductivity. Scripta Mater. **76**, 13–16 (2014)
157. Cahn, R.W., Haasen, P., Kramer, E.J. In: Materials Science and Technology, vol 8/9, p. 282. Wiley-VCH, New York (2005)
158. Kasap, S., Capper, P. (eds.): Springer Handbook of Electronic and Photonic Materials. Springer, Würzburg (2006)
159. Chen, X.H., Lu, L., Lu, K.: Electrical resistivity of ultrafine-grained copper with nanoscale growth twins. J. Appl. Phys. **102**, 083708 (2007)
160. Sauvage, X., Wilde, G., Divinski, S.V., Horita, Z., Valiev, R.Z.: Grain boundaries in ultrafine grained materials processed by severe plastic deformation and related phenomena. Mater. Sci. Eng., A **540**, 1–12 (2012)
161. Gubicza, J., Schiller, I., Chinh, N.Q., Illy, J., Horita, Z., Langdon, T.G.: The effect of severe plastic deformation on precipitation in supersaturated Al–Zn–Mg alloys. Mater. Sci. Eng., A **460–461**, 77–85 (2007)
162. Sha, G., Wang, Y.B., Liao, X.Z., Duan, Z.C., Ringer, S.P., Langdon, T.G.: Influence of equal-channel angular pressing on precipitation in an Al–Zn–Mg–Cu alloy. Acta Mater. **57**, 3123–3132 (2009)
163. Garcia-Infanta, J.M., Swaminathan, S., Cepeda-Jimenez, C.M., McNelley, T.R., Ruano, O. A., Carreno, F.: Enhanced grain refinement due to deformation-induced precipitation during ambient-temperature severe plastic deformation of an Al–7 % Si alloy. J. Alloys Compd. **478**, 139–143 (2009)
164. Roven, H.J., Liu, M., Werenskiold, J.C.: Dynamic precipitation during severe plastic deformation of an Al-Mg–Si aluminium alloy. Mater. Sci. Eng., A **483–484**, 54–58 (2008)
165. Murayama, M., Hono, K., Saga, M., Kikuchi, M.: Atom probe studies on the early stages of precipitation in Al–Mg–Si alloys. Mater. Sci. Eng., A **250**, 127 (1998)

166. Genevois, C., Fabregue, D., Deschamps, A., Poole, W.J.: On the coupling between precipitation and plastic deformation in relation with friction stir welding of AA2024 T3 aluminium alloy. Mater. Sci. Eng., A **441**, 39 (2006)
167. Sauvage, X., Murashkin, MYu., Valiev, R.Z.: Atomic scale investigation of dynamic precipitation and grain boundary segregation in a 6061 aluminium alloy nanostructured by ECAP. Kovove Mater. **49**(1), 11–15 (2011)
168. Kiessling, F., Nefzger, P., Nolasco, J.F., Kaintzyk, U.: Overhead Power Lines: Planning, Design, Construction. Springer, Berlin (2003)
169. Nishizaki, T., Lee, S., Horita, Z., Sasaki, T., Kobayashi, N.: Superconducting properties in bulk nanostructured niobium prepared by high-pressure torsion. Physica C **493**, 132–135 (2013)
170. Beloshenko, V.A., Chishko, V.V.: Deformation-heat treatment of Nb-Ti superconductors using severe plastic deformation methods. Phys. Met. Metall. **114**, 992–1002 (2013)
171. Edalati, K., Diao, T., Lee, S., Horita, Z., Nishizaki, T., Akune, T., Nojima, T., Sasaki, T.: High strength and superconductivity in nanostructured niobium-titanium alloy by high-pressure torsion and annealing: Significance of elemental decomposition and supersaturation. Acta Mater. **80**, 149–158 (2014)
172. Herzer, G. In: Buschow, K.H.J. (ed.) Handbook of Magnetic Materials, vol. 10, p. 415. Elsevier Science B.V. (1997)
173. Mulyukov, K.Y., Khaphisov, S.B., Valiev, R.Z.: Grain boundaries and saturation magnetization in submicron grained nickel. Phys. Stat. Sol. (a) **133**, 447 (1992)
174. Valiev, R.Z., Korznikova, G.F., Mulyukov, K.Y., Mishra, R.S., Mukherjee, A.K.: Saturation magnetization and curie temperature of nanocristalline nickel. Phil. Mag. B **75**, 803 (1997)
175. Mulyukov, K.Y., Korznikova, G.F., Abdulov, R.Z., Valiev, R.Z.: Microstructure and magnetic properties of submicron grained cobalt after large plastic deformation and their variation during annealing. Phys. Stat. Sol. **125**, 609 (1991)
176. Scheriau, S., Kriegisch, M., Kleber, S., Mehboob, N., Grossinger, R., Pippan, R.: Magnetic chatacteristics of HPT deformed soft-magnetic materials. J. Magn. Magn. Mater. **322**, 2984–2988 (2010)
177. Mulyukov, K.Y., Korznikova, G.F., Sagdatkireyeva, M.B., Timofeyev, V.N., Valiev, R.Z.: The study of domain structure of submicron grained cobalt and its changes during heating. J. Magn. Magn. Mater. **110**, 73 (1992)
178. Marin, P., Vazquez, M., Hernando, A.: Magnetic hardening during the amorphous to nanocrystalline transformation in FeSiBCuNb alloys: theoretical considerations. J. Magn. Magn. Mater. **196–197**, 221–223 (1999)
179. Chbihi, A., Sauvage, X., Genevois, C., Blavette, D., Gunderov, D., Popov, A.G.: Optimization of the magnetic properties of FePd alloys by severe plastic deformation. Adv. Eng. Mater. **12**, 708–713 (2010)
180. Stolyarov, V.V., Gunderov, D.V., Valiev, R.Z., Popov, A.G., Gaviko, V.S., Ermolenko, A. S.: Metastable states in R2Fe14B-based alloys processed by severe plastic deformation. J. Magn. Magn. Mater. **196–197**, 166–168 (1999)
181. Stolyarov, V.V., Gunderov, D.V., Popov, A.G., Puzanova, T.Z., Raab, G.I., Yavari, A.R., Valiev, R.Z.: High coercive states in Pr-Fe-B-Cu alloy processed by equal channel angular pressing. J. Magn. Magn. Mater. **242–245**, 1399–1401 (2002)
182. Stolyarov, V.V., Gunderov, D.V., Popov, A.G., Gavilko, V.S., Ermolenko, A.S.: Structure evolution and changes in magnetic properties of severe plastic deformed Nd(Pr)-Fe-B alloys during annealing. J. Alloys Compds. **281**, 69–71 (1998)
183. Popov, A.G., Gunderov, D.V., Stolyarov, V.V.: Severe plastic deformation—a new method of formation of a high coercivity state in PrFeB-alloy. J. Magn. Magn. Mater. **33**, 157–158 (1996)
184. Stolyarov, V.V., Popov, A.G., Gunderov, D.V., Gaviko, V.S., Korznikova, G.F., Ermolenko, A.S., Valiev, R.Z.: Effect of severe plastic deformation on the structure and magnetic properties of Pr–Fe–B–Cu alloys. Phys. Met. Metall. **83**(2), 173 (1997)

185. Korznikova, G.F., Korznikov, A.V.: Gradient submicrocrystalline structure in Fe–Cr–Co system hard magnetic alloys. Mater. Sci. Eng., A **503**, 99–102 (2009)
186. Straumal, B.B., Protasova, S.G., Mazilkin, A.A., Kogtenkova, O.A., Kurmanaeva, L., Baretzky, B., Schutz, G., Korneva, A., Zieba, P.: SPD induced changes in the Cu–Co alloys. Mater. Lett. **98**, 217–221 (2013)
187. Suehiro, K., Nishimura, S., Horita, Z.: Change in magnetic property of Cu-6.5Co alloy through processing by ECAP. Mater. Trans. **49**, 102–106 (2008)
188. Sagawa, M., Fujimura, S., Yamamoto, H., Matsuura, Y., Hiraga, K.: IEEE Trans. Magn. **20** (5), 1584 (1984)
189. Shimoda, T., Akioka, K., Kobayashi, O., Yamagami, T., Ohki, T., Miayagawa, M., Yuri, T.: Hot working behavior of cast Pr–Fe-B magnets. IEEE Trans. Magn. **25**(5), 4099 (1989)
190. Menéndez, E., Sort, J., Langlais, V., Zhilyaev, A., Muñoz, J.S., Suriñach, S., Nogués, J., Baró, M.D.: Cold compaction of metal–ceramic (ferromagnetic–antiferromagnetic) composites using high pressure torsion. J. Alloys Compds. **434–435**, 505–508 (2007)
191. Kisker, H., Gessmann, T., Wurschum, R., Kronmuller, H., Schaefer, H.E.: Magnetic properties of high purity nanocrystalline nickel. Nanostr. Mater. **6**, 925–928 (1995)
192. Rubel, M.: Reactor aspects of fusion: issues related to materials, radioactivity and radiation induced defects. Trans. Fusion Sci. Tech. **49**, 465–473 (2006)
193. Garner, F.A. In: Comprehensive Nuclear Materials. Radiation Damage in Austenitic Steels, vol. 4, p. 33. Elsevier, Amsterdam (2012)
194. Thomson, M.W.: Defects and Radiation Damage in Metals. Cambridge University Press, New York (1969)
195. Parshin, A.M.: Structure, Strength and Radiation Damage of Corrosion-Resistant Steels and Alloys, p. 361. Amer. Nucl. Soc., La Grange Park (1996)
196. Abramivich, M.D., Votinov, S.N., Yoltukhvsky, A.G.: Radiation Materials Science in Atomic Power Stations. Energoatomizdat, Moscow (1984)
197. Alamo, A., Seran, J.L., Rabouille, O., Brachet, J.C., Mailard, A., Touron, H., Royer, J. In: Gelles, D.S., Nanstag, R.K., Kumar, A.S., Little, E.A. (eds.) Effects of Radiation on Materials: 17th International Symposium, ASTM STP 1270. American Society for Testing and Materials (1996)
198. Borodin, O.V., Bruk, V.V., Voevodin, V.N., Neklyudov, I.M., Shamardin, V.K., Neystroev, V.S. In: Gelles, D.S., Nanstag, R.K., Kumar, A.S., Little, E.A. (eds.) Effects of Radiation on Materials: 17th International Symposium, ASTM STP 1270. American Society for Testing and Materials (1996)
199. Schaeublin, R., Leguey, T., Spaetig, P., Baluk, N., Victoria, M.: Microstructure and mechanical properties of two ODS ferritic/martensitic steels. J. Nucl. Mater. **307**, 778–782 (2002)
200. Brailsford, A.D., Bullough, R. In: Proc. Int. Conf. Phys. Met. React. Fuel Flem. Swelling of irradiated materials, p. 148. Berkeley Castle and Berkeley Nucl. Lab., London (1973)
201. Maksimkin, O.P., Shiganakov, S.B.: On the role of grain boundaries in work hardening and high-temperature embrittlement of irradiated metallic materials, p. 35. Preprint of Inst. Nuclear Phys. Kazakhstan Academy of Science, No.1-86, Alma-Ata (1986)
202. Chimi, Y., Iwase, A., Ishikawa, N., Kobiyama, M., Inami, T., Okuda, S.: Accumulation and recovery of defects in ion-irradiated nanocrystalline gold. J. Nucl. Mater. **297**, 355 (2001)
203. Rose, M., Balogh, A.G., Hahn, H.: Instability of irradiation induced defects in nanostructured materials. Nucl. Instr. Meth. Phys. Res. B **119**, 127–128 (1997)
204. Samaras, M., Derlet, P.M., Van Swygenhoven, H., Victoria, M.: Computer simulation of displacement cascades in nanocrystalline Ni. Phys. Rev. Lett. **88**, 125505 (2002)
205. Samaras, M., Derlet, P.M., Van Swygenhoven, H., Victoria, M.: Stacking fault tetrahedra formation in the neighbourhood of grain boundaries. Nucl. Instr. Meth. Phys. Res. B **202**, 51 (2003)
206. Samaras, M., Derlet, P.M., Van Swygenhoven, H., Victoria, M.: Radiation damage near grain boundaries. Phil. Mag. **83**, 3599 (2003)

207. Voegeli, W., Albe, K., Hahn, H.: Simulation of grain growth in nanocrystalline nickel induced by ion irradiation. Nucl. Instrum. Meth. B **202**, 230 (2003)
208. Valiev, R.Z., Islamgaliev, R.K., Alexandrov, I.V.: Bulk nanostructured materials from severe plastic deformation. Prog. Mater Sci. **45**, 105 (2000)
209. Lowe, T.C., Valiev, R.Z.: Producing nanoscale microstructures through severe plastic deformation. JOM **52**, 27 (2000)
210. Valiev, R.Z.: Nanomaterial advantage. Nature **419**, 887–889 (2002)
211. Korshunov, A.I., Vedernikova, I.I., Polyakov, L.V., Kravchenko, T.N., Smolyakov, A.A., Soloviev, V.P.: Effects of the number of ECAP passes and ECAP route on the heterogeneity in mechanical properties across the sample from titanium VT1-0. In: Proceedings of the 3rd International Conference on Nanomaterials by Severe Plastic Deformation, Fukuoka, Japan (2005)
212. Korshunov, A.I., Vedernikova, I.I., Polyakov, L.V., Kravchenko, T.N., Smolyakov, A.A., Soloviev, V.P.: Effects of the number of ECAP passes and ECAP route on the heterogeneity in mechanical properties across the sample from ultrafine copper. Rev. Adv. Mater. Sci. **10**, 34–40 (2005)
213. Raab, G.J., Valiev, R.Z., Lowe, T.C., Zhu, Y.T.: Continuous processing of ultrafine grained Al by ECAP—conform. Mater. Sci. Eng., A **382**, 30 (2004)
214. Lowe, T.C., Valiev, R.Z.: The use of severe plastic deformation techniques in grain refinement. JOM **56**, 64–68 (2004)
215. Nita, N., Schaeublin, R., Victoria, M., Valiev, R.Z.: Effects of irradiation on the microstructure and mechanical properties of nanostructured materials. Phil. Mag. **85**, 723 (2005)
216. Kilmametov, A.R., Gunderov, D.V., Valiev, R.Z., Balogh, A.G., Hahn, H.: Enhanced ion irradiation resistance of bulk nanocrystalline TiNi alloy. Scripta Mater. **59**, 1027–1030 (2008)
217. Radiguet, B., Etienne, A., Pareige, P., Sauvage, X., Valiev, R.: Irradiation behavior of nanostructured 316 austenitic stainless steel. J. Mater. Sci. **43**, 7338–7343 (2008)
218. Revathy Rajan, P.B., Monnet, I., Hug, E., Etienne, A., Enikeev, N., Keller, C., Sauvage, X., Valiev, R., Radiguet, B.: Irradiation resistance of a nanostructured 316 austenitic stainless steel. IOP Conf. Ser.: Mater. Sci. Eng. **63**, 012121 (2014)
219. Shamardin, V.K., Goncharenko, YuD, Bulanova, T.M., Karsakov, A.A., Alexandrov, I.V., Abramova, M.M., Karavaeva, M.V.: Effect of neutron irradiation on microstructure and properties of austenitic AISI 321 steel, subjected to equal-channel angular pressing. Rev. Adv. Mater. Sci. **31**, 167–173 (2012)
220. Alsabbagh, A., Valiev, R.Z., Murty, K.L.: Influence of grain size on radiation effects in a low carbon steel. J. Nucl. Mater. **443**, 302–310 (2013)
221. Alsabbagh, A., Sarkar, A., Miller, B., Burns, J., Squires, L., Porter, D., Cole, J.I., Murty, K. L.: Microstructure and mechanical behavior of neutron irradiated ultrafine grained ferritic steel. Mater. Sci. Eng., A **615**, 128–138 (2014)
222. Roy, I., Yang, H.W., Dinh, L., Lund, I., Earthman, J.C., Mohamed, F.A.: Possible origin of superior corrosion resistance for electrodeposited nanocrystalline Ni. Scripta Mater. **59**, 305–308 (2008)
223. Ralston, K.D., Birbilis, N.: Effect of grain size on corrosion: a review. Corrosion **66**, 075005 (2010)
224. Kim, H.S., Yoo, S.J., Ahn, J.W., Kim, D.H., Kim, W.J.: Ultrafine grained titanium sheets with high strength and high corrosion resistance. Mater. Sci. Eng., A **528**, 8479–8485 (2011)
225. Balyanov, A., Kutnyakova, J., Amirkhanova, N.A., Stolyarov, V.V., Valiev, R.Z., Liao, X. Z., Zhao, Y.H., Jiang, Y.B., Xu, H.F., Lowe, T.C., Zhu, Y.T.: Corrosion resistance of ultra fine-grained Ti. Scripta Mater. **51**, 225–229 (2004)
226. Hoseini, M., Shahryari, A., Omanovic, S., Szpunar, J.A.: Comparative effect of grain size and texture on the corrosion behaviour of commercially pure titanium processed by equal channel angular pressing. Corros. Sci. **51**, 3064–3067 (2009)

227. Kim, H.S., Kim, W.J.: Annealing effects on the corrosion resistance of ultrafine-grained pure titanium. Corros. Sci. **89**, 331–337 (2014)
228. Kim, H.S., Kim, W.J.: Enhanced corrosion resistance of ultrafine-grained AZ61 alloy containing very fine particles of Mg17Al12 phase. Corros. Sci. **75**, 228–238 (2013)
229. Jinlong, L., Hongyun, L.: Comparison of corrosion properties of passive films formed on phase reversion induced nano/ultrafine-grained 321 stainless steel. Appl. Surf. Sci. **280**, 124–131 (2013)
230. Zhang, L., Ma, A., Jiang, J., Yang, D., Song, D., Chen, J.: Sulphuric acid corrosion of ultrafine-grained mild steel processed by equal-channel angular pressing. Corros. Sci. **75**, 434–442 (2013)
231. Hadzima, B., Janeček, M., Estrin, Y., Kim, H.S.: Microstructure and corrosion properties of ultrafine-grained interstitial free steel. Mater. Sci. Eng., A **462**, 243–247 (2007)
232. Shahryari, A., Szpunar, J.A., Omanovic, S.: The influence of crystallographic orientation distribution on 316LVM stainless steel pitting behavior. Corros. Sci. **51**, 677–682 (2009)
233. Song, D., Ma, A.B., Jiang, J., Lin, P., Yang, D., Fan, J.: Corrosion behavior of equal-channel-angular-pressed pure magnesium in NaCl aqueous solution. Corros. Sci. **52**, 481–490 (2010)
234. Song, D., Ma, A., Jiang, J., Lin, P., Yang, D., Fan, J.: Corrosion behaviour of bulk ultra-fine grained AZ91D magnesium alloy fabricated by equal-channel angular pressing. Corros. Sci. **53**, 362 (2011)
235. Wei, W., Wei, K.X., Du, Q.B.: Corrosion and tensile behaviors of ultra-fine grained Al–Mn alloy produced by accumulative roll bonding. Mater. Sci. Eng., A **454–455**, 536–541 (2007)
236. Sharma, M.M., Ziemian, C.W.: Pitting and stress corrosion cracking susceptibility of nanostructrued Al–Mg alloys in natural and artificial environments. J. Mater. Eng. Perf. **17**, 870–878 (2008)
237. Naeini, M.F., Shariat, M.H., Eizadjou, M.: On the chloride-induced pitting of ultra fine grains 5052 aluminum alloy produced by accumulative roll bonding process. J. Alloys Compds. **509**, 4696–4700 (2011)
238. Hockauf, M., Meyer, L.W., Nickel, D., Alisch, G., Lampke, T., Wielage, B., Kruger, L.: Mechanical properties and corrosion behaviour of ultrafine-grained AA6082 produced by equal-channel angular pressing. J. Mater. Sci. **43**, 7409–7417 (2008)
239. Sikora, E., Wei, X.J., Shaw, B.A.: Corrosion behavior of nanocrystalline Al–Mg based alloys. Corrosion **60**, 387–397 (2004)
240. Gurao, N.P., Manivasagam, G., Govindaraj, P., Asokamani, R., Suwas, S.: Effect of texture and grain size on bio-corrosion response of ultrafine-grained titanium. Metall. Mater. Trans. A **44**, 5602–5610 (2013)
241. Balakrishnan, A., Lee, B.C., Kim, T.N., Panigrahi, B.B.: Corrosion behaviour of ultra fine grained titanium in simulated body fluid for implant application. Trends Biomater. Artif. Organs **22**, 54–60 (2008)
242. Gu, X.N., Li, N., Zheng, Y.F., Kang, F., Wang, J.T., Ruan, L.: In vitro study on equal channel angular pressing AZ31 magnesium alloy with and without back pressure. Mater. Sci. Eng., B **176**, 1802–1806 (2011)
243. Ralston, K.D., Birbilis, N., Davies, C.H.J.: Revealing the relationship between grain size and corrosion rate of metals. Scripta Mater. **63**, 1201–1204 (2010)
244. Ralston, K.D., Fabijanic, D., Birbilis, N.: Effect of grain size on corrosion of high purity aluminium. Electrochim. Acta **56**, 1729–1736 (2011)
245. Birbilis, N., Ralston, K.D., Virtanen, S., Fraser, H.L., Davies, C.H.J.: Grain character influences on corrosion of ECAPed pure magnesium. Corros. Eng. Sci. Tech. **45**, 224 (2010)
246. op't Hoog, C., Birbilis, N., Estrin, Y.: Corrosion of pure Mg as a function of grain size and processing route. Adv. Eng. Mater. **10**, 579 (2008)
247. Liu, K.T., Duh, J.G.: Grain size effects on the corrosion behaviour of Ni50.5Ti49.5 and Ni45.6Ti49.3Al5.1 films. J. Electroanal. Chem. **618**, 45 (2008)

248. Ghosh, S.K., Dey, G.K., Dusane, R.O., Grover, A.K.: Improved pitting corrosion behaviour of electrodeposited nanocrystalline Ni–Cu alloys in 3.0 wt% NaCl solution. J. Alloys Compd. **426**, 235 (2006)
249. Mahmoud, T.S.: Effect of friction stir processing on electrical conductivity and corrosion resistance of AA6063-T6 Al alloy. J. Mech. Eng. Sci. **222**, 1117 (2008)
250. Lin, P., Palumbo, G., Erb, U., Aust, K.T.: Influence of grain boundary character distribution on sensitization and intergranular corrosion of alloy 600. Scripta Metall. Mater. **33**, 1387 (1995)
251. Mishnaevsky Jr, L., Levashov, E., Valiev, R.Z., Segurado, J., Sabirov, I., Enikeev, N., Prokoshkin, S., Solov'yov, A.V., Korotitskiy, A., Gutmanas, E., Gotman, I., Rabkin, E., Psakh'e, S., Dluhos, L., Seefeldt, M., Smolin, A.: Nanostructured titanium-based materials for medical implants: modeling and development. Mater. Sci. Eng., R **81**, 1–19 (2014)
252. Williams, D.F.: On the mechanisms of biocompatibility. Biomaterials **29**, 2941–2953 (2008)
253. Niinomi, M.: Biologically and mechanically biocompatible titanium alloys. Mater. Trans. **49**, 2170–2178 (2008)
254. Geetha, M., Singh, A.K., Asokamani, R., Gogia, A.K.: Ti based biomaterials, the ultimate choice for orthopaedic implants—a review. Prog. Mater Sci. **54**, 397–425 (2009)
255. Long, M., Rack, H.J.: Titanium alloys in total joint replacement—a materials science perspective. Biomaterials **19**, 1621–1639 (1998)
256. Lowe, T.C., Valiev, R.Z.: Bulk nanostructured metals in biomedical applications. In: Tiwari, A., Nordin, A.N. (eds.) Advanced Biomaterials and Biodevices Frontiers, pp. 1–52. Wiley-Scrivener, New York (2014)
257. Bagherifard, S., Ghelichi, R., Khademhosseini, A., Guagliano, M.: Cell response to nanocrystallized metallic substrates obtained through severe plastic deformation. ACS Appl. Mater. Interf. **11**, 7963 (2014)
258. Webster, T.J., Ejiofor, J.U.: Increased osteoblast adhesion on nanophase metals: Ti, Ti6Al4V, and CoCrMo. Biomaterials **25**, 4731–4739 (2004)
259. Ward, B.C., Webster, T.J.: Increased functions of osteoblasts on nanophase metals. Mater. Sci. Eng., C **27**, 575–578 (2007)
260. Faghihi, S., Zhilyaev, A.P., Szpunar, J.A., Azari, F., Vali, H., Tabrizian, M.: Nanostructuring of a titanium material by high-pressure torsion improves pre-osteoblast attachment. Adv. Mater. **19**, 1069–1073 (2007)
261. Faghihi, S., Azari, F., Zhilyaev, A.P., Szpunar, J.A., Vali, H., Tabrizian, M.: Cellular and molecular interactions between MC3T3-E1 pre-osteoblasts and nanostructured titanium produced by high-pressure torsion. Biomaterials **28**, 3887–3985 (2007)
262. Valiev, R.Z., Semenova, I.P., Latysh, V.V., Rack, H., Lowe, T.C., Petruzelka, J., Dluhos, L., Hrusak, D., Sochova, J.: Nanostructured titanium for biomedical applications. Adv. Eng. Mater. **10**(8), B15–B17 (2008)
263. Estrin, Y., Kasper, C., Diederichs, S., Lapovok, R.: Accelerated growth of preosteoblastic cells on ultrafine grained titanium. J. Biomed. Mater. Res. A. **90**, 1239–1242 (2009)
264. Nie, F.L., Zheng, Y.F., Cheng, Y., Wei, S.C., Valiev, R.Z.: In vitro corrosion and cytotoxicity on microcrystalline, nanocrystalline, and amorphous NiTi alloy fabricated by high pressure torsion. Mater. Lett. **64**, 983–986 (2010)
265. Zheng, C.Y., Nie, F.L., Zheng, Y.F., Cheng, Y., Wei, S.C., Valiev, R.Z.: Enhanced in vitro biocompatibility of ultrafine-grained titanium with hierarchical porous surface. Appl. Surf. Sci. **257**, 5634–5640 (2011)
266. Zheng, C.Y., Nie, F.L., Zheng, Y.F., Cheng, Y., Wei, S.C., Valiev, R.Z.: Enhanced in vitro biocompatibility of ultrafine-grained titanium with hierarchical porous surface. Appl. Surf. Sci. **257**, 9086–9093 (2011)
267. Estrin, Y., Ivanova, E.P., Michalska, A., Truong, V.K., Lapovok, R., Boyd, R.: Accelerated stem cell attachment to ultrafine grained titanium. Acta Biomater. **7**, 900–906 (2011)

268. Venkatsurya, P.K.C., Girase, B., Misra, R.D.K., Pesacreta, T.C., Somani, M.C., Karjalainen, L.P.: The interplay between osteoblast functions and the degree of nanoscale roughness induced by grain boundary grooving of nanograined materials. Mater. Sci. Eng., C **32**, 330–340 (2012)
269. Korotin, D.M., Bartkowski, S., Kurmaev, E.Z., Neumann, M., Yakushina, E.B., Valiev, R.Z., Cholakh, S.O.: Surface studies of coarse-grained and nanostructured titanium implants. J. Nanosci. Nanotech. **12**, 8567–8572 (2012)
270. Misra, R.D.K., Nune, C., Pesacreta, T.C., Somani, M.C., Karjalainen, L.P.: Understanding the impact of grain structure in austenitic stainless steel from a nanograined regime to a coarse-grained regime on osteoblast functions using a novel metal deformation-annealing sequence. Acta Biomater. **9**, 6245–6258 (2013)
271. Zhu, Y.T., Lowe, T.C., Valiev, R.Z., Stolyarov, V.V., Latysh, V.V., Raab, G.I.: Ultra-fine-grained titanium for medical implants. U.S. Patent No. US6399215 B1, 4 June 2002
272. Re, F., Zanetti, A., Sironi, M., Polentarutti, N., Lanfrancone, L., Dejana, E., Collotta, F.: Inhibition of anchorage-dependent cell spreading triggers apoptosis in cultured human endothelial cells. J. Cell Biol. **127**, 537–546 (1994)
273. Yamanaka, K., Mori, M., Chiba, A.: Origin of significant grain refinement in Co–Cr–Mo alloys without severe plastic deformation. Metall. Mater. Trans. A **43**, 4875–4887 (2012)
274. Yamanaka, K., Mori, M., Chiba, A.: Enhanced mechanical properties of As-forged Co–Cr–Mo–N alloys with ultrafine-grained structures. Metallur. Mater. Trans. A. **43**, 5243–5257 (2012)
275. Bauer, S., Schmuki, P., von der Mark, K., Park, J.: Engineering biocompatible implant surfaces Part I: materials and surfaces. Prog. Mater. Sci. **58**, 261–326 (2013)
276. Zhou, J., Sun, C., Wu, X., Tao, N., Liu, G., Meng, X., Hong, Y.: Nanocrystalline formation during mechanical attrition of cobalt. Mater. Sci. Forum **503–504**, 751–756 (2006)
277. Jiang, J., Ren, J., Shan, A., Liu, J., Song, H.: Surface nanocrystallization of Ni_3Al by surface mechanical attrition treatment. Mater. Sci. Eng., A **520**, 80–89 (2009)
278. Ren, J., Li, D., Xu, P.: Surface nanocrystallines of Fe_3Al produced by surface mechanical attrition. Adv. Mater. Res. **320**, 325–328 (2011)
279. Li, W., Xu, W., Wang, X., Rong, Y.: Measurement of microstructural parameters of nanocrystalline Fe-30 wt%Ni alloy produced by surface mechanical attrition treatment. J. Alloys Compd. **474**, 546–550 (2009)
280. Zhao, C., Zhao, C., Cao, P., Ji, W., Han, P., Zhang, J., Zhang, F., Jiang, Y., Zhang, X.: Hierarchical titanium surface textures affect osteoblastic functions. J. Biomed. Mater. Res. A. **99**, 666–675 (2011)
281. Lin, C.C., Cheng, H.C., Huang, C.F., Lin, C.T., Lee, S.Y., Chen, C.S., Ou, K.L.: Enhancement of biocompatibility on bioactive Ti surface by low temperature plasma treatment. Jap. J. Appl. Phys. **44**, 8590–8598 (2005)
282. Li, H., Zheng, Y., Qin, L.: Progress of biodegradable metals. Prog. Nat. Sci.: Mater. Int. **24**, 414–422 (2014)
283. Zheng, Y.F., Gu, X.N., Witte, F.: Biodegradable metals. Mater. Sci. Eng. R. **77**, 1–34 (2014)
284. Brar, H.S., Platt, M.O., Sarntinoranont, M., Martin, P.I., Manuel, M.V.: Magnesium as a biodegradable and bioabsorbable material for medical implants. JOM **61**, 31–34 (2009)
285. Waizy, H., Seitz, J.M., Reifenrath, J., Weizbauer, A., Bach, F.W., Meyer-Lindenberg, A., Denkena, B., Windhagen, H.: Biodegradable magnesium implants for orthopedic applications. J. Mater. Sci. **48**, 39–50 (2013)
286. Vojtich, D., Elova, H., Volenec, K.: Investigation of magnesium-based alloys for biomedical applications. Kovove Mater. **44**, 206–219 (2006)
287. Staiger, M.P., Pietak, A.M., Huadmai, J., Dias, G.: Magnesium and its alloys as orthopedic biomaterials: a review. Biomaterials **27**, 1728–1734 (2006)
288. Mostaed, E., Hashempour, M., Fabrizi, A., Dellasega, D., Bestetti, M., Bonollo, F., Vedani, M.: Microstructure, texture evolution, mechanical properties and corrosion behavior of ECAP processed ZK60 magnesium alloy for biodegradable applications. J. Mech. Behav. Biomed. Mater. **37**, 307–322 (2014)

289. Li, Z., Gu, X., Lou, S., Zheng, Y.: The development of binary Mg–Ca alloys for use as biodegradable materials within bone. Biomaterials **29**, 1329 (2008)
290. Zhang, S., Zhang, X., Zhao, C., Li, J., Song, Y., Xie, C., Tao, H., Zhang, Y., He, Y., Jiang, Y., Bian, Y.: Research on an Mg–Zn alloy as a degradable biomaterial. Acta Biomater. **6**, 626 (2010)
291. Bahl, S., Suwas, S., Chatterjee, K.: The control of crystallographic texture in the use of magnesium as a resorbable biomaterial. RSC Adv. **4**, 55677–55684 (2014)
292. Yang, J., Cui, F., Lee, I.S.: Surface modifications of magnesium alloys for biomedical applications. Ann. Biomed. Eng. **39**, 1857–1871 (2011)
293. Wang, J., Tang, J., Zhang, P., Li, Y., Wang, J., Lai, Y., Qin, L.: Surface modification of magnesium alloys developed for bioabsorbable orthopedic implants: a general review. J. Biomed. Mater. Res. B **100**, 1691–1701 (2012)